

学位論文

A numerical study on the microphysical properties of
warm clouds off the west coast of California

カリフォルニア沖を対象とした

暖かい雲の微物理特性に関する数値実験

平成23年12月博士（理学）申請

東京大学大学院理学系研究科

地球惑星科学専攻

佐藤 陽祐

Abstract

This thesis investigates the characteristics of warm clouds off the coast of California by using a three-dimensional (3D) regional model with a Spectral Bin microphysical Model (SBM). To reproduce the characteristics of the warm clouds, the regeneration processes of aerosols have been implemented to the Japan Meteorological Agency Non-hydrostatic model with Hebrew University Cloud Model (JMA-NHM+HUCM).

3D idealized simulations with periodic boundary condition and downscaling simulations are conducted to verify model performance and to compare the model results with those obtained from observations. Numerical simulations by the model successfully reproduce the correlation pattern between cloud-droplet effective radius (RE r_e) and cloud optical thickness (COT τ_c) (RE-COT pattern) and Contoured Frequency Optical Depth Diagram (CFODD) retrieved from satellite observations.

Results of the idealized numerical experiments support the validity of an interpretation of previous studies on CFODD. The results also indicate that the characteristics of warm clouds are affected by grid resolution. However, the response of the cloud microphysical properties to aerosol amount and boundary layer (PBL) height does not depend on the grid resolution significantly. Therefore, the simulated results from coarse grid resolution experiments can acquire the fundamental features of the RE-COT pattern and CFODD. This finding is important for future global and/or long-term model simulations where it is difficult to adopt high resolution modeling like large eddy simulation (LES) modeling of several tens of meters.

3D-downscaling numerical experiments under a real atmospheric condition are also conducted to simulate the microphysical properties of warm clouds during the First ISCCP Regional Experiment (FIRE), and then combined analyses of RE-COT pattern and CFODD using the model results are, for the first time, conducted to investigate the cloud growth stage.

The model simulates the radiances observed from the visible wavelength sensor onboard the Advanced Very High Resolution Radiometer (AVHRR) satellite. The combined analysis and a box model calculation indicate that each of the RE-COT patterns does not always represent the observed cloud characteristics, but mixtures of RE-COT patterns from different clouds show a similarity to the satellite-derived pattern. This finding presents a new interpretation of the cloud microphysical properties seen by satellite-derived RE-COT patterns, in contrast to the interpretation by previous studies.

In conclusion the present results indicate that the characteristics of RE-COT patterns are totally

dependent on the drizzling rate, PBL height (corresponds to dynamic stability), and the aerosol amounts. Therefore, a comprehensive model including all these processes for successful simulation of the low-level clouds in the target region is needed. The lower the stability is the larger liquid water path (LWP) takes place at the right edge of the RE-COT patterns. The higher the aerosol amount is the larger the cloud droplet number concentration is found at the lower edge of RE-COT patterns. The geometrical center of the RE-COT pattern is mainly determined by the drizzling rate. It shifts to an area of larger RE and smaller COT values on the RE-COT plane when the drizzling rate is large, while it shifts to an area of smaller RE and larger COT values with a small drizzling rate.

Acknowledgements

This study of this PhD thesis was supported by many people and several funds. Firstly, the author would like to express his gratitude to Prof. T. Nakajima of the Atmosphere and Ocean Research Institute (AORI), the thesis supervisor, for his support of scientific advice and suggestions. The author is also grateful to all the reviewers of this paper, Prof. M. Koike of the University of Tokyo, Prof. M. Satoh of AORI, Prof. H. Niino of AORI, and Prof. M. Murakami of the Meteorological Research Institute for providing many useful comments in drafting this paper and their efforts in reviewing it.

The author would like to express thanks to Jørgen B. Jensen of the National Center for Atmospheric Research/Earth Observation Factory for advice concerning aircraft data analysis and supplying aircraft data, and to Prof. Xiquan Dong of the University of North Dakota for providing many comments while drafting this paper. The author is also grateful to Prof. T.Y. Nakajima of Toukai University for supplying satellite data and valuable comments on the satellite part of a paper submitted to the Journal of Atmospheric Science. Further thanks to Dr. K. Suzuki of NASA/JPL, Dr. T. Iguchi of NASA/GSFC, Dr. I.-J. Choi of Seoul National University, and Mr. H. Kadowaki for their efforts in developing the original version of the NHM bin model used and modified in this study and teaching the basic knowledge of cloud microphysics and numerical models. The author is also very thankful to all of members of AORI, especially for the members of T. Nakajima's laboratory for helping his everyday life in AORI.

This work is supported by Grant-in-Aid for JSPS Fellows 22-7893, JSPS Institutional Program for Young Researcher Overseas Visits, and the Initiative on Promotion of Supercomputing for Young Researchers from the Supercomputing division, Information Technology Center, University of Tokyo; projects of JAXA/EarthCARE, JAXA/GCOM-C, MEXT/VL for Climate System Diagnostics, MOE/Global Environment Research Fund A-1101, NIES/GOSAT, and MEXT/RECCA/SALSA. The computations for this study were carried out using Hitachi SR11000, Hitachi SR16000, Hitachi HA8000 of the Supercomputing division, Information Technology Center, University of Tokyo, and Hitachi SR16000 of the Research Institute of Information Technology, Kyushu University.

Finally, the author is especially thankful to his parents and sister for their support throughout his life.

Contents

Chapter 1. General Introduction -----	6
1.1. Effects of warm clouds on climate -----	6
1.2. Effects of aerosols on clouds microphysical and radiative properties -----	6
1.3. Previous modeling studies of warm clouds and spectral bin models -----	7
1.4. Correlation pattern between cloud-droplet effective radius (RE) and cloud optical thickness (COT) -----	8
1.5. Contoured Frequency Optical Depth Diagram (CFODD) -----	11
1.6. Grid resolution of model -----	13
1.7. Objective of this study -----	13
Chapter 2. Development and improvement of regional cloud resolving model -----	15
2.1. General description of University Tokyo-Aerosol Cloud Bin Model (UT-ACBM) -----	15
2.2. Improvement of UT-ACBM in this study -----	18
2.3. Radar simulator -----	19
Chapter 3. Investigation of the CFODD diagram using UT-ACBM model -----	21
3.1. Introduction -----	21
3.2. Experimental setup and satellite data -----	22
3.2.1. Experimental setup	
3.2.2. Calculation of CFODD from model results	
3.2.3. Satellite data	
3.3. Comparison of CFODD between model simulations and observation -----	27
3.4. Cloud growth process represented on CFODD -----	32
3.5. Time evolution of CFODD -----	34
3.6. Discussion -----	39
3.6.1. Benefit to take COD for vertical axis of CFODD	
3.6.2. Effect of vertical resolution of model	
3.7. Conclusion -----	41
Chapter 4. Effects of grid resolution on cloud microphysical properties -----	43
4.1. Introduction -----	43
4.2. Experimental setup -----	43
4.3. Results -----	43
4.4. Conclusion -----	49

Chapter 5. Simulations of warm clouds by one-way nesting -----	50
5.1. Introduction -----	50
5.2. Experimental setup and observation data for comparisons -----	52
5.2.1. Experimental setup	
5.2.1. Data for comparisons	
5.3. Comparison of model results with observations -----	56
5.4. Cloud growth process observed by satellite remote sensing -----	61
5.5. Conclusion -----	65
Chapter 6. Discussion -----	67
6.1. Sensitivity to aerosol and PBL height -----	67
6.2. Factors determining the characteristics of RE-COT patterns -----	72
6.3. Bi-modal distribution of RE-COT pattern -----	77
Chapter 7. General conclusion -----	80
Appendix -----	82
Appendix A1. Validity of several methods used in one-way nesting simulation -----	82
A1.1. Validity of the parameterization of Feingold et al. (1996)	
A1.2. Initial and lateral boundary SDF of hydrometeors	
A1.3. Initial and lateral boundary conditions for SDF of hydrometeors	
Appendix A2. Regeneration and other sources of aerosol -----	94
Appendix A3. Basic equations of dynamical core of JMA-NHM -----	95
Appendix A4. Estimation of CPU time of the model -----	96
Appendix A5. Factors determining general characteristics of CFODD -----	97
Appendix A6. Notations of symbols used in this paper -----	99
Appendix A7: Discussion on the threshold value of RE (RE=14 μ m) by the previous study ----	103
Appendix A8: Description of Monte Carlo integration of stochastic collection equation (SCE) and two-dimensional spectral bin model (2D-SBM) -----	104
A8.1. Monte Carlo integration of stochastic collection equation	
A8.2. Extension of one-dimensional SBM to two-dimensional SBM	
Appendix A9: Derivation of equations (3-7) and (6-1) -----	111
A9.1. Derivation of the equation (3-7)	
A9.2. Derivation of the equation (6-1)	
References -----	116

Chapter 1. General Introduction and motivations

1.1. Effects of warm clouds on climate

Clouds have large effects on the climate system through the hydrological cycle and energy budget of the Earth. Among many different types of clouds, warm clouds, whose cloud-top pressure is higher than 680 hPa (Rossow and Schiffer 1999), critically affect the Earth's climate system (Randall et al., 1984; Ma et al., 1996) through their high albedo for solar radiation, which effectively decreases the net radiation at the top of atmosphere (TOA), thus working as an efficient cooler in the climate system.

This radiative effect of warm clouds is recognized to be very large; that is, the shortwave forcing by mid-latitude stratus clouds can reach $\sim 150 \text{ W m}^{-2}$ (Klein and Hartmann, 1993). In spite of its significance, modeling of the climatic effects of clouds including warm clouds is one of the major sources of uncertainties in understanding and predicting global climate change (Stephens, 2005; IPCC AR4, 2007). In particular, it is important to reduce the large uncertainties in the evaluation of the radiative forcing of low-level clouds.

The albedo of warm clouds is mainly determined by the cloud optical thickness (COT τ_c), which is a key parameter governing the cloud albedo for solar radiation, and the cloud-droplet effective radius (RE r_{eff}) determines the cloud reflectivity in the shortwave infrared spectral windows. Thus, it is very important to have both cloud optical depth and cloud-droplet effective radius to improve the cloud radiative forcing estimate.

In this situation, a large amount of studies were conducted to obtain cloud microphysical and radiative properties from satellites (*e.g.* Han et al., 1994; Nakajima and Nakajima, 1995; Kawamoto et al., 2001; Rosenfeld, 2000) and aircraft measurement (*e.g.* Nakajima and King, 1990; Nakajima et al., 1991; Brenguier et al., 2000, 2003; van Zanten and Stevens, 2005; Dong et al., 2002; Dong and Mace, 2003). These two parameters, as the previous studies indicated, are closely related to the cloud microphysical properties such as liquid water path and particle size distribution function (SDF). In addition, aerosols affect these microphysical properties and, therefore, affect the cloud radiative forcing.

1.2. Effects of aerosols on the cloud microphysical and radiative properties

Aerosols are tiny particles in the atmosphere, and serve as cloud condensation nuclei (CCN); as a result, they can change cloud microphysical properties. There are characteristic differences in the

cloud properties depending on their environment with different CCN concentrations.

A well-known example is the systematic difference between cloud properties in continental and oceanic environments (Squires, 1956), which was also retrieved from satellite (Han et al., 1994, Kawamoto et al., 2001). It is considered that the systematic difference results from a positive correlation between concentrations of CCN and cloud droplets. Increase in aerosol loading (*i.e.* increase in CCN concentration) leads to a higher cloud droplet number concentration assuming a constant liquid water path, which results in an increase in the albedo of optically thin clouds (Twomey, 1974; known as the Twomey effects) and the cloud reflects more shortwave radiation.

Furthermore, an increase in the cloud droplet number concentration reduces cloud droplet size, and suppresses the collision/coagulation process and generation of drizzles and rain particles, which results in prolonging the cloud lifetime (Albrecht, 1989). These phenomena are generally called the cloud-aerosol interaction. As mentioned above, cloud-aerosol interaction is triggered by change of cloud droplet number concentration and cloud droplet sizes. Therefore the size distribution function (SDF) of the cloud polydispersion system, which is also closely related to RE and COT, is a key parameter.

1.3. Previous modeling studies of warm clouds and spectral bin models

As discussed in the previous section, SDFs are important indices to investigate the cloud-aerosol interaction. A spectral bin model (SBM), which predicts SDFs of hydrometeors explicitly, is a useful tool to investigate the effects of the aerosol on cloud microphysics properties (*i.e.*, RE and COT).

This situation has motivated a large amount of previous studies using SBM. Khain and Sednev (1996) investigated the effects of aerosols on convective clouds using an idealized 2D SBM simulation. Several other studies, as well as this study, were also conducted using SBM (*e.g.* Takahashi and Kawano, 1998; Khain et al., 2000; Khain et al., 2005), but all these simulations were mostly performed with a two-dimensional (2D) model because of the extremely large computational costs of SBM and the necessity to reduce computational costs.

Suzuki (2004) proposed a method that deployed the SDF of hydrometeors by basis function expansion and succeeded in reducing the number of bins. Sato et al. (2009) applied a stochastic scheme based on the Monte-Carlo numerical integration theory for collision/coagulation process of clouds, and reduced computational cost of the process to 10% of the cost by a standard integration scheme.

Supported by such progress in modeling technology as well as computer hardware, more realistic

simulations by 3D regional spectral bin models have just begun (*e.g.* Takahashi and Shimura, 2004; Lynn et al., 2005a; 2005b; 2007; Iguchi et al., 2008). Takahashi and Shimura (2004) reproduced a convective cloud system triggered by a warm bubble with 3D idealized simulation. Lynn et al. (2005a, 2005b) simulated a convective cloud system at the Florida peninsula by an SBM implemented into the fifth-generation NCAR/Penn State mesoscale model (MM5). Lynn et al. (2007) simulated an orographic cloud system in the Sierra Nevada Mountains by an SBM model. Iguchi et al. (2008, 2010) simulated an ensemble of convective clouds generated by a frontal system near Japan, and a snowstorm in the Great Lake area, respectively, by a 3D SBM.

In spite of these pioneering contributions to cloud modeling science, there are no studies, to our knowledge, of simulating low level warm clouds by a 3D regional SBM in a real atmosphere. Here, low level cloud off the coast of California were studied for which a higher model resolution is required in comparison to the convective clouds studied in the previous reports.

1.4. Correlation pattern between cloud-droplet effective radius (RE) and cloud optical thickness (COT)

Although there are a few studies simulating warm clouds by 3D regional SBMs off the west coast of California (East Pacific), this region is a good experimental field of warm clouds because there exist persistent warm clouds of various kinds including stratus, stratocumulus, and cumulus (Klein and Hartmann, 1993).

This has attracted investigators who conducted large eddy simulation (LES) with extremely fine grid resolution (*e.g.*, Ackermann et al., 2009; Stevens et al., 2005; Savic-Jovic and Stevens, 2008; Wang and Feingold, 2009a; 2009b; Feingold et al., 2010, Wang et al., 2011; Mechem et al., 2006; Wang et al., 1993; Mechem et al., 2003; McCaa and Bretherton, 2004; Uchida et al., 2010).

Although these studies are useful to understand the behaviors and processes of smaller scale clouds, the numerical domain size is too small (several tens of kilometers) to understand how the cloud system characteristically interacts with its large-scale environment and aerosols transported to this region as reported in past satellite studies. Some previous studies conducted mesoscale simulations of cloud boundary layers by a bulk microphysical model (*e.g.* Mocko and Cotton, 1995), but there are no studies, to our knowledge to date, to conduct a mesoscale simulation by an SBM targeting warm clouds in this region.

Iguchi et al. (2008) performed simulations of warm clouds by SBM targeted on the West Pacific, but satellite observations in the studies of Nakajima et al. (2001), Matsui et al. (2004), and Matsui et

al. (2006) suggested that the microphysical properties of warm clouds and characteristics of aerosols off the East Pacific are different from those in the West Pacific.

Nakajima et al. (2001) analyzed the aerosol number concentration retrieved from the Advanced Very High Resolution Radiometer (AVHRR) satellite, and showed that the aerosol number concentration in the East (West) Pacific is smaller (larger) than the global average. Matsui et al. (2004, 2006) showed that lower-tropospheric static stability (LTSS) of West and East Pacific is larger than 21 K and lower than 17 K, respectively, *i.e.*, East Pacific is more stable than West Pacific. They also insisted that both aerosol amount and LTSS correlate to cloud microphysical parameter (*e.g.*, RE, Liquid water path, cloud albedo).

From these results, it appears that the dynamical and aerosol condition of East and West Pacific is completely different, and the cloud microphysical characteristics appear to be different in each region because of the difference of these conditions. This background suggests that it is necessary to conduct mesoscale simulation by SBM targeting warm clouds off the coast of California (East Pacific).

To evaluate the model results, a great amount of observation campaigns, *e.g.*, First International Satellite Cloud Climatology Project (ISCCP) Regional Experiment (FIRE) (Albrecht et al., 1988), second Dynamics and Chemistry of Marine Stratocumulus (DYCOMS-II) (Stevens et al., 2003), Marine Stratus/Stratocumulus Experiment (MASE) (Daum et al., 2007) were conducted off the west coast of California.

During these observation campaigns, Nakajima and King (1990) retrieved RE and COT by aircraft remote sensing during FIRE period, and Nakajima et al. (1991) found that RE and COT tends to be positively correlated when the clouds do not include drizzle-sized particles, whereas a negative correlation is found when the drizzle-sized particles occur frequently in the clouds as illustrated in Fig. 1.1.

These correlation patterns can be interpreted as a manifestation of the growth processes of cloud droplets that take place in the cloud system. Nakajima and Nakajima (1995; henceforth referred to as NN95) extended the analysis of Nakajima et al. (1991) into wider regions of the FIRE using AVHRR satellite data, and investigated statistical relationships between RE and COT (henceforth referred to as RE-COT pattern).

Suzuki et al. (2006) investigated the effects of aerosols on the RE-COT pattern by a 2D idealized SBM model, and successfully reproduced the positive (negative) correlation pattern when the aerosol amount is large (small). Suzuki et al. (2010a) interpreted that the RE-COT pattern represents growth stages of cloud droplets described as follows: Both COT and RE increase when the

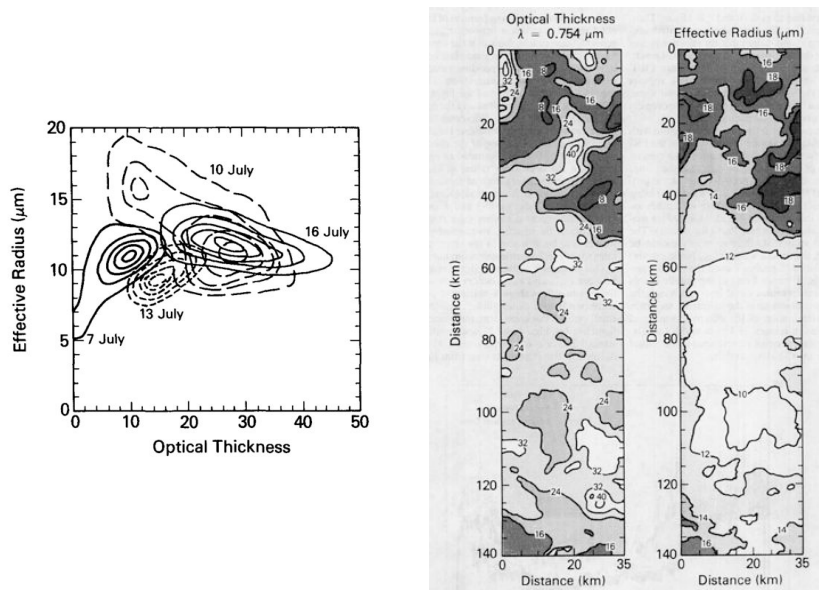


Figure 1.1. (Left) Correlation pattern of cloud-droplet effective radius r_{eff} vs. cloud optical thickness τ_c retrieved from aircraft remote sensing over the FIRE region from July 7 to 16, 1987 (Nakajima et al., 1991) and (right) the spatial distributions of cloud optical thickness and effective radius on 10 July 1987.

condensation growth process is dominant because the number concentration of cloud droplets is constant within a cloud layer and has a positively correlated RE-COT pattern. On the other hand, there is a negative correlation when the collision/coagulation process dominates because the concentration of cloud droplets changes during the process. This finding has demonstrated that the cloud growth processes can be obtained from satellite observations and retrievals. There are no other studies, however, to confirm this finding by a 3D realistic simulation. Therefore, it is necessary to repeat this finding using a real case simulation, such as a 3D realistic simulation in this study.

In addition, the RE-COT pattern has a shortcoming when considering the cloud growth stage. The problem is that cloud growth stages are discussed without consideration of the vertical structure of cloud through the RE-COT pattern. The RE values retrieved from satellites represent the cloud-top microphysical properties where cloud optical depth (COD) reaches 20~40 % of the COT of cloud layer (Nakajima and King, 1990) or 5-10 (Dong et al., 2008) from cloud top, depending on which wavelength is used ($\lambda=1.6, 2.1, \text{ or } 3.8 \mu\text{m}$). Because the vertical profiles of both COD and RE are unavailable in this study the vertical structure cannot be taken into account when considering the cloud growth stage.

1.5. Contoured frequency optical depth diagram (CFODD)

As discussed in the previous section, the RE-COT correlation pattern does not contain the cloud vertical structures because of the limitations of passive satellite remote sensing. Vertical profiles of cloud microphysical properties have been retrieved by the ground-based active radar-lidar observations (*e.g.*, Dong and Mace, 2003), satellite-borne CloudSat/Cloud Profiling Radar (CPR) (Stephens et al., 2008), and Cloud-Aerosol Lidar and Infrared Pathfinder Satellite (CALIPSO) (Winker et al., 2003, 2007).

Both CloudSat and CALIPSO have been operated in the A-Train satellite constellation (Stephens et al., 2002), which also includes the Moderate Resolution Imaging Spectro-radiometer (MODIS) onboard the AQUA satellite. Nakajima et al. (2010b) (henceforth referred to as N10) investigated the vertical structure of warm clouds from global scale observations by the CloudSat/CPR and AQUA/MODIS satellite sensors and proposed a new type of diagram, called a Contoured Frequency by Optical Depth Diagram (CFODD; presented in Fig. 1.2), to interpret the growth process of cloud droplets.

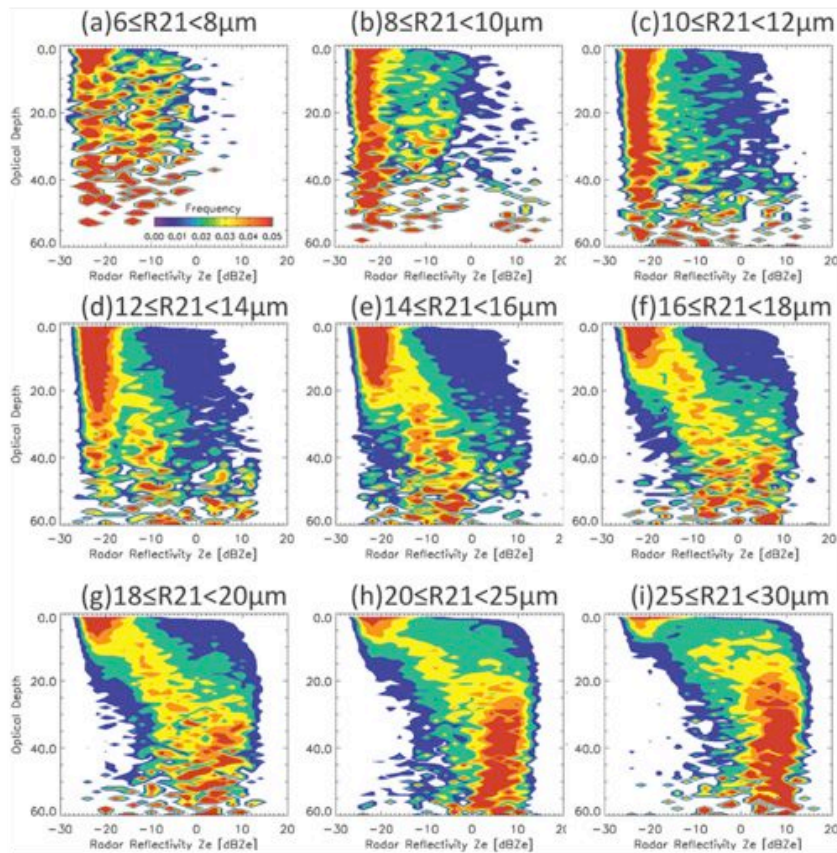


Figure 1.2. A Contoured Frequency Optical Depth Diagram (CFODD) obtained from satellite observations

(Nakajima et al., 2010b)

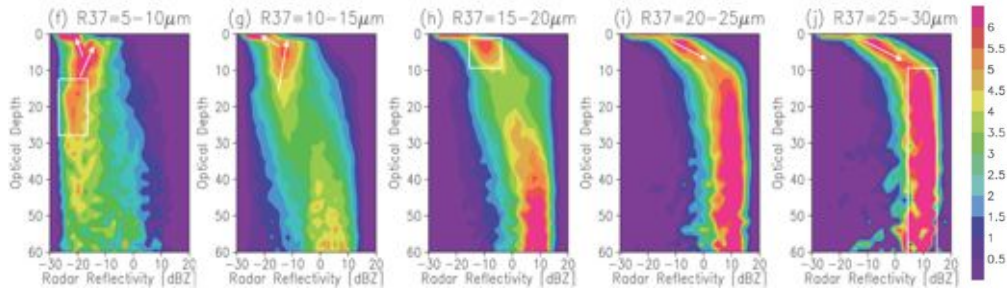


Figure 1.3 A Contoured Frequency Optical Depth Diagram (CFODD) obtained from satellite observations with an adiabatic assumption (Suzuki et al., 2010c). The unit of color shading is [% dBZ⁻¹]

Suzuki et al. (2010c; henceforth referred to as S10) also studied CFODDs (Fig. 1.3) using global observations of CloudSat and MODIS data along with an adiabatic-condensation growth model, which assume that the cloud water content increases linearly with height (Brenquier et al., 2000). Both of them claimed that cloud growth processes are represented by various characteristic patterns found in the CFODD summarized as follows.

Small particles move from the left-top area to the center-top area, as demonstrated by longer white arrow of Figs. 1.3f and 1.3g, which corresponds to condensation growth. These small particles also move from left-top area to further left-top area by evaporation at cloud top as shown by short white arrow in Figs. 1.3f and 1.3g. These small particles move from the center or left-top area to the right-bottom area because these cloud droplets grow through collision/coagulation process and finally fall down by gravity. To be more specific, the collision/coagulation process makes reflectivity large corresponding to movements from left area to right area on CFODD, whereas the gravitational falling moves cloud droplets from cloud top to bottom layer, which is demonstrated as downward arrow of Figs. 1.3i and 1.3j.

It should be recognized, however, that these results were created by accumulating several months of global observation only at around 13:30 local time of the A-train constellation orbit. A model study, therefore, is important to investigate how the regional and temporal variations of cloud characteristics are represented by the CFODD diagram and the RE-COT correlation pattern.

Although the RE-COT patterns and CFODD have their shortcomings as described above, an integrative analysis of the CFODDs and the RE-COT pattern can compensate for the problems of each diagram. In addition, model simulations can overcome the limitations of passive satellite observation and can provide detailed information that cannot be obtained by observations. Establishing a combined tool of modeling and satellite data analysis can expand the applications of

observation by next-generation satellites, *i.e.* Himawari-8 and -9, EarthCare satellite, etc. It also helps in understanding the detailed cloud growth processes.

1.6. Grid resolution of model

Although it is important to reproduce warm clouds, RE-COT pattern, and CFODD by a 3D regional SBM under a real atmospheric condition, the computational cost of SBM is too large to perform a large amount of numerical experiments. In addition to the large computational cost of SBM itself, the grid resolution of the numerical model is another problem for reproducing warm clouds by a numerical model.

Several previous studies (*e.g.*, Bretherton et al., 1999, Stevens et al., 1999) indicated that extremely fine grid resolutions (*i.e.*, from several meters to a few tens of meters) are required for simulating the entrainment at the top of warm clouds, which is one of the key factors to determine the characteristics of warm clouds (Duykerke et al., 1995; Bretherton et al., 2004). In addition, since the RE retrieved by satellite is RE near cloud top (Nakajima and King, 1990), the cloud top entrainment is a key process to determine the RE, and RE-COT pattern.

In this situation, a fine grid resolution and a large amount of computational resources are required to fully simulate warm clouds. This problem has been preventing previous studies from performing full numerical simulations of warm clouds by a 3D-SBM in a large calculation domain.

These backgrounds required the development of a low cost SBM, and how coarse grid resolutions distort the RE-COT correlation pattern and CFODD diagram needed to be investigated.

1.7. Objectives of this study

In the above, the following items have been considered: (1) the effects of warm clouds on climate through radiative processes are large and the effects of aerosols on clouds are one of the factors that produce a large uncertainty in climate prediction, (2) investigation of RE-COT patterns and CFODD is one of the important steps towards understanding the microphysical and radiative properties of warm clouds and their interactions with aerosols, (3) the interpretation by previous studies regarding various characteristic features found in RE-COT pattern and CFODD must be verified by a 3D regional model simulation under a real atmospheric condition, and (4) both SBM and extremely fine grid resolution are required for numerical simulations to fully reproduce the vertical structures of the warm cloud system.

Therefore, there are four objectives in this study. The first objective is to develop a low-cost 3D SBM. The second objective is to reproduce RE-COT patterns and the CFODD by the 3D SBM. The third objective is to investigate the effects of aerosols and other factors on the RE-COT pattern and the CFODD, and the fourth is to verify previous interpretations of the RE-COT patterns and the CFODDs. It should be emphasized that rather than simulating a detailed structure of each warm cloud, the statistical study of the microphysical characteristics of a warm cloud using the RE-COT patterns and CFODDs are focused upon, under the limited computational resources of a doctoral thesis study. With this in mind, the sensitivity of model grid resolution on the simulated cloud microphysical characteristics is investigated.

Model development is described in Chapter 2, a study of the cloud microphysical characteristics by an idealized simulation in Chapter 3, sensitivity experiments of grid resolution in Chapter 4, a study of the microphysical characteristics of warm clouds interacting with aerosols by downscaling simulation in Chapter 5, discussion in Chapter 6, and conclusion in Chapter 7.

Chapter 2. Development and improvement of regional cloud resolving model

2.1. University Of Tokyo-Aerosol Cloud Bin Model (UT-ACBM)

Two mesoscale models, named University Of Tokyo Aerosol Cloud Bin Model (UT-ACBM) and Japan Meteorological Agency Non-Hydrostatic Model (JMA-NHM), were used in this study. JMA-NHM was developed by Saito et al. (2006), and UT-ACBM was developed by Iguchi et al. (2008), Sato et al. (2009), and Choi et al. (2010).

The dynamical cores of both models adopt three-dimensional (3D) non-hydrostatic dynamics schemes that are based on a weather forecasting model developed at the Japan Meteorological Agency (JMA) (Saito et al., 2006). The basic equations adopted in JMA-NHM are summarized in Appendix A3.

The dynamical cores have two schemes to prevent the inflation of sound waves by restricting the maximum time-step: the first scheme treats waves implicitly both in horizontal and vertical directions (HI-VI scheme), and the second one treats waves explicitly in horizontal direction and implicitly in vertical direction (HE-VI scheme). In this study the HI-VI scheme is used. The Arakawa C type and Lorentz type grid systems are used for horizontal and vertical grids, respectively.

The turbulence scheme is based on the Deardorff (1980) method that is based on an assumption of isotropic turbulence structure. Thus, numerical weather prediction (NWP) models with low resolution or anisotropic grid system have Deardorff's scheme with an improved mixing length of turbulence, some tuning coefficient for the coarse grid system based on Sun and Chang (1986) and Hong and Pan (1996); henceforth referred to as Weather Forecast (WF) turbulence scheme. Both of the schemes are used as the grid resolution demands (see experimental setting of each simulation).

The radiation scheme in both models is the same, called MSTRN-X that was developed by Nakajima et al. (2000) and Sekiguchi and Nakajima (2008) (available from <http://www.ccsr.u-tokyo.ac.jp/~clastr/>).

The cloud microphysical scheme in the original version of JMA-NHM is an explicit two-water and three-ice bulk microphysics (Ikawa and Saito, 1991; Yamada, 2003). The details of this scheme are described in Saito et al. (2006). The conversion process from cloud water to rain is parameterized by the Kessler theory (*e.g.* Kessler, 1969).

The cloud microphysical scheme of the UT-ACBM, on the other hand, is a spectral-bin microphysics scheme adapted from the Hebrew University Cloud Model (HUCM) (Khain et al.,

2000) with improvements by Suzuki et al. (2006), Iguchi et al. (2008) and Sato et al. (2009, 2012a), which will be introduced in the next section. This coupled model calculates the SDFs of liquid water and six ice hydrometeors [*i.e.*, three ice crystals (plate, column, and dendrite), snowflakes, graupel, and hail] within the non-hydrostatic three-dimensional dynamical framework. The SDFs of the seven hydrometeors are represented on each spatial grid by 33 increasing mass bins that cover particle sizes (melted radii) ranging from 2.0 to 3251 μm . Only the warm phase processes of clouds, *i.e.* nucleation, condensation/evaporation, collision/coagulation, and regeneration of aerosol particles (see section 2.2) are calculated in this study because the temperature of the top of warm cloud was almost over 273 K.

In the modeling nucleation process calculation, all aerosols larger than a critical radius are transferred from the aerosol bin to the cloud droplet bin. The aerosols, whose radii are smaller than the range of cloud particle sizes (2.0 μm), are transferred from aerosols bins to the smallest cloud droplets bin. The aerosols, while, whose radii are in the cloud bin size range, are transferred from the aerosol bins to cloud bins corresponding to aerosol size. The critical radius (r_{crit}) of the aerosols is calculated by the Köhler theory (*e.g.*, Rogers and Yau, 1989) as:

$$r_{crit} = \sqrt{\frac{4}{27} \frac{A^3}{B S_w}}, \quad A \approx \frac{3.3 \times 10^{-5}}{T} (\text{cm}), \quad B \approx \frac{4.3\nu}{M_{ccn}} \left(\frac{4\pi\rho_{ccn}}{3} \right) (\text{cm}), \quad (2-1)$$

where T is the temperature, ρ_{ccn} is density of an aerosol particle, M_{ccn} is molecular weight of the aerosol, ν is Van't Hoff factor (*e.g.*, Low, 1969), and S_w is supersaturation over water. The notation of symbols is written in Appendix A6.

Condensation/evaporation growth is calculated by solving an equation (*e.g.*, Rogers and Yau, 1989) as:

$$\frac{dm}{dt} = \frac{4\pi r S_w}{F}, \quad F = \frac{R_v T}{e_w D_v} + \frac{L_w}{K_a T} \left(\frac{L_w}{R_v T} - 1 \right), \quad (2-2)$$

where m is the mass and radius of the hydrometeors, r is radius of hydrometeors, R_v is the gas constant of vapor, D_v is diffusivity of water vapor, e_w is saturation vapor pressure over water, K_a is thermal conductivity of air, and L_w is specific latent heat of vaporization.

Collision and coagulation growth is calculated using the stochastic collision equation (SCE) (*e.g.*, Pruppacher and Klett, 1997),

$$\frac{\partial f(m)}{\partial t} = \int_0^{\infty} f(m)K(m,m')f(m')dm' - \int_0^{m/2} f(m-m'')K(m,m'')f(m'')dm'' \quad (2-3)$$

$$K(m,m') = \pi \{r(m) + r'(m')\} |V(m) - V(m')| E_{coll}(m,m') E_{coal}(m,m')$$

where f is the SDF of hydrometeors, V is terminal velocity, E_{coll} is collision efficiency, and E_{coal} represents the coalescence efficiency. The values of E_{coll} and E_{coal} are adopted from the study of Khain et al. (2000).

The SDFs of five chemical species of aerosols (*i.e.*, sulfates, sea salt, dust, black carbon (BC), and organic carbon (OC)) are treated (Choi et al., 2010). The aerosol particle radius is discretized into 17 bins increasing mass bins that cover particle sizes ranging from 1.3 nm to 7.62 μm for each of these species. Initial SDFs of aerosols are given by multi-modal log-normal distribution as follows:

$$f_a(r_a) = \sum_{k=1}^{M_{spc}} \sum_{i=1}^{N_m} \frac{N_{spr} A_i}{\sqrt{2\pi} \sigma_i} \exp\left[-\frac{(\ln r_a - \ln r_{0i})^2}{2\sigma_i^2}\right], \quad (2-4)$$

where f_a is number concentration (SDF) of aerosol and r_a is radius of aerosol particle. N_m , which is set to 3 (Choi et al. 2010), is the number of modes, and A_i , r_{0i} , and σ_i are mode fraction, mode radii, and geometrical standard deviation, respectively (see Table 2.1 for details of A_i , r_{0i} , and σ_i).

Table 2.1. Values of A_1 , A_2 , A_3 , r_{01} , r_{02} , r_{03} , σ_1 , σ_2 , and σ_3 of equation (2-4). OC, BC, SU, DU, and SA means organic carbon, black carbon, sulfate, dust, and sea salt respectively.

	OC	SA	SU	DU	BC
A_1	0.4286	0.965	0.8994	0.8542	0.4286
A_2	0.5714	0.035	0.1002	0.1457	0.5714
A_3	1×10^{-6}	0.0	0.0004	0.0001	1×10^{-6}
r_{01} [μm]	0.005	0.035	0.021	0.05	0.005
r_{02} [μm]	0.08	0.41	0.065	0.27	0.08
r_{03} [μm]	2.5	1.0	0.352	4.0	2.5
σ_1	1.5	1.92	1.51	1.65	1.5
σ_2	1.7	1.7	1.78	2.67	1.7
σ_3	1.65	1.5	1.23	2.4	1.65

The number of aerosol chemical species M_{spc} , in the original formulation is set to 5, but it is set to 1 in this study: and the aerosol species is assumed to be only sulfate for simplicity of experimental setup and limitation of parameterization of the regeneration process of aerosol used in this study (see section 2.2 on the regeneration process).

2.2. Improvement of UT-ACBM in this study

In this section several improvements developed in this study for UT-ACBM are presented. Firstly, a scheme based on the Monte-Carlo integration method is implemented for calculating the SCE (eqs. 2-3) to reduce computational costs of SBM. The details of this scheme are presented in Sato et al. (2009) and Appendix A8. Secondly, the regeneration of aerosols by complete evaporation of water droplets based on Feingold et al. (1996) is introduced because several previous studies indicated the importance of this process (*e.g.*, Ivanova and Leighton, 2008) to reproduce warm clouds. This scheme is based on the assumption that the complete evaporation of a droplet generates an aerosol particle (Mitra et al., 1992). Two types of parameterization are used for determining the SDF of regenerated aerosol. The SDF of the first parameterization is given as:

$$R_k(t) = N(t) \frac{\phi_k(t)}{\sum_{k=1}^{n_a} \phi_k(t)}, \quad \phi_k(t) = \frac{\bar{N}_k(0) - \bar{N}_k(t)}{\bar{N}_k(0)}, \quad (2-5)$$

where $\bar{N}(t)$ is the domain-averaged number concentration of aerosol at time t , $N(t)$ is the total number concentration of regenerated aerosol at time t , n_a is the number of aerosol bins, and $R_k(t)$ is the regenerated aerosol number concentration of the k -th aerosol bin at time t .

This parameterization is based on a concept that the size of regenerated aerosols is usually larger than the aerosol particle before activated to cloud droplet. The SDF of the other parameterization is given by the same SDF of initial time. These parameterizations are used as the demand for an experimental setup. The parameterizations, however, cannot calculate the SDF of regenerated aerosol explicitly, and can treat only one species of chemical component because the chemical species of regenerated aerosol cannot be determined. To overcome this limitation of parameterization, multi-dimensional spectral bin microphysical schemes, which calculate the mass of aerosols in cloud droplets, have been developed recently (*e.g.* Chen and Lamb, 1994, Xue et al., 2011).

Similar to these schemes, the spectral bin microphysical scheme is expanded to a two-dimensional

(2D) spectral microphysical bin scheme, which calculates the mass of aerosols in hydrometeors explicitly, as well as the mass of hydrometeors. This scheme calculates changes of the aerosol mass in cloud droplets through the collision/coagulation process of cloud droplets, but does not calculate chemical reaction of solute aerosols in cloud droplets. Since the computational (CPU) cost of this 2D spectral bin scheme is too large to conduct sensitivity experiments, this 2D spectral bin scheme is only used for checking the validity of the regeneration scheme, as discussed in Appendix A1.2.

2.3. Radar simulator

In this study model simulations are compared with satellite observation in terms of radiance and radar reflectivity. To calculate the radiance and the radar reflectivity from the model results, two radar simulators are used to calculate radiance and reflectivity at the corresponding wavelengths of satellite sensors. One is a radar simulator developed by Okamoto et al. (2003, 2007, and 2008) called EarthCARE Active Sensor (EASE) simulator. This simulator calculates the radar reflectivity of 95 GHz corresponding to the signal of Cloud Profiling Radar (CPR) on board the CloudSat satellite. The radar signal (Z_e) is given as:

$$Z_e = Z_{e,true}(z_i) \exp[-2\tau_{d,i-1/2}(z_{i-1/2})] \exp\left[\frac{\exp(-2\sigma_{ext,ra}(z_i)\Delta z) - 1}{-2\sigma_{ext,ra}(z_i)\Delta z}\right], \quad (2-6)$$

$$Z_{e,true}(z_i) = \frac{\lambda^4}{\pi^5 |K_r|^2} \left[\int_{r_{min}}^{r_{max}} \frac{df(r)}{dr} C_{bk}(r, z_i) dr \right]$$

where $\lambda (=95GHz)$ is the wavelength of CPR, $C_{bk}(r, z_i)$ is backscattering cross section, $\sigma_{ext,ra}$ is extinction coefficient, Δz is vertical grid interval of model, and i is model layer number. The variables z_i and $\tau_{d,i}$ denote the altitude and optical depth at the center of the i -th cloud layer, respectively, and $z_{i-1/2}$ and $\tau_{d,i-1/2}$ denote the altitude and optical depth at the bottom boundary of the i -th layer, respectively. K_r is estimated from the complex refractive index of water m_r by $|K_r| = |(m_r^2 - 1)/(m_r^2 + 2)|$. $Z_{e,true}$ is defined as the “true” radar reflectivity (and has dimensions of $mm^6 m^{-3}$). In this study, the logarithmic form of Z_e is used to describe the radar reflectivity $dBZ_e = 10 \log_{10}(Z_e)$.

The other simulator is also a radar simulator called Joint Simulator for satellite sensors (J-simulator) (Hashino et al. 2011). This simulator calculates radiances at visible and infrared wavelengths of satellite-borne imagers through solving the radiative transfer equation by using a radiation code Rstar-6B (Nakajima and Tanaka, 1986, 1988, and Sekiguchi and Nakajima 2008,

OpenCLUSTER web site; <http://www.ccsr.u-tokyo.ac.jp/~clastr/software.html>). This code applies combined Adding method and Discrete Ordinate Method (DOM) for each layer and calculates radiative fluxes at user-defined angles and optical depths. The profile of temperature, relative humidity, wind field, density of water, the inputs of the simulator, are given by the model results and Japanese Reanalysis 25 data (JRA-25) (Onogi et al., 2007).

Chapter 3. Investigation of the CFODD diagram using UT-ACBM model

3.1. Introduction

In this chapter the characteristics of cloud processes in the CFODD diagram using the UT-ACBM simulation results are investigated. As mentioned in section 1, CFODD was originally proposed by N10. The CFODD was constructed from MODIS retrieved RE value onboard the AQUA satellite and COD obtained by the 95 GHz CloudSat/CPR reflectivities. S10 also calculated CFODD (*e.g.*, Fig. 3.1) from CPR reflectivity and MODIS derived RE, and interpreted the characteristic patterns appearing in the CFODD by using an adiabatic condensation growth model (Brenguier et al., 2000). Both N10 and S10 suggested that CFODD represents various dominant growth processes depending on cloud stage. The cloud growth process appearing in the CFODD can be summarized as follows.

At first small cloud droplets are generated by nucleation process near the cloud base. This stage is seen in the left-bottom area of small RE category in the CFODD (Fig. 3.1a). Then, these small particles move from the left-bottom area to the left-top area in the CFODD with increasing RE by updraft (arrow (i) in Fig. 3.1a, referred to as updraft mode), however, there is no noticeable increase in radar reflectivity because the RE is still small at this stage.

Secondly, the radar reflectivity increases with increasing RE through the condensation process and the small particles move from the left-top area to the center-top area in the CFODD, as demonstrated by arrow (ii) of Fig. 3.1b; henceforth, referred to as condensation mode.

Thirdly, these small particles move from the center or left-top area to the right-bottom area in the

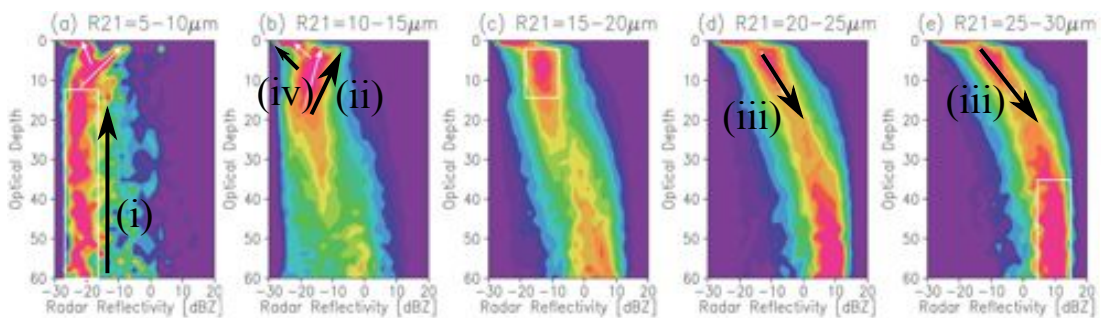


Figure 3.1. Contoured Frequency Optical Depth Diagrams (CFODDs) classified by the MODIS retrieved cloud-droplet effective radius at $\lambda=2.1 \mu\text{m}$ wavelength $r_{2.1}$ (a) 5–10 μm , (b) 10–15 μm , (c) 15–20 μm , (d) 20–25 μm , and (e) 25–30 μm over the ocean area from June to August, 2007. Cited from Suzuki et al. (2010c) and rearranged. Arrows (i), (ii), (iii), and (iv) represent “updraft”, “condensation”, “collision”, and “entrainment” pattern, respectively.

CFODD, because these cloud droplets grow through a collision/coagulation process and finally fall down by gravity. To be more specific, the collision/coagulation process makes reflectivity larger corresponding to movements from left area to right area in the CFODD, whereas the gravitational falling moves cloud droplets from cloud top to bottom layer, which corresponds to movement from smaller COD to larger COD area in the CFODD. These processes are displayed as arrows (iii) in Figs. 3.1d and 3.1e; henceforth, referred to as collision mode.

The other mode in S10 was introduced as evaporation process at the cloud top due to cloud-top entrainment, which is seen as arrow (iv) of Fig. 3.1b; henceforth, referred to as entrainment mode.

Although this diagram (CFODD) and interpretation is novel, the CFODDs constructed by previous studies were obtained from accumulating 3-month results of global MODIS and CloudSat observations with 1.1km (480m) horizontal (vertical) resolution at local time of around 13:30. Thus, the important temporal evolutions appearing in the CFODD cannot be obtained by satellite observations. To investigate the cloud growth processes and to verify the interpretation by N10 and S10, it would be better to rely upon numerical models.

The SBM are used to reach this goal with the following three objectives: The first objective is to reproduce the satellite-derived CFODD, the second objective is to investigate how CFODDs evolve with time, and the final objective is to verify the interpretation of N10 and S10 using data simulated in SBM.

3.2. Experimental setup and satellite data

3.2.1. Model description

The 3D-SBM (*i.e.* UT-ACBM) is used for experiments of this section. A detailed description is shown in section 2 of this paper. The turbulence scheme of Deardroff (1980) is used for the experiments, and parameterization of Feingold et al. (1996); shown in eq. (2-5) is used in aerosol regeneration scheme. In addition, to simplify the experimental setup, a simple radiation scheme and a simple aerosol size distribution shown in the next subsection are used, instead of original radiation scheme (*i.e.* MSTRN-X) and aerosol size distribution (*i.e.*, Choi et al. 2010) of UT-ACBM, in the experiments of this section.

3.2.2. Experimental setup

The experimental setup of this section is based on the DYCOMS-II RF02 modeling study (Ackermann et al., 2009) targeting nocturnal stratocumulus during the summer season off the coast

of California, and their experimental setup was based on aircraft in situ measurements over this region. Although the DYCOMS-II RF02 modeling study was conducted to simulate with an initial wind velocity based on aircraft observation, no initial wind is set, following Wang and Feingold (2009a). Thus, the initial conditions are horizontally uniform and no wind and the vertical profiles of the potential temperature, relative humidity, and vapor mixing ratio are given in Fig. 3.2.

Calculations begin without any cloud liquid water, with a super saturated layer from 400–795 m, which corresponds to the simulated cloud layer. A horizontally and vertically uniform aerosol layer is assumed, with a single-modal log-normal size distribution whose geometrical standard deviation and mode radius are set as 1.5 and 0.1 μm , respectively.

Although the original version of UT-ACBM treats aerosol particle radius discretized into 17 increasing mass bins that cover particle sizes ranging from 1.3 nm to 7.62 μm , the version used in this section discretizes the aerosol particle radius into 13 increasing mass bins that cover particle sized ranging of aerosol from 1.3 nm to 0.767 μm in this experiment for simplicity. All activated aerosols are transferred into the smallest bin of cloud particles, since the aerosol particle size is always smaller than smallest size of cloud particles (*i.e.* 2.0 μm) in this experiments.

The number concentration of the aerosol is set to 60 cm^{-3} (pristine experiments) and 500 cm^{-3} (polluted experiments) for sensitivity experiments. The chemical component of the aerosol is sulfate.

Calculations are performed for 6 hours with a time step of $dt = 0.5$ s for horizontal (vertical) resolution of 50 (20) m, *i.e.*, $600 \times 600 \times 75$ grids within a domain of $30 \times 30 \times 1.5$ km with a horizontally periodic lateral boundary condition.

To drive and maintain warm clouds in the domain, a random perturbation of the potential temperature and vapor mixing ratio is initially applied. Forcing of the radiation, large-scale

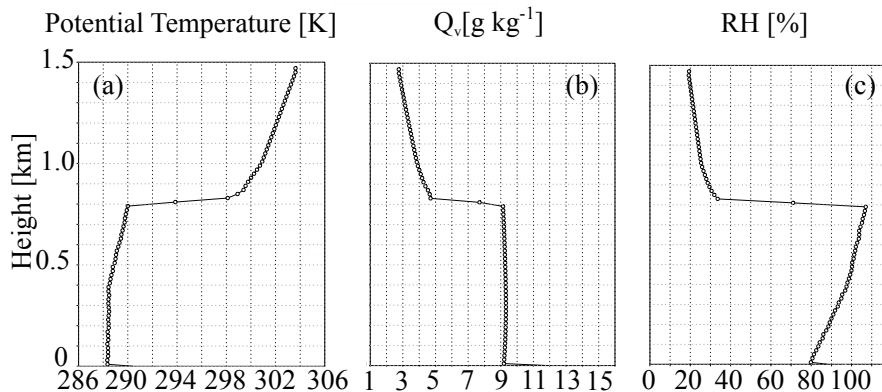


Figure 3.2 Initial profiles of (a) potential temperature, (b) vapor mixing ratio, and (c) relative humidity of water.

subsidence, and surface heat flux is also incorporated, based on the forcing used in Ackermann et al. (2009). Random perturbations of temperature and water vapor (0.1 K and 0.025 g kg⁻¹), are given in the layer below the cloud-top height, $z_{top} = 795$ m, at $t = 0$. The large-scale vertical wind is computed as $w_{LS} = -D_L z$ with $D_L = 3.75 \times 10^{-6}$ s⁻¹, and is used as a source term for each prognostic variable η as $-w_{LS} \partial \eta / \partial z$. The radiative heating rate is computed at every time step from the divergence of a long-wave radiative flux profile in each model column using the parameterization by Stevens et al. (2005),

$$F(z) = F_0 \exp[-Q_r(z, z_{model_top})] + F_l \exp[-Q_r(0, z)] + a \rho_l C_p D_L H_v (z - z_{top}) [0.25(z - z_{top})^{4/3} + z_{top}(z - z_{top})^{1/3}]. \quad (3-1)$$

$$Q_r(z_1, z_2) = \int_{z_1}^{z_2} \kappa \rho q_l dz$$

In eq. (3-1), $F_0 = 70$ W m⁻² and $F_l = 22$ W m⁻², $\rho_l = 1.12$ kg m⁻³, $C_p = 1004$ J kg⁻¹ K⁻¹, H_v is the Heaviside step function, z_{top} and z_{model_top} are the cloud-top heights and model top heights, $\kappa = 85$ m² kg⁻¹, $a = 1$ K m^{-1/3}, and q_l and ρ are the liquid water mixing ratio and air density, respectively. The upward sensible and latent heat fluxes from the surface are given as 93 W m⁻² and 16 W m⁻² at each time step. The upward surface momentum flux is computed as $-uu^*/|u|$, where the wind components u and magnitude $|u|$ are defined locally, and the friction velocity is fixed at $u^* = 0.25$ m s⁻². To avoid errors caused by model spin-up, only the simulated results from 2.5–6 h are used to construct the CFODDs.

The model simulates clouds whose geometrical depth is about 400~500m in a small (30 x 30 km²) domain in this experimental setup shown above. The CFODDs in the previous studies were constructed from global observations of warm clouds. Additional global scale experiments must be performed in future to extend our understanding of the cloud evolution on a global scale.

3.2.3. Calculation of CFODD from model results

Constructing a CFODD, the simulated cloud optical depth (COD) at each model height and the RE values corresponding to those derived from the MODIS satellite are required. The COD, as denoted by $\tau(z)$ or τ_d , is calculated as

$$\tau_d(z) = \tau(z) = \frac{3}{2\rho_w} \int_{z_{top}}^z \frac{LWC(z)}{r_{eff}(z)} dz, \quad (3-2)$$

where ρ_w , is the density of water, r_{eff} is RE, z_{top} is cloud-top height, and z is height. LWC is the liquid water content, defined by

$$LWC(z) = \int_{r_{min}}^{r_{max}} \frac{4}{3} \pi \rho_w r^3 f(r, z) dr, \quad (3-3)$$

where f is the SDF of a cloud droplet, r is radius of a cloud droplet, r_{max} is the maximum radii of cloud droplets, and r_{min} is minimum radii of cloud droplets in the model. RE (r_{eff}) is defined by

$$r_{eff}(z) = \frac{\int_{r_{min}}^{r_{max}} r^3 f(r, z) dr}{\int_{r_{min}}^{r_{max}} r^2 f(r, z) dr}. \quad (3-4)$$

The COT, denoted by τ_c , is then calculated as

$$\tau_c = \frac{3}{2\rho_w} \int_{z_{top}}^{z_{bottom}} \frac{LWC(z)}{r_{eff}(z)} dz, \quad (3-5)$$

where z_{bottom} is the cloud bottom height.

N10 used the RE values retrieved from the 2.1 μm ($r_{2.1}$) or 3.7 μm ($r_{3.7}$) channel of MODIS. They indicated that the 3.7 μm (2.1 μm) channel-retrieved RE values corresponds to the height at the optical depth of 8 (15) from the cloud top. In this study, the 3.7 μm channel-retrieved RE is used, denoted by $r_{3.7}$, for calculation of the CFODD. $r_{3.7}$ can be calculated from the following equation (Platnick, 2000; Nakajima et al., 2010a):

$$r_{3.7} = \int_0^{\tau_1} r_{eff}(\tau'(z)) w_\lambda(\tau', \tau_1) d\tau', \quad (3-6)$$

where $\tau_1 = 8$ as used in Nakajima et al. (2010a), and w_λ is the weight function suggested by Platnick

(2000). To calculate the radar reflectivity corresponding to CPR signal the EASE simulator was used.

3.2.4. Satellite data

To investigate the regional differences between model-derived CFODDs and satellite-derived ones, CFODDs from satellite observations are also constructed. The CFODDs obtained from satellite observations over the Californian region (20°–40°N, 115°–135°W) and the East Asian region (20°–40°N, 120°–140°E) are constructed in this study. The former is one of the pristine regions over the globe, and the latter is one of the polluted regions (Nakajima et al., 2001).

The radar reflectivity profiles are obtained from the 2B-GEOPROF product of the CloudSat Project (*e.g.*, Mace et al., 2007) for the June–August (JJA) in 2007. The COT and RE are retrieved from a CPR-matched MODIS multispectral analysis based on the Comprehensive Analysis Program for Cloud Optical Measurements (CAPCOM; NN95; Kawamoto et al., 2001) algorithm. 2.1 μm radiances (Nakajima et al., 2010a) are used in this analysis.

The horizontal and vertical resolutions of the CloudSat CPR observation are 1.1 km and 240 m, respectively. The COD is retrieved by the method of S10, which uses COT and the geometrical depth (H_c) of the cloud obtained from CPR radar reflectivity. Cloud top and bottom heights are determined by the highest and lowest radar bins where the radar reflectivity is larger than the minimum sensitivity of CloudSat CPR (-30 dBZe). The COD at a height (h), measured from the cloud bottom, is calculated by COT and H_c as

$$\tau(h) = \tau_c \left[1 - \left(\frac{h}{H_c} \right)^{5/3} \right]. \quad (3-7)$$

The derivation of eq. (3-7) is given in S10 and Appendix A9. To construct CFODDs for the same conditions as in S10, the procedures described below are applied to the satellite data.

Because the sensor on the MODIS satellite is not sensitive to optically thin clouds, only reflectivity profiles associated with COTs larger than 1 are used for constructing CFODDs. To restrict analyses to warm cloud cases, the reflectivity profiles with cloud-top temperatures higher than 273.15 K are selected, where both MODIS and the European Center for Medium-range Weather Forecasts (ECMWF)-AUX provided temperature profiles matching the CPR echo top. In

addition, only single-layer cloud reflectivities are used for this analysis.

Although the details of satellite data used for constructing CFODD are described, an observational limitation of CPR, whose wavelength is $\lambda=94\text{GHz}$, should be noted. Even though the 94GHz radar (W-band) is an effective tool to detect cloud droplet from satellite and ground remote sensing, they often cannot detect the clouds without large cloud droplet *i.e.*, drizzle. Further, it is difficult for them to determine the base height of cloud with large cloud droplet (*i.e.*, drizzle). In addition, the ground clutter prevents the radars from detecting the signal of warm shallow cloud off the coast of California.

The signals selected from raw data of CPR reflectivity for making CFODD are not always the signals of warm clouds off the west coast of California; in addition, the cloud base heights retrieved from CPR are not always correct.

In spite of these limitations, this research is considered as a step forward in understanding CFODD, and is very important because there is no other study, to my knowledge, to reproduce CFODD from 3D-SBM data and compare the model-derived CFODD with satellite-derived CFODD.

3.3. Comparison of CFODD between model simulations and observation

Figure 3.3 presents the spatial distribution of cloud albedo (A_{lb}) calculated by the formula of Savic-Jovicic and Stevens (2008) as follows:

$$A_{lb} = \tau_c / (6.8 + \tau_c) . \quad (3-8)$$

Figure 3.3 also demonstrates the spatial distributions of the vertical wind velocity field below the cloud layer (*i.e.*, 200 m height from the surface) and the simulated surface precipitation rate at 6 h after the initiation of the calculation.

It is seen from Fig. 3.3 that high (low) albedo values are obtained in the polluted (pristine) experiment. Precipitation occurs frequently in the pristine experiment. In the polluted case, only a little precipitation occurs and optically deep clouds are represented. The domain-averaged RE of the pristine experiment is larger than the polluted experiments (figure not shown). From this result, it appears that cloud droplet size is decreased by large amounts of aerosol and the generation of precipitation is suppressed.

These characteristics of results found in both experiments are also manifested in the vertical

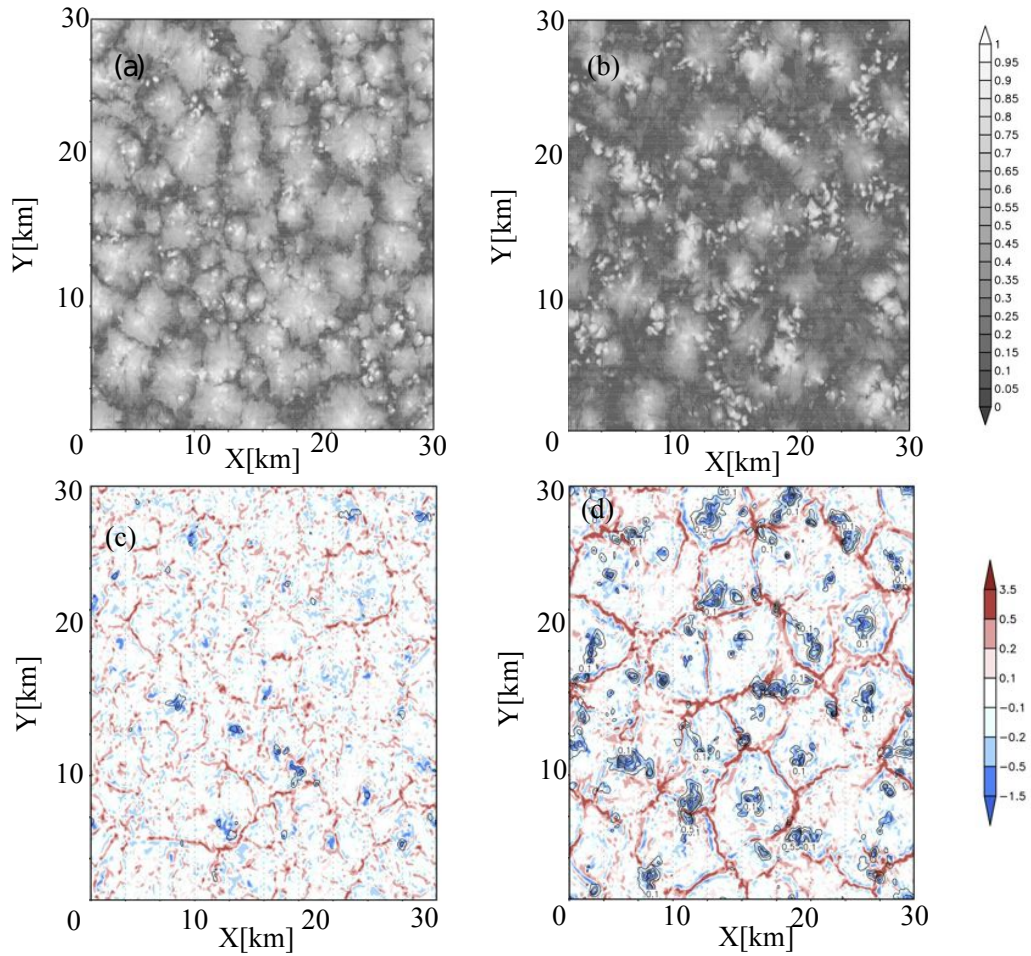


Figure 3.3 Spatial distributions of the cloud albedo obtained from (a) polluted and (b) pristine experiments, and areal distributions of the vertical wind velocity below the cloud layer (200 m) [m s^{-1}] (shade) and surface precipitation (contour) obtained from (c) polluted and (d) pristine experiments. Contours values are 0.1, 0.5, 1.0, 2.5, 5.0, and 10.0 mm day^{-1} .

profiles of dynamical variables. Figure 3.4 represents vertical profiles of liquid water content, relative humidity, potential temperature and vapor mixing ratio averaged over the whole calculation domain at 6 h after the start of the calculation.

Fig. 3.4a shows that liquid water content (LWC) in the polluted experiment is larger than that in the pristine experiment. In the pristine experiment, LWC broadens to a lower layer, which corresponds to the existence of drizzle particles. This is consistent with the occurrence of precipitation in the pristine experiment. As well as liquid water content (represented as Fig. 3.4a), high relative humidity broadens to a lower layer in the pristine experiment (as shown in Fig. 3.4b), which results from drizzle in the pristine experiment.

It is also found from Figs. 3.4c and 3.4d that cloud top height in the pristine experiment is lower

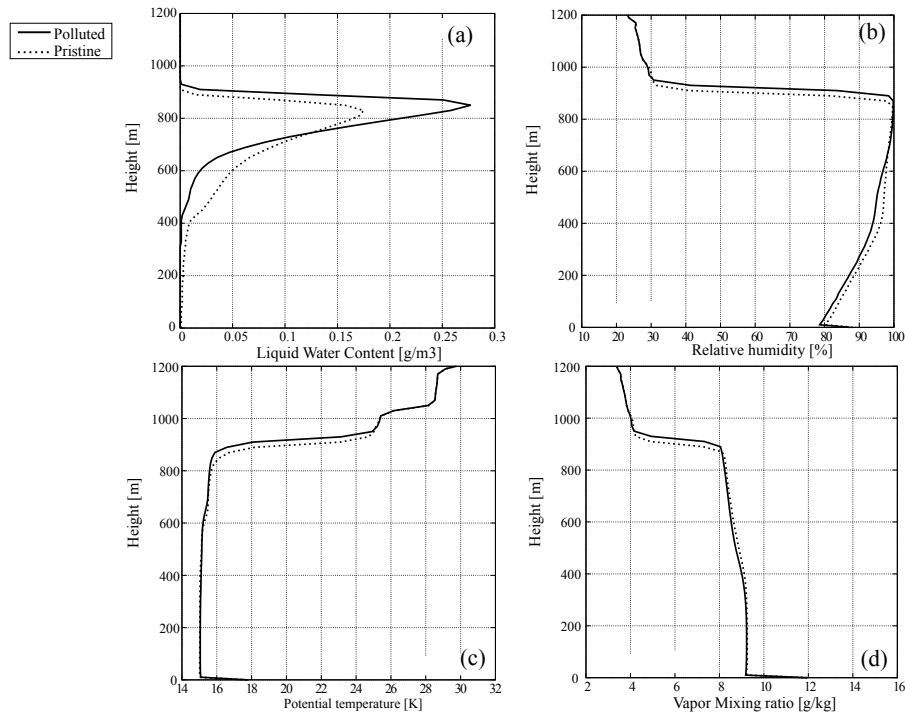


Figure 3.4. The vertical profiles of (a) liquid water content, (b) relative humidity, (c) potential temperature, and (d) vapor mixing ratio averaged over whole calculation domain at $t=6$ after the starting time of calculation simulated by (solid line) polluted experiment and (dotted line) pristine experiment.

than that in the polluted experiment, which results from the precipitation occurring in pristine experiments. The precipitation transfers cloud water to the surface and reduces LWC in the cloud layer, which results in weak turbulence and entrainment. The weak entrainment lowers the cloud top height.

This cloud structure and its aerosol dependence are the same as those found by Wang and Feingold (2009b), and are also consistent with the proposed cloud field changes caused by aerosol effects (Twomey, 1974; Albrecht, 1989).

Figure 3.5 represents the CFODDs obtained from model results at $t = 6$ h, while Fig. 3.6 represents the CFODDs obtained from satellite observations over the East Asian region (Figs. 3.6a–e) and the Californian coast region (Figs. 3.6f–j). It is found from Figs. 3.1 and 3.6 that CFODD obtained from regional observation indicates different characteristics from that obtained from global scale observation (*e.g.*, there are no signals on optically deep areas in Fig. 3.6f).

The CFODDs in Figs 3.5a–e are obtained from the polluted experiment where there are relatively small numbers of large particles (*i.e.*, $RE > 20 \mu\text{m}$) and none with $RE > 25 \mu\text{m}$. The radar reflectivity of small particles (*i.e.*, $RE < 15 \mu\text{m}$) is almost constant in a range of COD 10–60, as

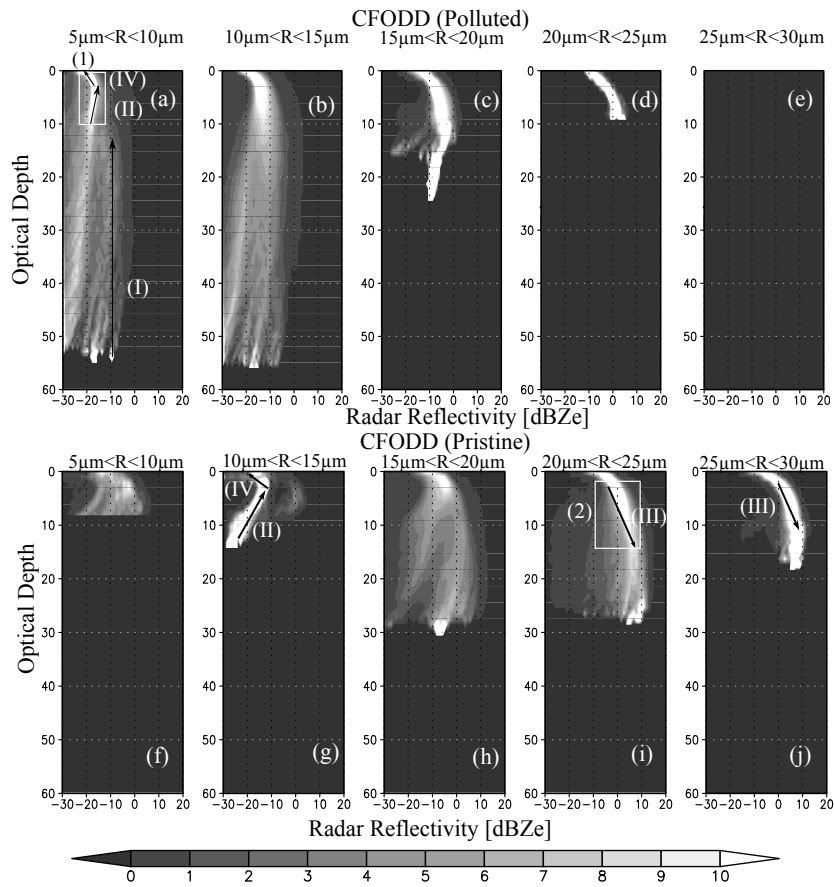


Figure 3.5 Contoured Frequency Optical Depth Diagrams (CFODDs) at $t = 6$ h obtained from (a–e) polluted, (f–j) pristine experiments, divided by r_{eff} of (a, f) 5–10 μm , (b, g) 10–15 μm , (c, h) 15–20 μm , (d, i) 20–25 μm , and (e, j) 25–30 μm . Arrows (I), (II), (III), and (IV) represent “updraft”, “condensation”, “collision”, and “entrainment” pattern, respectively. Rectangle (1) and (2) represent areas where size distribution functions (SDFs) of hydrometeor are used for box model calculation.

illustrated by the arrow (I) in Fig. 3.5a.

This characteristic was also found by S10 that used satellite observations (arrow (i) in Fig. 3.1a). S10 suggested that this mode reflects the movement of cloud droplets from cloud bottom to cloud top by upward motion of air, *i.e.* updraft mode. In the upper part of cloud cells, the radar reflectivity of fine particles (*i.e.*, $R_E < 10 \mu\text{m}$) decreases as the COD decreases from 3 to 0, as shown by arrow (IV) in Fig. 3.5a, after displaying an increasing tendency in the deeper part of the cloud layer, as shown by arrow (II) in Fig. 3.5a.

These patterns were also found in satellite observations by S10 in their CFODDs, as shown by arrows (ii) and (iv) in Fig. 3.1. This corresponds to the condensation growth of uplifted cloud droplets, *i.e.*, condensation pattern, and corresponds to the evaporation of cloud droplets invoked by

cloud-top entrainment, *i.e.*, entrainment pattern.

Figures 3.5f–j represent the CFODDs obtained in the pristine experiment. In this case, small cloud droplets (*i.e.*, $RE < 15 \mu\text{m}$) do not exist in the optically deep region, whereas the radar reflectivity of large particles (*i.e.*, $RE > 20 \mu\text{m}$) increases with the COD, as shown by arrows (III) in Figs. 3.5i and 3.5j. N10 and S10 interpreted this pattern as the collision/coagulation processes during the growing process of cloud droplets, and then these large cloud droplets fell by gravity to the lower part of the CFODD, *i.e.*, collision pattern. This pattern is not clear in Figs. 3.5d and 3.5e for the polluted case. Notice that the patterns (II) and (IV) in Fig. 3.5a are also produced in Fig. 3.5g, but the pattern (I) in Figs. 3.5a (*i.e.*, the updraft pattern) is not produced in the pristine case.

Figures 3.6a–e represent the CFODDs obtained from satellite observations over the East Asian region, where the amount of aerosol is significantly larger than the global average (Nakajima et al., 2001; Remer et al., 2005; Matsui et al., 2006). These correspond to the polluted condition in this study. In Fig. 3.6a, a constant radar reflectivity area (*i.e.*, the updraft pattern) is produced, with a slightly increasing reflectivity with decreasing COD. This behavior is also simulated by the model (Fig. 3.5a).

Figures 3.6f–j are the CFODDs obtained from satellite observations off the west coast of California, where the amount of aerosol is small, corresponding to the pristine condition in this study. In this case, the collision pattern is clear, whereas the updraft pattern cannot easily be discerned. This structure is also reproduced by the model-derived CFODDs in the pristine experiment (Figs. 3.5f–j).

The model-derived CFODD reproduces the characteristics of satellite-derived CFODDs of each aerosol condition; COD of simulated clouds are lower than observation. It is seen from Figs. 3.5 and 3.6 that the range of simulated COD is from 0 to 30, while the COD obtained from satellite observation reaches over 50 in both regions (*i.e.*, California and East Asia). The difference of COD between model results with satellite observations could be due to the experimental setup.

The experimental setup of this study is based on the DYCOMS-II experiment, which was targeted on nocturnal stratocumulus off the west coast of California. The satellite data used for making CFODD is obtained from global scale observation. The COD of stratocumulus off the west coast of California are smaller than global average. This could be one reason for this difference. Conducting a global scale simulation for making CFODD from a global model could explain or shed some light on this shortcoming.

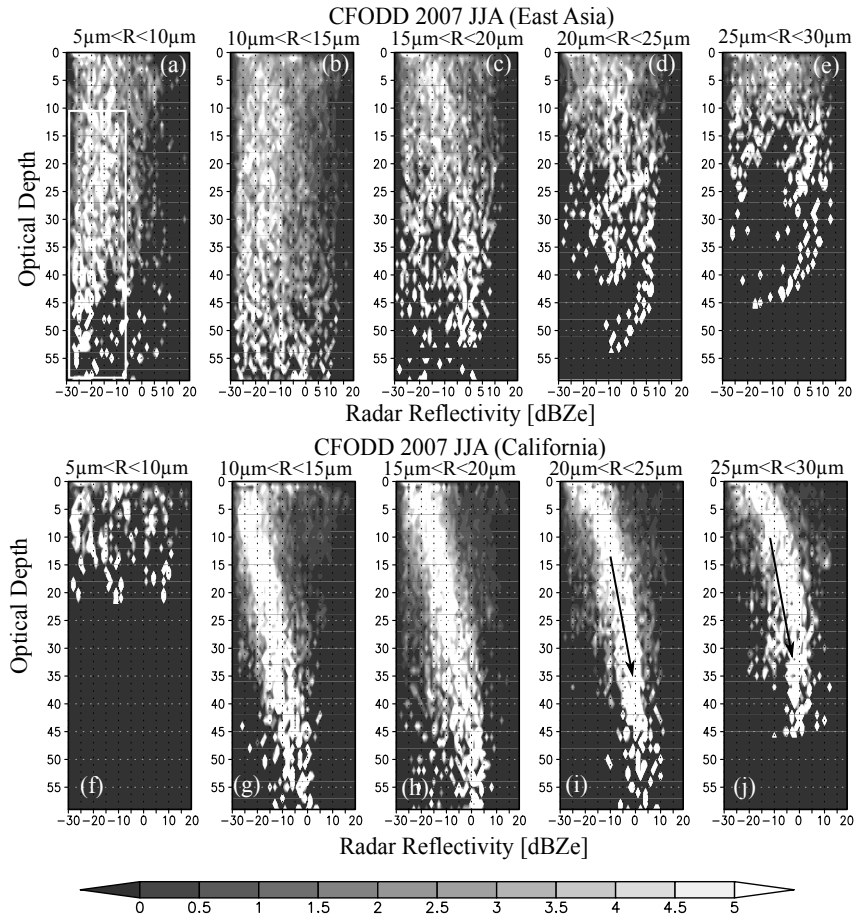


Figure 3.6 Contoured Frequency Optical Depth Diagram (CFODDs) obtained from satellite observations in (a–e) East Asia (20° – 40° N, 120° – 140° E), and (f–j) California (20° – 40° N, 115° – 135° W), divided by r_{eff} of (a, f) 5–10 μ m, (b, g) 10–15 μ m, (c, h) 15–20 μ m, (d, i) 20–25 μ m, and (e, j) 25–30 μ m. Rectangle in (a) and arrows in (i,j) represents “updraft” and “collision” pattern, respectively

3.4. Cloud growth process represented on CFODD

In the previous section, it has been confirmed that the CFODDs constructed from model simulation data qualitatively reproduce the characteristics of satellite-derived CFODDs. From this confirmation, the present model can be used to identify the dominant growth processes characterized by the CFODD. This is one of the objectives of this section.

A cloud microphysics zero-dimensional box model is applied to the simulated cloud field to identify the dominant processes that characterize each of the cloud layers composing the CFODD. This box model is a stand-alone version of the microphysical module of the UT-ACBM.

It calculates temporal evolution of SDFs using only the cloud microphysical processes. It also

assumes that the cloud dynamical states, such as temperature, pressure, and super saturation, are given and fixed. In the study, the initial values of temperature and pressure are set to 284 K, 800 hPa, which correspond to the mean atmospheric conditions of the cloud layer calculated by the present 3D model and supersaturation is set to 0.5%. Although the supersaturation is larger than that of simulated cloud layer, it is difficult to identify the cloud growth process by calculation result under small supersaturation condition, thus the supersaturation value is set to 0.5 %.

Initial SDFs are given by the averaged SDF from the 3D model. Box model calculations are performed for 10 min with a time step of $dt = 0.5$ s. To determine which process is dominant during the cloud growth process, the box model calculations without the condensation process, without the collision process and with all processes are performed. Henceforth, these calculations are referred to as without condensation, without collision, and all, experiments.

As discussed in the previous section and S10, arrows (II) and (IV) appearing in rectangle (1) of Fig. 3.5a represent the evaporation process at the cloud top and condensation growth in the cloud layer, respectively, while arrow (III) in rectangle (2) of Fig. 3.5i represents the conversion from cloud to rain by the collision/coagulation process. However, this finding/interpretation requires validation.

To confirm this, the SDFs of the clouds over rectangles (1) and (2) in Figs. 3.5a and 3.5i are investigated. Figure 3.7 represents the averaged mass density distributions (SDFs) over the rectangles (1) and (2), and the SDFs obtained by the box model calculations at $t = 10$ min. From Fig. 3.7, it is concluded that the SDF of clouds over rectangle (1) is a mono-modal shape with a mode value of $\sim 20 \mu\text{m}$ that grows with time when all growth processes are active (the dotted curve in Fig. 3.7a).

The peak value increases without the collision process, as indicated by the dotted-dashed curve. However, it does not increase without the condensation process, as shown by the dashed curve. This indicates that cloud droplets located in rectangle (1) grow mainly by condensation, and they shrink through the evaporation process with an unsaturated air mass; the arrows in rectangle (1) of Fig. 3.5a show the active condensation and evaporation processes.

The SDF averaged over rectangle (2) of Fig. 3.5i is of bi-modal shape as shown in Fig. 3.7b. The first and second mode has peaks around $20 \mu\text{m}$ and $100 \mu\text{m}$, respectively (henceforth, referred to as the small particle mode and the large particle mode). The large particle mode grows from $100 \mu\text{m}$ to about $130 \mu\text{m}$ due to the conversion of water from cloud/drizzle particles to raindrops, as calculated by the box model with all processes included (the dotted curve in Fig. 3.7b).

In contrast, the large mode does not grow without the collision process, as demonstrated by the

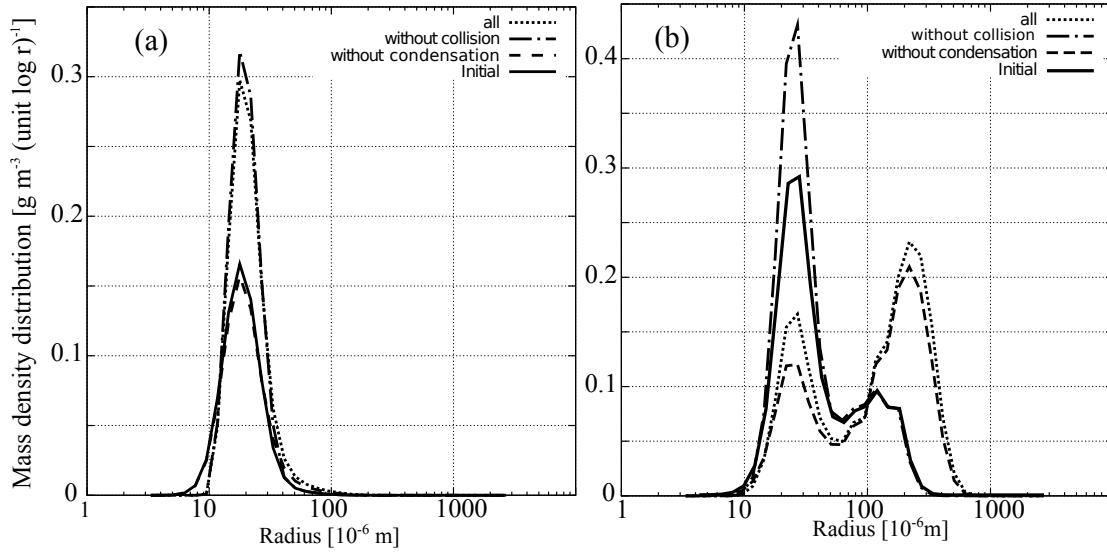


Figure 3.7 Mass density size distribution functions (SDF) averaged over (a) rectangle 1 of Fig. 3.5a, and (b) rectangle 2 of Fig. 3.5i, and SDFs calculated by a box model after 10 min. Solid lines indicate the initial SDFs for the box model calculation. Dotted, dashed, and dot-dashed lines show SDFs obtained at 10 min after start of calculation by the box model with all processes, without condensation process, and without collision process, respectively.

dot-dash curve in Fig. 3.7b. This result suggests that cloud droplets located in rectangle (2) grow mainly by the collision process; the arrow in rectangle (2) represents conversion from cloud to drizzle or rain by the collision process.

3.5. Time evolution of CFODD

The analysis in section 3.4 has been conducted using snapshot results at $t=6$ h after the start of the calculation, and the satellite analyses by S10 using observational data accumulated over several months. For further verification of the interpretation of N10 and S10, an analysis of the temporal evolution of CFODDs is conducted. Although it is difficult to investigate the temporal evolution of CFODDs from satellite observation due to a limitation of samples at a fixed time ($\sim 13:30$ local time), the simulated temporal evolution of CFODDs can be studied using model results.

Figure 3.8 shows the CFODDs obtained from the pristine experiments at $t=2.5$ h and $t=6$ h after the start of each calculation. In the early stages of the calculation ($t = 2.5$ h), high-frequency cloud data mostly locate on the optically thin area for $COD < 22$, and there are few amount of large particles (*i.e.*, $RE > 25 \mu\text{m}$). The COD gradually increases with time (figure not shown). In the later

stages of the calculation ($t = 6$ h) high-frequency cloud data spreads into the area with optically thicker and larger particles.

To compare the cloud growth in the CFODDs with the theoretical growth calculation, the continuous growth model (*e.g.*, Rogers and Yau, 1989) is introduced. This model describes how a collector drop with radius r , whose mass concentration (Liquid water content; LWC) is denoted by LWC (g m^{-3}), grows by falling through and sweeping out the population of smaller cloud droplets. The growth rate of a particle due to this collection process is expressed as follows:

$$\frac{dr}{dt} = \frac{E_{collection} V(r)}{4\rho_w} LWC, \quad (3-9)$$

where $V(r)$ is the terminal velocity of the collector drop and $E_{collection}$ is the collection efficiency. $E_{collection}$ is obtained from a collection kernel (Long, 1974). The upward air velocity is often neglected because it is much smaller than the fall velocity (*e.g.*, Rogers and Yau, 1989), and thus the growth rate with respect to height (h) can be simplified as:

$$\frac{dr}{dh} = \frac{dr}{dt} \frac{dt}{dh} = -\frac{dr}{dt} \frac{1}{V(r)} = -\frac{E_{coll} LWC}{4\rho_w}. \quad (3-10)$$

The negative sign means that r increases as the particle descends. Dividing (3-10) by r , we obtain

$$\frac{dr}{r} = -\frac{E_{coll} LWC}{4\rho_w} \frac{dh}{r}. \quad (3-11)$$

If we relate the fractional change in r to that in Z_e we have

$$\frac{dZ_e}{Z_e} = \alpha \frac{dr}{r} \quad \text{or} \quad d(\ln Z_e) = \alpha d(\ln r), \quad (3-12)$$

and the relationship between cloud liquid water path and optical depth change can be written as

$$d\tau_d = -\frac{3}{2} \frac{1}{\rho_w} \frac{LWC}{r} dh. \quad (3-13)$$

Inserting eq. (3-13) into eq. (3-11) will lead to

$$\frac{dZ_e}{Z_e} = \frac{\alpha}{6} E_{coll} d\tau_d, \quad (3-14)$$

where α differs according to the cloud stage that depends on the dominant water conversion process. A typical value of $\alpha = 6$ is taken when the number concentration is conserved, whereas $\alpha = 3$ when the mass concentration is conserved. It may be natural to assume $\alpha \sim 3$ for the collection process here based on a previous study (Suzuki et al., 2010a). To derive the temporal evolution of radar reflectivity, eq. (3-9) can be reformulated as

$$\frac{dr}{d(\ln r)} \frac{d(\ln r)}{dt} = r \frac{d(\ln r)}{dt} = \frac{E_{coll} V(r)}{4\rho_w} LWC. \quad (3-15)$$

Thus eqs. (3-12) and (3-15) can be simplified as a new equation for the temporal evolution of the radar reflectivity as

$$\frac{d(\ln Z_e)}{dt} = \frac{\alpha E_c V(r) LWC}{4\rho_w r}. \quad (3-16)$$

Combining eqs. (3-14) and (3-16) will give an equation for the temporal evolution of the optical depth

$$\frac{d\tau_d}{dt} = \frac{3V(r)LWC}{2\rho_w r}. \quad (3-17)$$

Solving eqs. (3-9), (3-16), and (3-17), we can calculate the growth trajectory of a collector drop in the CFODD, assuming a typical value of $LWC = 0.2 \text{ g m}^{-3}$ in the pristine experiment. The lines in Fig. 3.8 represent examples of trajectories during a 3.5 h period from the states indicated by cross symbols. The starting points shown as cross symbol in Fig. 3.8 are at the optically deepest points of

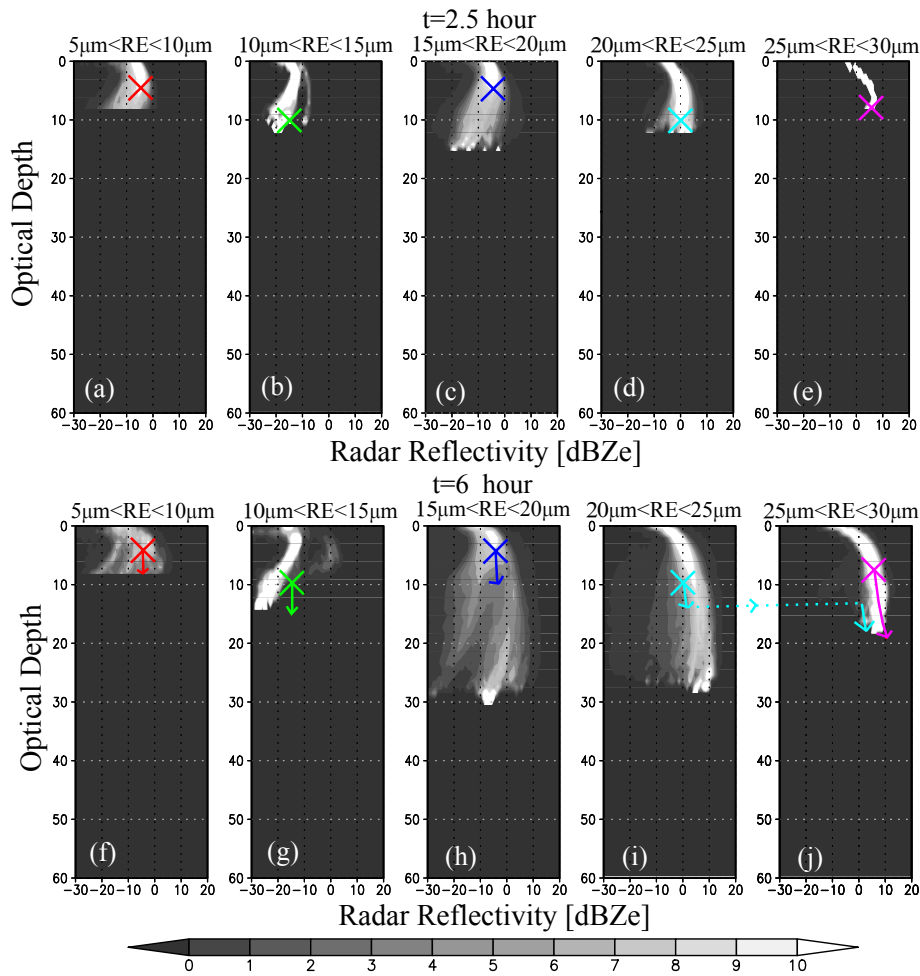


Figure 3.8 Same as Fig. 3.5f-j but at (a–e) $t = 2.5$ h, and (f–j) $t = 6$ h. Lines on a Contoured Frequency Optical Depth Diagram (CFODD) are orbit of clouds calculated during a 3.5 h period by continuous growth model with starting point at (red) $\tau_d = 8$, $Z_e = -10$ (dBZe) in (a), (green) $\tau_d = 10$, $Z_e = -5$ (dBZe) in (b), (blue) $\tau_d = 5$, $Z_e = -5$ (dBZe) in (c), (light blue) $\tau_d = 10$, $Z_e = 0$ (dBZe) in (d), and (orange) $\tau_d = 8$, $Z_e = 5$ (dBZe) in (e) marked by a cross.

shaded value = 10 in Figs. 3.8a–e (listed in Table 3.1). These growth trajectories indicate how cloud droplets at each layer on the CFODD move during the 3.5 h period.

Trajectories of mid- and large-sized particles, *i.e.*, $RE = 15 \mu\text{m}$ and $20 \mu\text{m}$ at the start time of the continuous growth model, move along the ridge of the CFODD high frequency areas, indicating that the water collection process is dominant.

Table 3.1. Initial values of radar reflectivity, COD, and RE used in Fig. 3.8, calculated by the continuous collection model.

Category	Fig. 3.8a	Fig. 3.8b	Fig. 3.8c	Fig. 3.8d	Fig. 3.8e
Initial reflectivity [dBZe]	-10	-5	-5	0	5
Initial τ_d	8	10	5	10	8
Initial RE [μm]	5	10	15	20	25

Trajectories of coarse particles, *i.e.*, RE = 25 μm at the model start time, deflect from the dense high-frequency areas of the CFODD, indicating that cloud droplets grow into coarse droplets and are lost from the cloud layer as precipitation at a later time in the simulation. This interpretation is supported by the surface precipitation as shown in Figs. 3.3 and 3.4 in the pristine experiment.

Trajectories of fine particles, *i.e.*, RE < 10 μm at the model start time, move along an isoline of radar reflectivity, indicating that the growth of these particles is not significant enough to increase the radar reflectivity by the collision process. This fact demonstrates why the collection process is not dominant for these small particles, as discussed in section 3.4. It is easily understood from eqs. (3-16) and (3-17) that these trajectories are mainly generated by the strong size dependence of terminal velocity $V(r)$, as also represented in Fig. 3.9.

This analysis proves that CFODDs can depict a cloud droplet growth regime that drastically changes at a particle radius of around 20 μm between large and small particle regimes with and without significant particle growth by the collision/coagulation process. This critical particle radius is useful for classifying CFODDs. The CFODD for the polluted experiment is characterized by a mean cloud droplet effective radius of 12.1 μm at $t = 2.5$ h, whereas the CFODD for the pristine

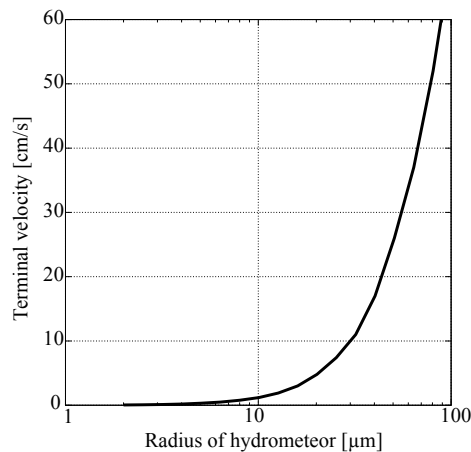


Figure 3.9 Terminal velocity of cloud particles

experiment gives a mean effective radius of 17.8 μm at $t = 2.5$ h.

3.6 Discussion

In the previous sections, the interpretation of the previous studies is verified through the analyses of model results. Although the analyses are meaningful, there are several issues to consider. The issues are 1: validity of vertical axis of CFODDs and 2: effects of vertical grid resolution of cloud model. These points are discussed in this section.

3.6.1. Benefit to take COD for vertical axis of CFODD

Firstly, the vertical axis of CFODD; COD is considered, since transfer from geometrical depth of clouds to COD can make errors. To show the benefit of taking COD to vertical axis, contoured frequency diagrams between cloud geometrical depth (henceforth, referred to as CFGDD), instead of COD, and radar reflectivity are created.

The CFGDD obtained from the pristine experiment is shown in Fig. 3.10. It is seen that condensation mode, collision mode, and entrainment mode are also reproduced in CFGDD, but condensation mode and collision mode are separated into two parts (see Figs. 3.10b and 3.10d).

The first part locates the geometrically deep area, and the other locates the geometrically thinner area. The first and the other part are originated from geometrically thick and thin clouds, respectively (figure not shown). The separation of the modes is not shown in CFODD, because CFODD takes the COD for the vertical axis. This is the one of the benefits of taking the COD for the vertical axis of CFODD in discussing the growth process of clouds.

Although the vertical axis of CFODD has its benefits, one important issue from this analysis should be noted. The issue is the relationship between geometrical thickness of clouds simulated by model and sampling volume of CloudSat/CPR. It is seen from Fig. 3.10 that cloud geometrical thickness simulated by the model is from 400m to 800m.

This geometrical thickness corresponds to 1 or 2 sampling volumes of CloudSat/CPR, and CFODD obtained from satellite observation does not always shown the characteristics of warm cloud simulated in this study. This is the one of the shortcomings of this study. A global simulation of a cloud resolving model needs to be conducted in order to discuss the characteristics of CFODD in more detail. In addition, the vertical resolution of the model is much finer than the satellite sampling volume. The effects of vertical resolution will be considered in the following section.

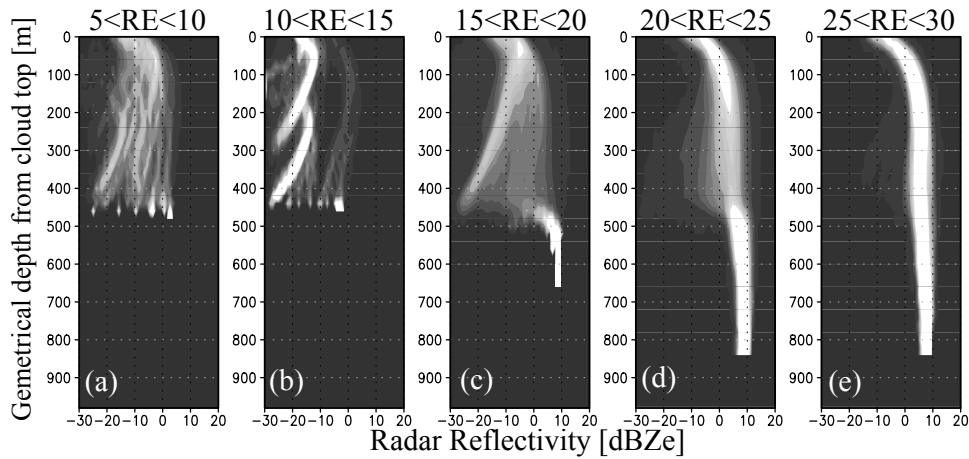


Figure 3.10 Contoured frequency diagram of cloud geometrical depth (CFGDD) at $t = 6$ h obtained from (a–e) polluted, (f–j) pristine experiments, divided by RE of (a) 5–10 μm , (b) 10–15 μm , (c) 15–20 μm , (d) 20–25 μm , and (e) 25–30 μm .

3.6.2. Effects of vertical resolution of model

The vertical resolution of the model ($dz=10\text{m}$ for calculation of radiative transfer) is much higher than the satellite sampling volume of CPR ($dz=480\text{m}$).

To investigate the effects of vertical grid resolution, calculations of the radar simulator changing vertical grid resolution are carried out, creating CFODDs by using radar reflectivity calculated by each grid resolution. The vertical grid resolutions of the calculation are 10m, 60m, and 100m. The parts of CFODDs calculated by this sensitivity calculation are shown in Fig. 3.11. It is seen from this figure that the condensation pattern and the entrainment pattern are separated in the CFODDs calculated by coarse vertical grid resolution (*i.e.* $dz=100\text{m}$).

The difference results from the depth of each grid of volumes. Coarse grid spacing makes a large difference in the COD of each grid from that of its neighboring grid, which can separate the modes in CFODD. This characteristic is also seen in CFODD of satellite observations (Fig. 3.1a), whose vertical grid resolution is coarse (*i.e.* 480m).

Although, vertical grid resolution affects CFODDs, the condensation, entrainment, and collision patterns are reproduced by the model regardless of vertical grid resolution. From these results it can be concluded that CFODDs obtained from model simulations at much finer grid spacing than satellite observations are useful in interpreting the cloud growth process.

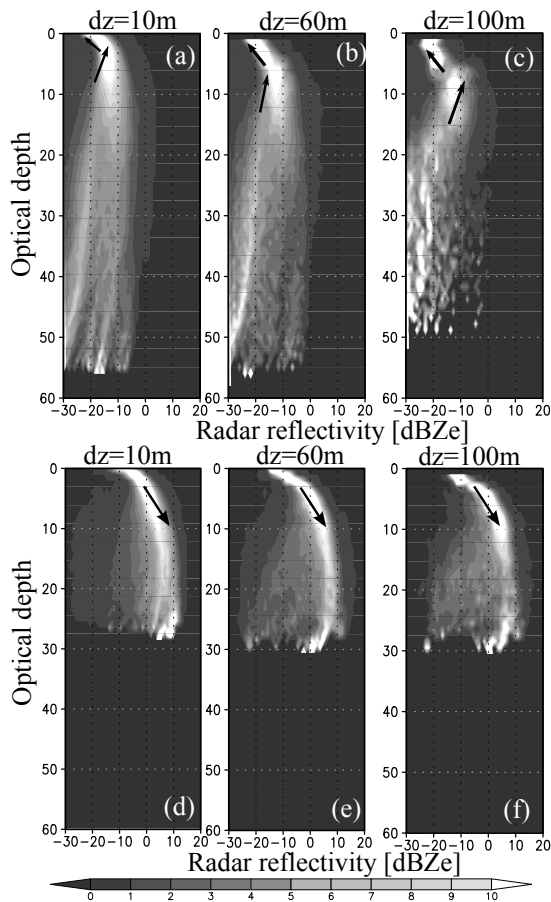


Figure 3.11 Contoured frequency diagram of cloud optical depth (CFODD) at $t = 6$ h obtained from (a–e) polluted, (f–j) pristine experiments, divided by RE of (a) 5–10 μm , (b) 10–15 μm , (c) 15–20 μm , (d) 20–25 μm , and (e) 25–30 μm .

3.7. Conclusions

In this chapter, the CFODDs are calculated, for the first time ever, from the results of a cloud ensemble simulation by a 3D numerical model, which assume a dynamical condition off the Californian coast during the summer season. The simulated CFODDs reproduce the characteristic patterns obtained by satellite observations.

The results and additional diagnostic tests by a box microphysics model show that the clouds in rectangle (1) of Fig. 3.4a mainly grow through the condensation/evaporation process, while the clouds in rectangle (2) of Fig. 3.4i grow as a result of the collision/coagulation process. This result mostly supports the interpretation of previous studies on the dominant growth processes in warm cloud cells (Nakajima et al., 2010b; Suzuki et al., 2010c).

The temporal evolutions of CFODDs are firstly calculated by using the results obtained from the model.

There are some differences between the CFODDs in this study and those of N10 and S10 (*i.e.*, Fig. 3.1). There are dense contours in an optically deep area in the CFODDs of N10 and S10, and these differences appear to result from the shortcomings of the experimental setup. Therefore, it is necessary to conduct a global scale experiment in future.

Chapter 4. Effects of grid resolution on cloud microphysical properties

4.1. Introduction

In Chapter 3, we presented the simulated warm clouds by the spectral bin model (SBM), especially with a fine grid resolution (*i.e.*, $dx=50\text{m}$, $dz=20\text{m}$), which is almost the same as that of the inter-comparison study of LES modeling targeted on DYCOMS-II RF02 (Ackermann et al., 2009). However, as we will describe in Appendix A4, computational costs of SBM are too high to conduct any numerical simulations with such the fine grid resolution over a large area. And therefore, we need to investigate the effects of horizontal grid resolution on simulated clouds and RE-COT patterns, the target of this study. In this section, we will conduct sensitivity experiments, by changing horizontal grid resolution.

4.2. Experimental setup

The experimental setup is the same as the experiment in Chapter 3, except for horizontal grid spacing and cloud-top heights. The horizontal grid spacing is changed in order of 50m, 100m, 300m, and 500m, that is, there are $600 \times 600 \times 75$ grids, $300 \times 300 \times 75$ grids, $100 \times 100 \times 75$ grids, and $60 \times 60 \times 75$ grids, respectively, in a domain of $30 \times 30 \times 1.5$ km with a horizontally periodic lateral boundary condition. Experiments with lower boundary layer (PBL) height ($=595\text{m}$, which is 200m lower than that of experiments in Chapter 3) are also conducted (henceforth we refer to this experiment as “low-CTH” experiment). Calculations are performed for 6 hours with a time step of $dt = 0.5$ s. We analyze the temporal evolution of averaged parameters over the entire domain and vertical profile of several valuables averaged during the last 1 hour to avoid the error of model spin-up.

4.3. Results

Figure 4.1 illustrates the spatial distribution of cloud albedo (A_{lb}) obtained from the sensitivity experiment by changing grid resolution under the polluted aerosol condition. Figure 4.1 also presents the spatial distribution of vertical wind velocity field below the cloud layer (200 m above the ground) and the RE-COT patterns at 6 hours after the start of the calculation.

According to the figure, as the grid resolution becomes finer, the contrast of upward and downward winds is much clearer, and the spatial distribution of albedo shows more detailed structures.

The RE-COT patterns are also affected by grid resolution, and both RE and COT are smaller as

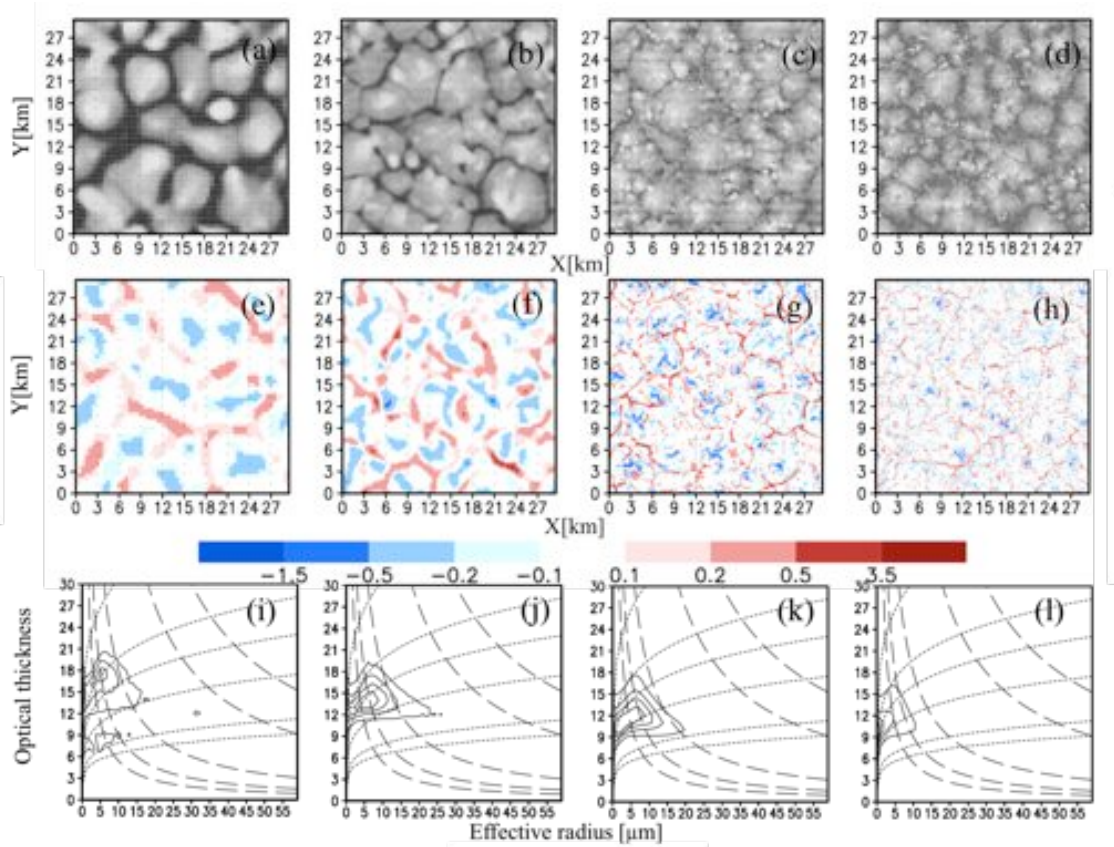


Figure 4.1. Spatial distributions of (a-d) albedo, (e-h) vertical wind [m s^{-1}] field below at $z=200\text{m}$, and (i-l) correlation pattern between r_{eff} and τ_c (RE-COT pattern) at 6 hours after start of calculation obtained from the results of the polluted experiments with at (a,e,i) 500m, (b,f,j) 300m, (c,g,k) 100m, and (d,h,l) 50m grid spacing, respectively.

the grid resolution is finer. To investigate these differences, we check hourly averaged profiles and temporal evolutions of several variables, as follows.

Important factors determining the characteristics of stratocumulus clouds are, large-scale subsidence, turbulent mixing below clouds, radiative cooling at cloud top, and cloud-top entrainment (Duynkerek et al., 1995; Bretherton et al., 2004). Among these variables, the value of large-scale subsidence of this simulation is same regardless of grid resolution, thus we discuss other factors. .

Figure 4.2 shows the domain-averaged vertical profiles of radiative cooling ratio, the sum of grid resolved turbulence kinetic energy (TKE) and sub-grid TKE, liquid water content (LWC), and vapor mixing ratio averaged over the whole calculated domain during the last 1 hour of calculation. Figure 4.3 presents the temporal evolutions of liquid water path (LWP) and cloud-top height, which are good indices of strength of cloud-top entrainment, averaged over the entire calculation domain.

First, we check the amount of water in the cloud layer. To check the amount, vapor mixing ratio and LWC are the good indicators. As shown in Fig. 4.2d, the vapor mixing ratio of the lower cloud

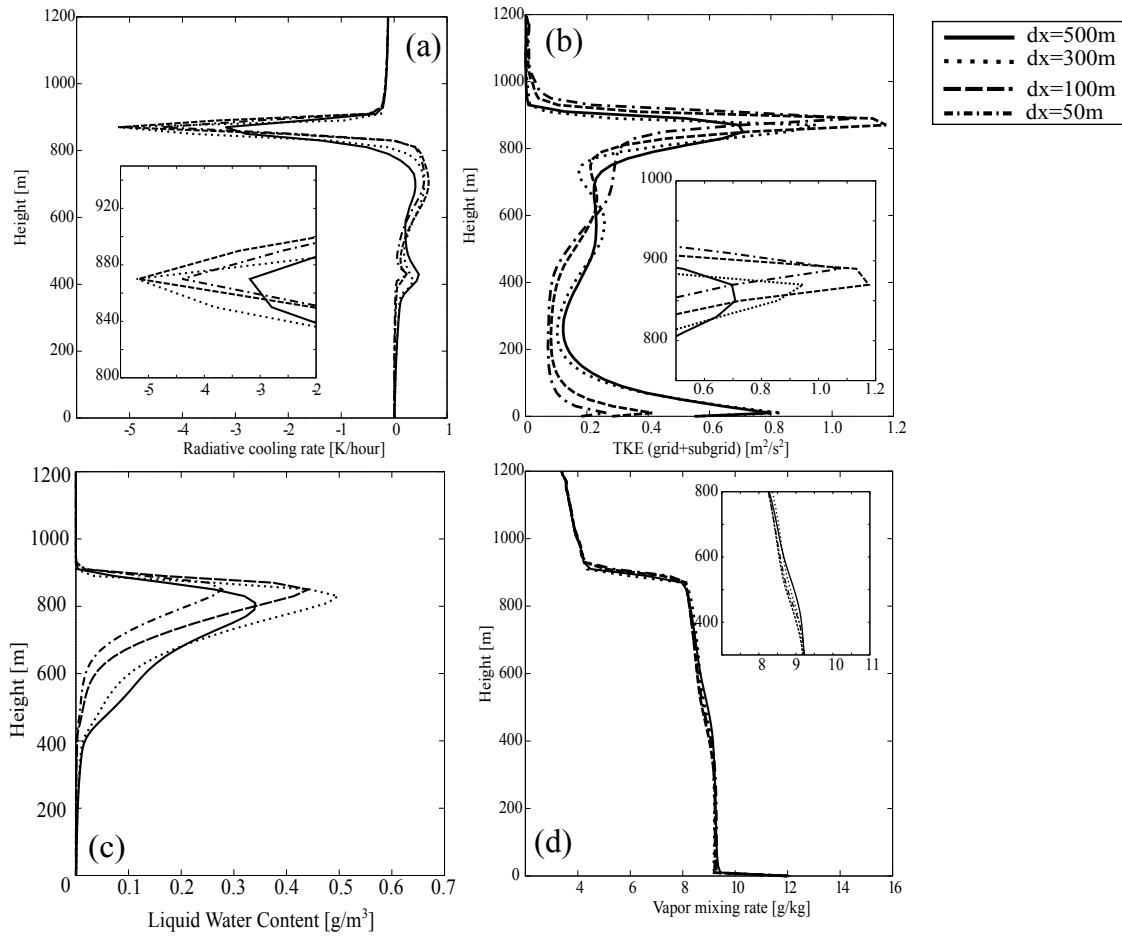


Figure 4.2 Domain averaged profiles of (a) radiative cooling ratio, (b) sum of grid resolved and sub-grid turbulence kinetic energy, (c) liquid water content, and (d) vapor mixing ratio respectively, hourly (*i.e.*, from $t=5h$ to $t=6h$) averaged at (solid line) 500m, (dotted line) 300m, (dashed line) 100m, and (dot-dashed line) 50m grid resolutions. The small graph in (a), (b), and (d) is magnified view of (a), (b) and (d), respectively.

layer (*i.e.*, $z=400m\sim 600m$) simulated by coarse grid resolution is larger than that by fine grid resolution.

It is also found from Fig. 4.2c that LWC simulated by fine grid resolution is small and it increases with decrease in grid resolution except for the LWC at 500m-grid spacing. Although the peak value of LWC simulated by 500m grid spacing is smaller than that simulated by 300m grid spacing, drizzles are generated in experiments at 500m grid spacing, shown as the tail of LWC in lower layer ($z=400\sim 600m$), and a column accumulated LWC (*i.e.* LWP) simulated by 500m grid spacing is larger than that simulated by 300m grid spacing.

These results demonstrate that the amount of liquid water increases with decrease in grid resolution. As a result, both COT and RE simulated by fine grid resolution are smaller than those simulated by coarse grid resolution.

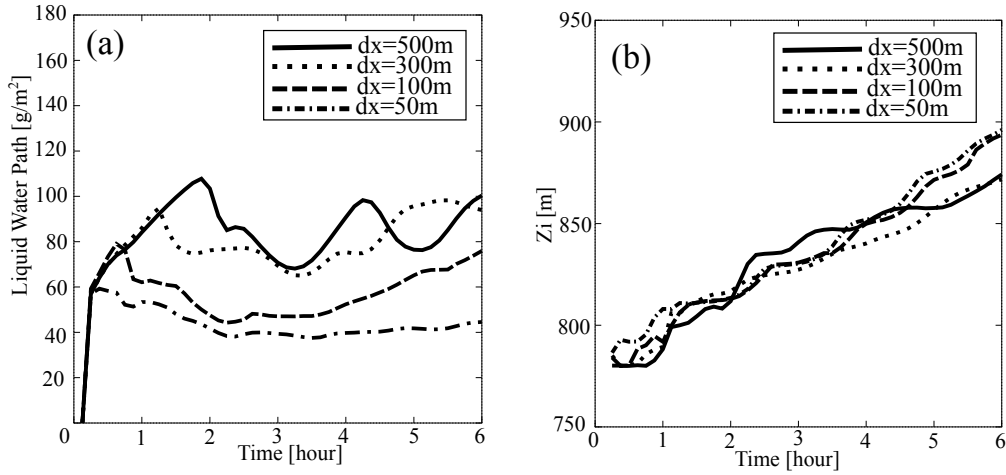


Figure 4.3. Temporal evolutions of (a) simulated liquid water path (LWP) and (b) cloud-top height averaged over entire calculation domain at (solid line) 500m, (dotted line) 300m, (dashed line) 100m, and (dot-dashed line) 50m grid resolutions, respectively.

As well as the difference of liquid water amount, we check the vertical profiles of radiative cooling and TKE, in order to investigate the structure of turbulence and cloud top entrainment.

Fig. 4.2a and Fig. 4.2b show that radiative cooling rate and TKE at the cloud top increase with increase in grid resolution, but their values in the finest grid resolution (*i.e.*, $dx=50m$) are smaller than those in the second finest grid resolution (*i.e.*, $dx=100m$).

To understand this trend, two clues to the solution are shown as follows;. (1) It is found from Fig. 4.3b that the finer the grid resolution is, the higher the cloud-top height is, and evaporation simulated by fine grid resolution is more active than that simulated by coarse grid resolution (figure not shown). Both of these results suggest that the cloud-top entrainment get to be strong with increase in grid resolution. (2) The finer the grid resolution is, the larger the amount of liquid water is as mentioned above, and drizzle amount increases with decreasing grid resolution (Table 4.1), and the drizzle leads to stabilization of cloud layer by evaporative cooling as reported by the previous studies (Stevens et al., 1999; Chlond et al., 2004), and result in weak TKE.

Table 4.1. Drizzling rate [$mm\ day^{-1}$] of each experiments at $t=6$ hour from the start of calculation.

	$dx=50m$	$dx=100m$	$dx=300m$	$dx=500m$
Drizzle rate [$mm\ day^{-1}$]	0.00956	0.0245	0.0831	0.238

The former clue implies that active evaporation simulated by fine grid resolution reduces LWC at cloud layer, which leads to weak radiative cooling. As a result, TKE decrease in fine grid resolution. The latter clue shows that TKE of coarse grid resolution is weak because drizzle stabilizes the cloud layer.

From these results, we can infer that, as far as the last 1 hour (*i.e.*, $t=5\sim 6$), the TKE and radiative cooling simulated by coarse (finest) grid resolution are weak because of the effects of drizzle (the effect of evaporation and weak radiative cooling at cloud top).

However this interpretation shown above is derived only from the profile of the last 1 hour of calculation, and the result does not reach to the equilibrium state, and therefore we need longer time calculation. In addition, the aerosol amount for the initial condition (60 cc^{-1} and 500 cc^{-1}) is different from the observed aerosol amount, and therefore, we do not compare the model results with the in situ aircraft measurement.

We must to conduct some additional experiments to overcome the problems in future.

Although the finest grid resolution ($dx = 50\text{m}$) is better to reproduce detailed structures of warm clouds, we cannot conduct simulation with such fine grid resolution over large area and longer time period (*e.g.*, 6 hours calculation over $125\text{ km} \times 300\text{km}$ domain as shown in next chapter) because of limitation of computational resources, as we mention above and Appendix A4.

Our objective, however, is to provide specific statistics of the RE-COT pattern simulated by coarse grid resolution, and to check if these statistics has the same responses to the external forcing of aerosol, and/or dynamical condition as those simulated by fine grid resolution.

Figure 4.4 shows the RE-COT patterns obtained from the sensitivity experiment by changing aerosol amount and the PBL height at both fine and coarse grid resolution. As demonstrated in Fig. 4.4, the contour lines of RE-COT patterns located more at left-upper area when aerosol amount is small, and at more left area with low PBL height, regardless of grid resolution.

Figure 4.5 illustrates the scattering plots between grid resolutions and RE (COT) averaged over entire calculation domain. The figure indicates that the responses of RE and COT to the changes of aerosol amount and PBL height are similar, even though the differences of RE and COT between pristine and polluted experiments simulated by coarse grid resolution are smaller than those simulated by fine grid resolution.

From these results we can conclude that we can discuss the RE-COT pattern by using the results simulated at a grid resolution of 500 m, even though the resolution is not enough to reproduce detailed structures of warm clouds.

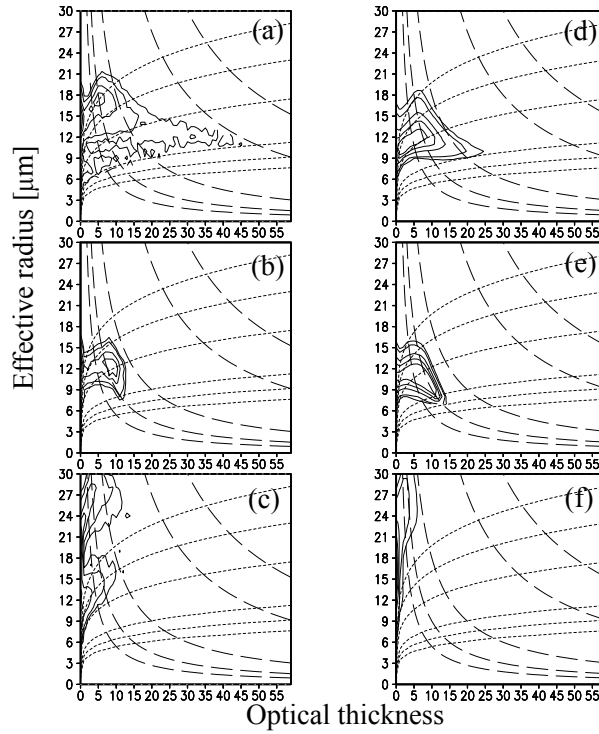


Figure 4.4 Correlation pattern between cloud-droplet effective radius (r_{eff}) and cloud optical thickness (τ_c) obtained from (a,d) polluted experiments, (b,e) low-CTH experiment, and (c,f) pristine experiments at (a,b,c) 500m, and (d,e,f) 100m grid spacing.

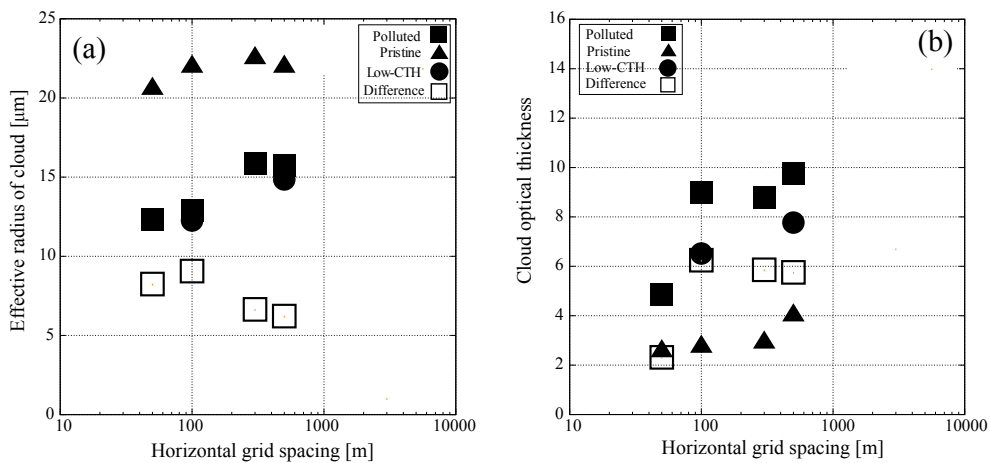


Figure 4.5 Scatter plots between averaged (a) effective radius, (b) optical thickness and grid resolution obtained from polluted (closed square), pristine (triangle), low-CTH experiments (circle), and the difference of each value between pristine and polluted experiments (open square).

4.4. Conclusions

Sensitivity experiments by changing horizontal grid resolution are conducted to investigate effects of grid resolution on microphysical characteristics of warm cloud, under the assumption of typical condition of nocturnal stratocumulus off the coast of California. The experiments indicate that the wide updraft area simulated by coarse grid resolution can transfer more vapors to the cloud layer, which results in a large amount of liquid water in the cloud layer. Due to this large amount of liquid water, the more drizzle is generated, the coarser the grid resolution is, which results in the large RE and COT simulated by the model of coarse grid resolution.

In spite of the differences of RE and COT between coarse and fine grid resolutions, the responses of the characteristics of RE-COT correlation pattern (*e.g.*, shape and location on RE-COT plane) are similar regardless of grid resolutions. These results lead to a conclusion that we can qualitatively discuss the characteristics of RE-COT pattern by coarse (*i.e.* $dx=500\text{m}$) grid resolution even though the resolution is not enough to reproduce detailed structures of cloud.

Chapter 5. Simulations of warm clouds by one-way nesting

5.1. Introduction

In the previous chapter, we have investigated the effects of grid resolution on cloud microphysical properties. These investigations indicate that the simulation conducted at a grid resolution of 500 m can be used to discuss qualitatively the characteristics of the RE-COT pattern and CFODD.

In this chapter, the 3D downscaling simulations of the SBM covering a wide area as that of satellite observations in NN95 are performed with 500m-grid resolution to reproduce the warm clouds, the RE-COT pattern and CFODD, and to compare the simulated results with the satellite observations.

As we mentioned before, Nakajima et al. (1991) firstly found the correlation pattern between RE and COT from the aircraft measurement during the FIRE field campaign. They indicated that positive (negative) correlation pattern was corresponding to non-drizzling (drizzling) clouds. NN95 extended this analysis to a broader region by using retrievals from AVHRR satellite observation, and also confirmed the finding by Nakajima et al. (1991) as displayed in Fig. 5.1. These positive or negative patterns have been investigated by many observational studies (*e.g.*, Asano et al., 1995;

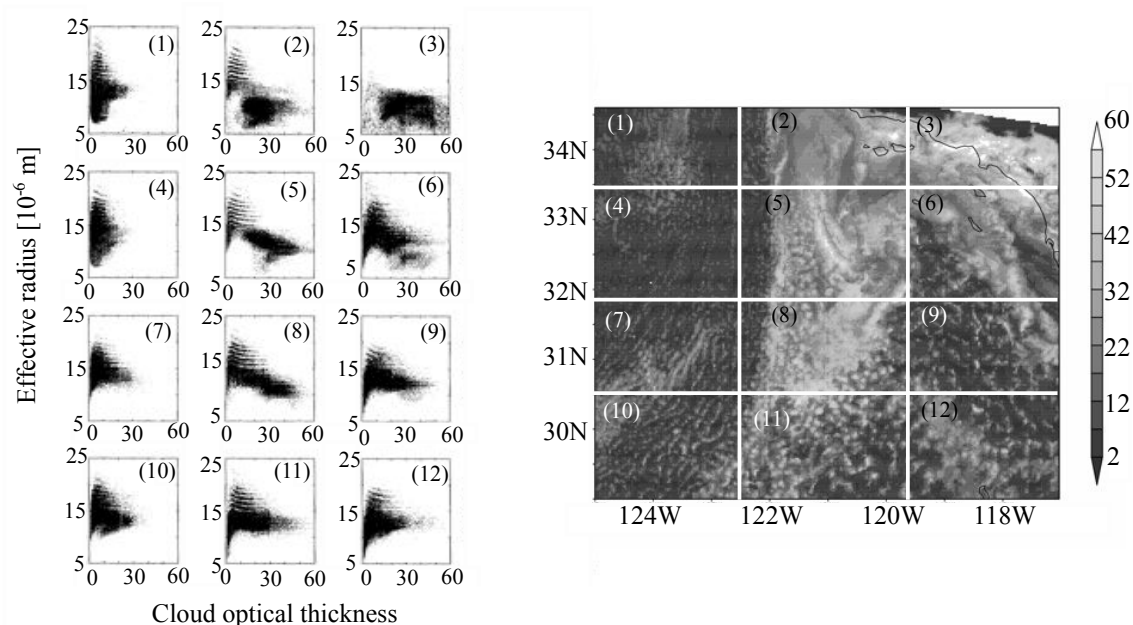


Figure 5.1. Scatter plots of cloud-droplet effective radius vs. cloud optical thickness observed over the FIRE region by NN95 (left; original figures cited from NN95) and geophysical distribution of cloud optical thickness (right). The numbers in parentheses in the left figure indicate the domain number in the right figure, from which scatter plots were obtained.

Han et al., 1998; Bores and Rotstajn, 2001; Kobayashi and Masuda, 2008; Lebsock et al., 2008), where they concluded that these correlation patterns occur in a complicated manner depending on the cloud environments. These observational results suggest that the characteristic patterns in the correlation patterns are governed by complicated but systematic microphysical mechanisms involved in the clouds over different climatic regions of the globe.

Lohmann et al. (2000) also found positive (negative) correlation pattern between RE and COT of warm clouds off the coast of California under non-precipitation (precipitation) conditions simulated by GCM, offering a hint at links between RE-COT correlation statistics and precipitation. The GCM-based study, however, is not suitable for detailed investigation of cloud microphysical structures because the grid resolution of GCM is much coarser ($\sim 2^\circ \times 2.5^\circ$) than the scale of typical individual cloud and is also contingent upon highly parameterized representation of cloud microphysical processes.

To avoid the dependence of the results on the parameterization of cloud microphysics, Suzuki et al. (2006; 2010a; 2010b) have employed a SBM cloud model, and explored formation mechanisms to control the COT and RE relation as discussed in Chapter 1. These model studies produced successful simulations of the positive and negative correlation patterns of the RE-COT relation for non-drizzling and drizzling clouds, respectively, and which are consistent with the previous observational statistics. They then demonstrated that the static stability and aerosol amount systematically modified the RE-COT patterns through changes in the liquid water path (W) and the cloud droplet number concentration (N_c), respectively (Suzuki et al. 2010a). The shape of the aerosol size distribution function was also found to systematically control the RE-COT pattern (Suzuki et al. 2010b). Their simulations with different aerosol size spectrum slopes showed striking differences in the shapes of the RE-COT correlation patterns that closely resembled those retrieved over the FIRE and the Atlantic Stratocumulus Transition Experiment (ASTEX) (Albrecht et al., 1995) in the regions as reported by NN95.

CFODD was, originally used by N10 and S10 and they suggested that CFODD could represent the cloud growth stages. The CFODDs in both studies, however, were obtained by accumulating 3-month results of global scale observations, and could not provide a temporal evolution of CFODD. The temporal evolutions of CFODD have been simulated by a model simulation under idealized dynamical condition in Chapter 3, which was also discussed in Sato et al. (2012b).

In spite of these novel contributions, the interpretation by Suzuki et al. (2010a, 2010b) about RE-COT pattern and that described in Chapter 3 (Sato et al., 2012b) about CFODD were made from their idealized simulations. Thus more realistic simulations are required to investigate how their

findings are valid and useful for understanding the behavior of clouds formed in the real atmosphere.

In addition, we must consider the drawbacks and advantages of the both RE-COT pattern and CFODD in discussing cloud growth processes from these diagrams.

RE-COT patterns can be obtained from a broader area than CFODDs, but it does not have vertical information of cloud. CFODDs, on the other hand, have vertical information, but it can be only obtained from narrow area with low frequency.

COT, the variable of horizontal axis of RE-COT patterns, is an integrated value of COD. In the meantime, it is also a variable of vertical axis of CFODD, thus COD of each altitude can provide the vertical structures for RE-COT pattern if both COT and COD can be obtained simultaneously. Thus, the combination of RE-COT and CFODD may expand the possibility of satellite observations about the cloud microphysics.

Although this combination has a possibility, there are no other studies, to our knowledge, to analyze the characteristics of cloud microphysics by combining the CFODD and the RE-COT pattern because of limited satellite observations. In this study, we will conduct such analysis by using the results simulated by a 3D SBM (UT-ACBM).

In this chapter, we will study the warm clouds off the west coast of California by 3D downscaling simulations, to compare model results with satellite observations, and to understand the interpretation of RE-COT pattern and CFODD about cloud growth stages indicated by the previous studies (*e.g.* N10, S10, NN95, Suzuki et al. 2010a) through an integrated analysis of the CFODD and RE-COT pattern.

5.2. Experimental setup and observation data for comparisons

5.2.1. Experimental setup

Downscaling simulations are conducted for three nested domains over a region off the west coast of California (Fig. 5.2) on 10 July 1987 when the FIRE field campaign was conducted. The settings of simulations, such as domain size, resolution, etc., are summarized in Table 5.1 and Fig. 5.2. The largest, intermediate, and smallest domain is referred to as domain I, II and III, respectively. Only the results for domain III are analyzed in this thesis.

For the domain I, data from the Japanese 25-year Reanalysis Project (JRA-25) (Onogi et al., 2007) are used for the initialization and lateral boundary conditions of dynamical variables, such as horizontal wind velocities, potential temperature, mixing ratio of water vapor, and sea surface

temperature (SST). The JRA-25 data have the horizontal grid intervals of 2.5 degrees, with 23 vertical layers, sampled four times per day (*i.e.* every 6 hours). The geographic data are based on the Global 30 Arc Second Elevation Dataset with 1 km resolution (GTOPO30). Initial and lateral boundary dynamical field of domain II (domain III) are nested every 2 hours (1 hour) from domain I (domain II).

The main framework of the meso-scale model is that of UT-ACBM described in Chapter 2. Both WF turbulence scheme and Deadroff (1980) turbulence scheme are used according to resolution of model (shown in Table 5.1).

The SBM is only used for calculation over domain III and the initial and lateral SDF of hydrometeors of the domain III are assumed zero (no cloud), but with super saturated atmosphere where relative humidity is calculated from total water mixing ratio (not vapor mixing ratio) of domain II. Because this method can make super-saturated atmosphere and artificially thick cloud at lateral boundary and initial time of domain III calculation, the method by Lynn et al. (2005a; 2005b), which determines the initial and lateral SDF of hydrometeor by gamma distribution, should be applied to reproduce the real clouds in future.

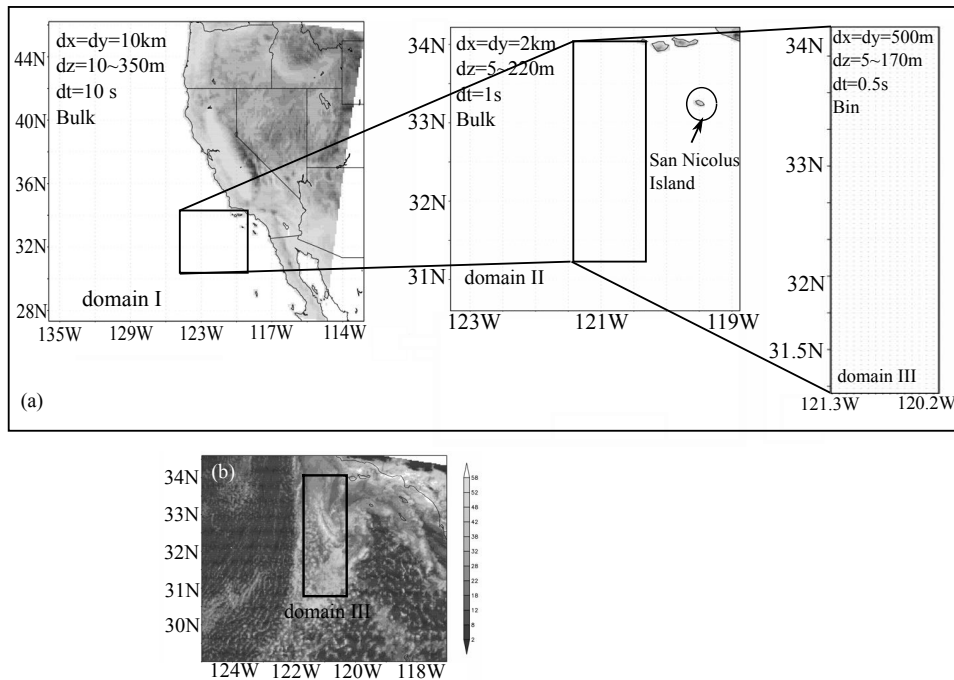


Figure 5.2. (a) Domains for multi-downscale simulations where dx , dy , dz , and dt represent the horizontal and vertical grid resolutions and time step. “Bin” and “Bulk” indicate the microphysical schemes used for the simulations in each domain. (b) Optical thickness observed by satellite over the FIRE region with a black rectangle corresponding to domain III in Fig. 5.2a.

Table 5.1. Catalog of the numerical experiment

	NHM10 ^{*4}	NHM2 ^{*4}	NHM500 ^{*4}
	(domain I)	(domain II)	(domain III)
Dynamics	NHM	NHM	NHM
Microphysics	BULK ^{*1}	BULK ^{*1}	BIN ^{*2}
Aerosol	X ^{*5}	X ^{*5}	SPR ^{*3}
Horizontal grid spacing	10 km	2 km	500 m
Domain size (horizontal)	2020x2020km ²	202x202km ²	125x300km ²
Vertical grid spacing	10~350m	5~220m	5~60m (~40m at cloud layer)
Vertical grid number	60	80	60
Model top height	10160m	9880m	1915m
Turbulence Scheme	WF ^{*6}	WF ^{*6}	DD ^{*6}
Initial and boundary condition	JRA	NHM10 ^{*4}	NHM2 ^{*4}
Calculation time (dt)	168 h (10s)	18 h (1s)	6h (0.5s)
Sampling interval of nesting	6h	3h	1h
Start time	6/26/18UTC	7/8/18UTC	7/10/12UTC

*1: BULK means bulk microphysical model (Yamada, 2003)

*2: BIN means spectral bin microphysical model (Khain et al., 2000; HUCM)

*3: SPR means aerosol field nested from SPRINTARS (Takemura et al., 2005).

*4: NHM10, NHM2, and NHM500 indicate experiments with 10 km, 2 km, and 500 m grid spacing, respectively. NHM means the dynamical framework (Saito et al., 2006)

*5: X means the experiment did not implement the process

*6: WF means turbulence scheme used for weather forecasting, and DD is that of Deadroff (1980)

We conduct additional experiments to check the effects of the initial lateral boundary SDF of hydrometeor in Appendix A1.3, and conclude that the results obtained from the method, in which initial and lateral boundary SDF are assumed zero, can be used to investigate RE-COT patterns, even though the method is not perfect. Based on the additional experiments, we conduct most of experiments in this chapter assuming no clouds at initial and lateral boundary.

Aerosols fields are only calculated over domain III, and the initial and lateral boundaries of aerosol field are given by a global simulation from the Spectral Radiation Transport Model for Aerosol Species (SPRINTARS) (Takemura et al., 2005). The aerosol number concentrations calculated by SPRINTARS is nested directly to the domain III where the number concentrations of five-types aerosols by SPRINTARS are converted into one-type aerosols (sulfate), and unified to a binned SDF using a method considering the different water uptake efficiencies of aerosols as cloud condensation nuclei (CCN) (Iguchi et al., 2008, Choi et al. 2011, personal communication).

The SDF of aerosol particles is discretized into 17 increasing mass bins that cover particle sizes ranging from 1.3 nm to 7.62 μm . Since the range of aerosol radius overlaps the range of cloud SDF, an aerosol particle activated by nucleation process is transformed from the aerosol bin to a cloud bin whose radius is corresponding to the radius of aerosol. The SDF of regenerated aerosols is given as that of the initial aerosol SDF, because parameterization given by eq. (2-5) is not valid for downscaling simulation as we discuss in Appendix A1.

Several sensitivity experiments have been performed in order to understand the RE-COT patterns. The first sensitivity experiment with and without the aerosol regeneration process is performed to emphasize the importance of the process to reproduce realistic cloud fields.

The second sensitivity experiment with changing the aerosol amount is performed to investigate the effects of aerosol amount as studied by Suzuki et al. (2006, 2010a). The initial condition of the SDF for aerosols over domain III is given by eq. (2-4). The horizontal distribution of column accumulated N_{spr} is shown as shaded areas in Fig. 5.3. We then carry out two sensitivity experiments, named as Na3 and Na5 experiments, in which N_{spr} value is three and five times higher than the value in the control run (referred to as Na1 experiment), respectively.

The third sensitivity experiment is related to atmospheric stability. To change the stability of atmosphere, the sea surface temperature (SST) of the domain I is changed. We perform the experiments with $\text{SST} \pm 3\text{K}$ from the SST value of the control run (referred to as CNTL experiment), named as SST-3 and SST+3 experiments, respectively.

This treatment changes the PBL height defined as the lowest layer whose potential temperature is 3 K lower than that in the upper layer. The PBL height is corresponding to cloud-top height.

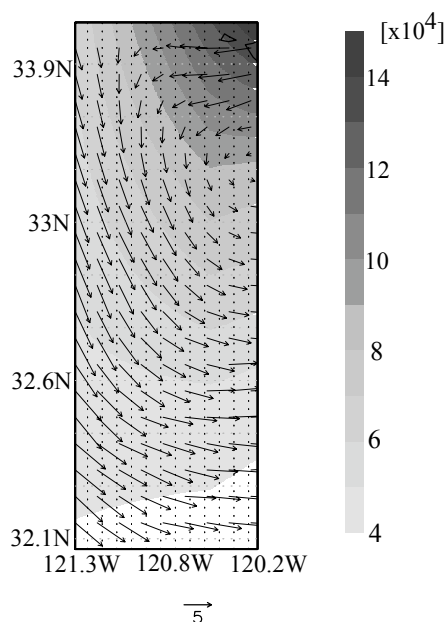


Figure 5.3. Column accumulated number concentration of aerosol (cm^{-2}) (shaded) and horizontal wind velocity (m s^{-1}) at 600 m height (vector) at the initial time of the domain III calculation during the Na3 experiment.

The lower tropospheric static stability at initial condition (LTSS; Klein and Hartmann 1993), defined by the potential temperature difference between the ground and 700 hPa level, is calculated for the SST-3, CNTL, and SST+3 experiments, with extrapolation of the potential temperature to the 700 hPa level. The LTSS values for SST-3, CNTL, and SST+3 experiments are 33.06 K, 29.64 K, and 25.37 K, respectively.

5.2.2. Data for comparisons

Several datasets are used in this study to compare with model results. The first dataset is AVHRR satellite observation (AVHRR LAC) at 15:37UTC on 10 July 1987. The COT, RE, cloud-top temperature (CTT) are retrieved using the CAPCOMS algorithm from the dataset. The second dataset is the CN and CCN number concentrations from aircraft in situ measurements during the FIRE period (Hudson and Xie, 1999). The third dataset is the vertical profiles of temperature and relative humidity observed by radiosonde sounding at Sun Nicolas Island (SNI: 33.4°N, 119.6°W).

5.3. Comparison of model results with observations

Before we discuss RE-COT pattern and CFODD, we must compare model results with observations to demonstrate the model performance and the validity of model results. We firstly compare the amount of aerosols in the model with that obtained from the aircraft in situ measurements in the study of Hudson and Xie (1999), because number concentration of cloud

condensation nuclei (CCN) is a key factor to determine characteristics of warm clouds (Pruppacher and Klett, 1997).

Figure 5.4 represents the profiles of condensation nuclei (CN) and cloud condensation nuclei (CCN), which can be activated into cloud droplet at 0.02 % supersaturation, averaged over the entire domain III at the initial time, and averaged all the data by aircraft measurements during the entire FIRE period (Hudson and Xie, 1999). The figure also shows normalized probability density function (PDF) of visible radiance simulated by the model changing aerosol amount, and that retrieved from AVHRR satellite.

As shown in Figure 5.4, both CN and CCN numbers nested from SPRINTARS are smaller than those obtained from the aircraft measurement. CN and CCN values of Na3 and Na5 at cloud base (~950hPa), where cloud microphysical characteristics are very sensitive to aerosol amount, are close to observational results. In addition, the peak position of PDF simulated by Na5 experiments is closest to that of PDF obtained from satellite observation. Thus, we set the Na5 value to a control value of aerosol amount.

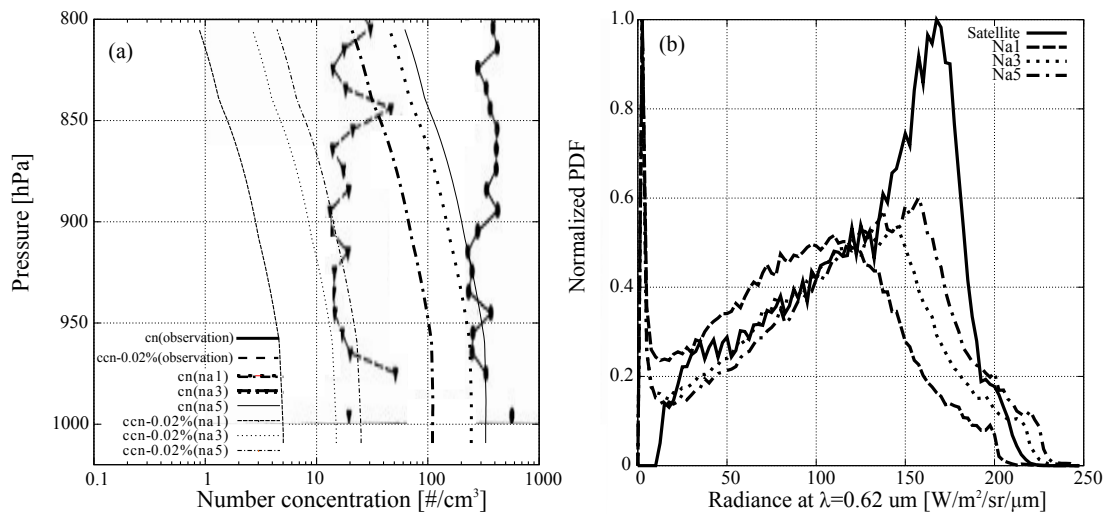


Figure 5.4 (a) Vertical distributions of Condensation Nuclei (CN) averaged from all aircraft measurements during the entire FIRE period (thick dashed line), entire domain III of Na1 (thick dot-dashed line), Na3 (thick dotted line), and Na5 (thin solid line), and Cloud Condensation Nuclei (CCN), which can be activated by 0.02 % super saturation, averaged all aircraft measurements during the entire FIRE period (thick solid line), entire domain III of Na1 (thin dashed line), Na3 (thin dotted line), and Na5 (thin dot-dashed line), (b) Probability density functions (PDFs) of visible radiance (solid line) at $\lambda=0.64 \mu\text{m}$ retrieved from AVHRR satellite, and visible radiance at $\lambda=0.62 \mu\text{m}$ simulated by (dashed line) Na1, (dotted line) Na3, and (dot-dashed line) Na5 experiment respectively.

Secondly, we compare the vertical profiles of temperature and relative humidity obtained from the model with those from radiosonde soundings. Figure 5.5 illustrates the profiles obtained from radiosonde sounding at SNI and over the center of domain III. Although we must compare the profiles obtained from sounding at the center of domain III with those simulated by the model, there is no such sounding station as SNI in the center, and therefore we make comparison of profile observed by radiosonde sounding at SNI and simulated profile at the center of domain III. This comparison is useful as a roughly check of model performance. We, however, will additional experiment targeting on a day when the observations of profile at the center of domain III were performed among domain III, in future.

Figure 5.5 indicates that PBL height of model is a little bit lower than that obtained from sounding. These differences probably arose not only from the difference of geographical location but also from the uncertainty in meteorological fields that are used for initial and lateral boundary conditions of the model. The meteorological fields are derived from JRA-25 data with a relatively coarse resolution of $2.5^\circ \times 2.5^\circ$, while the model resolutions for domains I, II, and III are 10 km, 2 km, and 500 m, respectively, and these resolutions are much finer than resolution of JRA-25. The difference of resolution is seemed to make contradiction of PBL height. Future work is also needed to improve the model performance.

Finally, we compare the model results with satellite observations. Figure 5.6 shows the radiance at $0.64 \mu\text{m}$ wavelength observed by a sensor boarded on AVHRR satellite, and the radiance at $0.62 \mu\text{m}$ wavelength simulated by J-simulator from model results with and without regeneration process.

Although the model does not reproduce cloud field and structure completely, the radiances simulated by the model with the regeneration process are close to satellite observation as shown in

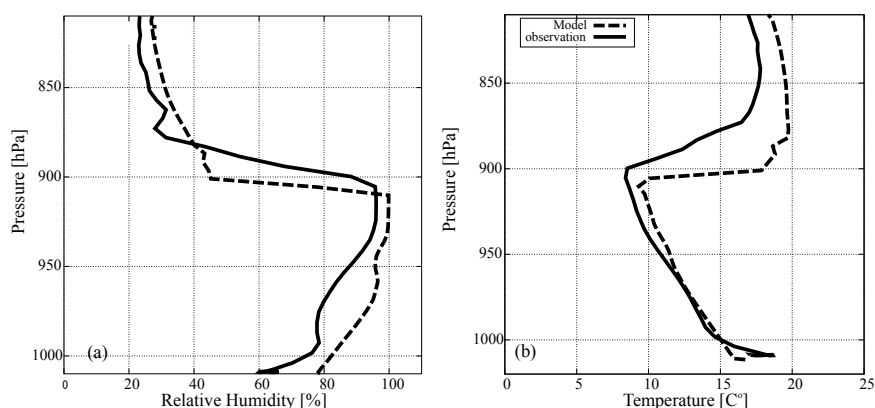


Figure 5.5 Profiles of (a) relative humidity [%] and (b) temperature [°C] observed by radiosonde observation at San Nicolas Island (SNI: 33.4°N , 119.6°W) (solid line), and model at center of domain III (dashed line).

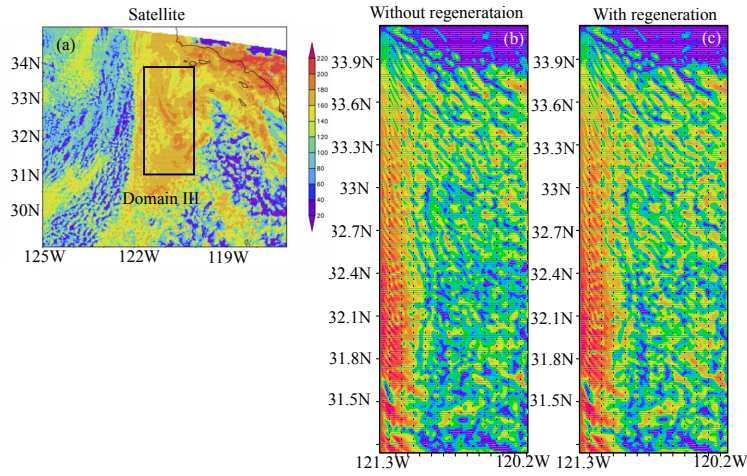


Figure 5.6 Radiance [$\text{Wm}^{-2}\text{Sr}^{-1}\text{m}^{-1}$] (a) detected at $0.64 \mu\text{m}$ wavelength of AVHRR satellite at 15:37UTC on 10 July 1987, calculated by J-simulator from model simulations (b) without regeneration process, (c) with regeneration process.

Fig. 5.7, while the model without the regeneration process underestimates the radiance.

The results can be interpreted as follows: the model without the regeneration process does not have any source to compensate CCN except for their inflow from lateral boundary and above the cloud top. In this situation, once aerosols are activated as CCN, there are no other aerosol sources in the model. As a result, the model loses the potential to make more cloud droplets.

Since the regeneration process supplies more aerosols into the model, more cloud droplets can be generated with the regeneration process. These conditions are illustrated schematically in Fig. 5.8,

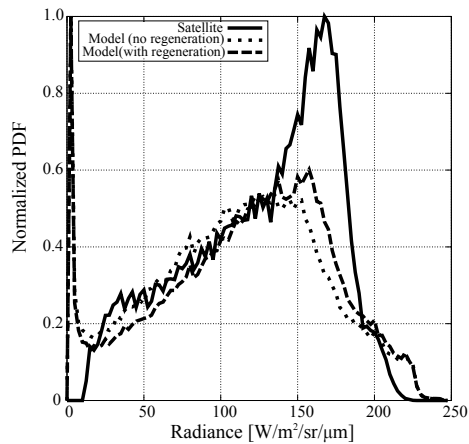


Figure 5.7 Probability density functions (PDFs) of visible radiance. The solid, dashed, and dotted lines represent satellite observations, model simulations with and without regenerations.

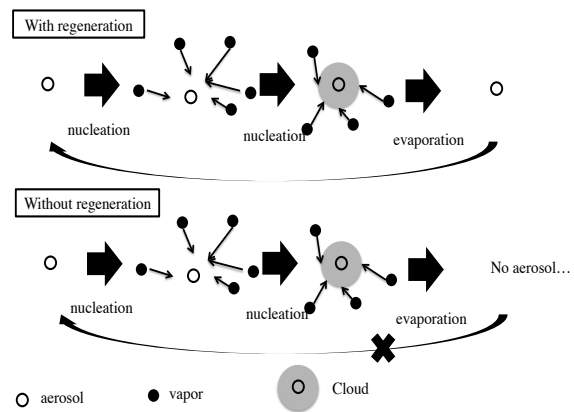


Figure 5.8 Schematic illustrations of the regenerating aerosols processes.

and these results are one of the important findings in this study.

Also with regeneration process, there are other possible sources of aerosols in real atmosphere as will be described in Appendix A2. Therefore it is necessary in a future study to include these aerosol sources in regeneration processes.

Figure 5.9 represents the RE-COT patterns obtained from the model. The patterns with regeneration process scatter around broader area, and represent positive (negative) pattern in northern (center and southern) area shown by black arrows, which is similar to the results obtained from satellite observations (*e.g.* Fig. 5.1-left).

The patterns without regeneration process also reproduce positive and negative correlation pattern, but the contour lines of Fig. 5.9e and 5.9f concentrate on the left-upper area where the optically thin clouds and large particle size are dominant.

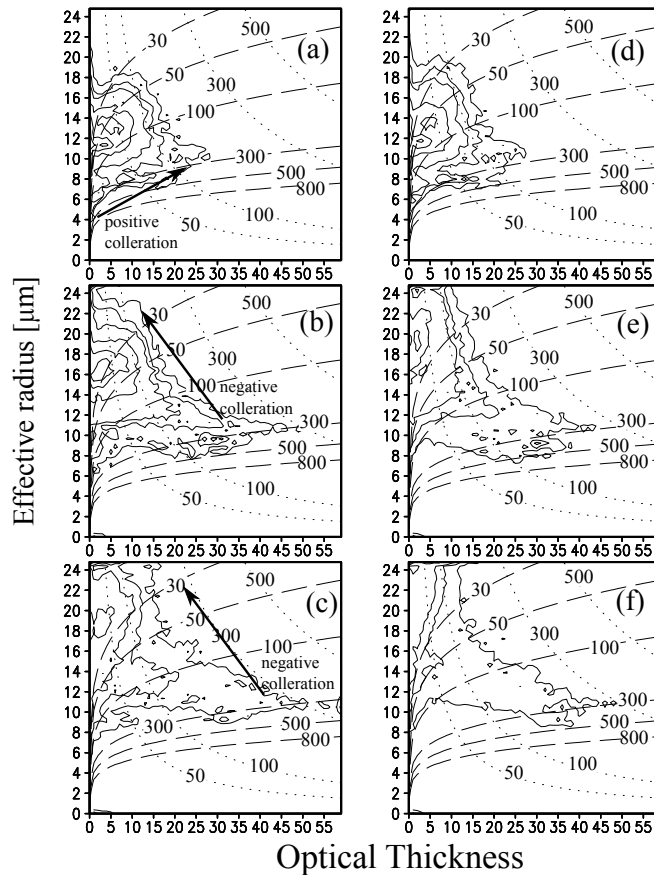


Figure 5.9 Normalized correlation pattern between cloud optical thickness and cloud-droplet effective radius obtained from the simulated results with regeneration (a, b, c), and without regeneration (d, e, f). (a, d), (b, e), and (c, f) are the patterns obtained from the northern, center, and southern parts of domain III divided into three parts in the meridional direction. The contour values are for 0.01, 0.1, 0.3, 0.5, with setting the maximum value of frequency to 1. The arrows in (a) and (b), (c) demonstrate positive and negative correlation.

These results clearly show that the RE-COT patterns simulated with regeneration process are well reproduced those retrieved from satellite.

Furthermore, these results suggest that the model reproduce visible radiance, CCN amount, and RE-COT patterns retrieved from satellite, although it underestimates PBL height.

5.4. Cloud growth process observed by satellite remote sensing

In the previous sections, we have demonstrated that the model can reproduce basic cloud microphysical characteristics of warm clouds and RE-COT patterns retrieved from satellite observations. These results can lead to a more detailed use of the present model to identify the main growth processes that characterize the RE-COT pattern and CFODD.

The patterns obtained from the model with regeneration reproduce positive (negative) correlations over northern (center and southern) area of the domain III similar to the patterns obtained from satellite.

Based on the interpretation of Suzuki et al. (2010a), the trend translating from positive (northern) to negative (southern) correlations corresponds to the translation of cloud growth stage from condensation process to collision process.

However this interpretation is deduced from the 2D simulation of an isolated cloud in the model domain, and the distance from northern to southern part of the domain III is several hundreds of kilometers, which is too far to discuss the growth stage of isolated cloud.

In addition, RE-COT patterns do not include any information of cloud vertical structure. Thus, we will confirm the validity of the interpretation by using the results of 3D-model, where an ensemble of clouds is simulated (*i.e.*, not an isolated cloud) in the model domain.

First, we investigate which cloud growth process is dominant in each area of RE-COT pattern on cloud microphysical box model. We apply a zero-dimensional box model of cloud microphysics (henceforth we refer to the model as just "box model") for the simulated cloud field to identify the dominant processes shown as in Chapter 3.

The initial value of dynamical parameters and initial SDF of hydrometeors for the box model are obtained from the cloud field simulated by the current 3D model. Box model calculations are performed for a total of 10 seconds with a time step of $dt = 0.5$ s.

By taking difference of initial RE (COT) obtained from initial SDF from RE (COT) at $t=10$ s after starting time of box model calculation, we derive moving direction of the point where each cloud locate on RE-COT planes. Therefore we define those clouds with upper right, upper left, and lower left moving directions over RE-COT patterns as cloud droplets evolving through condensation,

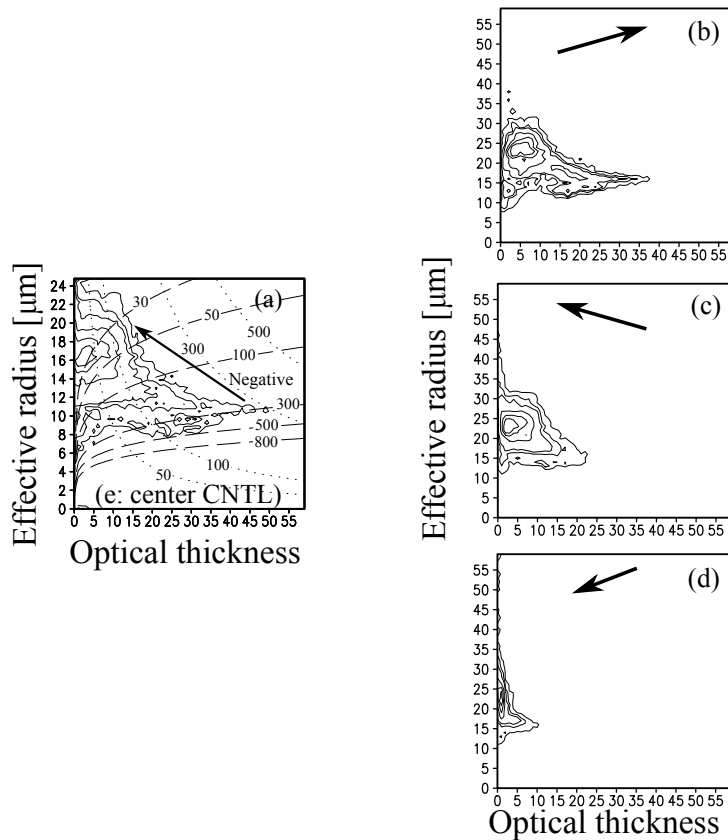


Figure 5.10 (a) Same as Figure 5.9b, and same as but categorized by moving direction on RE-COT plane to (b) upper right, (c) upper left, and (d) lower left direction with time (*i.e.*, accumulating (b), (c), and (d) makes (a)). The moving directions are derived from calculations of the box model. The contour values are for 0.01, 0.1, 0.3, 0.5, and 0.7 with setting the maximum value of frequency to 1.

collision, and evaporation processes, based on the interpretation of Suzuki et al. (2010a).

Figure 5.10 represents a frequency density distribution of RE-COT pattern at the center part of domain III categorized by moving directions of each cloud on RE-COT patterns (*i.e.*, we can get Fig. 5.10a by accumulating Fig. 5.10b, Fig. 5.10b, and Fig. 5.10c). The moving directions are defined by difference of the position on RE-COT plane at the initial time of box model calculation from that at 10 seconds after the box model calculation (*e.g.*, if both COT and RE at 10 seconds after box model calculation is larger than those at initial time of box model calculation, the moving direction is "upper-right").

It is found that contours in Fig. 5.10b and 5.10c distribute in wide area even though the accumulated pattern (*i.e.*, Fig. 5.10a) is negatively correlated. This can draw a conclusion that condensation and collision process can occur simultaneously at a wide area over the RE-COT pattern, no matter RE-COT patterns are negatively correlated. This trend is the same as the other part of domain III (figure not shown).

From this result, it is inferred that positive and negative correlation pattern are not always the indicative of condensation and collision process.

Later on, we will check the vertical structure of clouds by using CFODD because RE-COT pattern, by itself, does not have any information of clouds vertical structures. Figure 5.11 shows RE-COT patterns rotated 90 degree in clockwise (Fig. 5.11a) and CFODD (Fig. 5.11b-f) obtained from the simulated cloud over the center part of domain III with regeneration process.

Even though the RE-COT pattern over the center part of domain III correlate negatively, which is indicative of collision process based on Suzuki et al. (2010a), several patterns are displayed in the CFODD (*i.e.* condensation, evaporation, and collision pattern) demonstrated as black arrows in Fig. 5.11. This trend is the same as the results over the others parts of domain III (*i.e.*, northern and southern part of domain III). This means that all these processes occur simultaneously, even though RE-COT patterns are negatively or positively correlated.

Both of these results do not always support the interpretation of Suzuki et al. (2010a), in which the positive and negative correlations are corresponding to condensation and collision/coagulation process, respectively.

To understand the reason of the contradiction, it is worthy to mention the difference of the

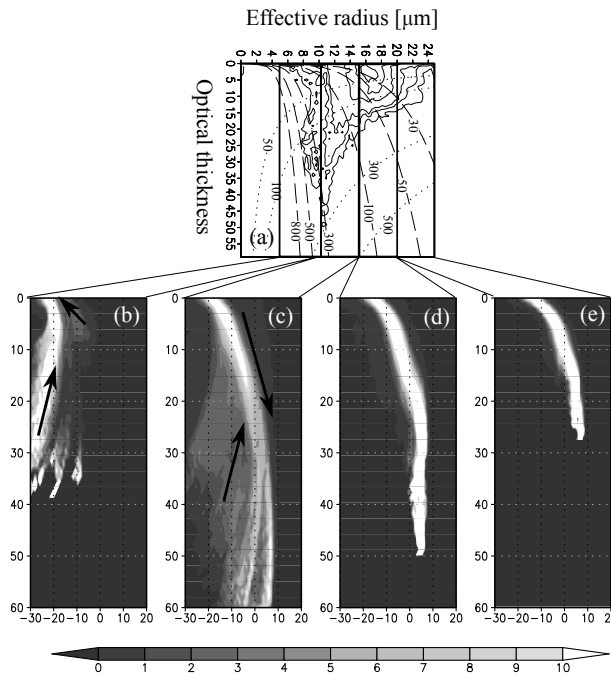


Figure 5.11. (a) The correlation patterns between cloud-droplet effective radius (r_{eff}) and cloud optical thickness (τ_c) (RE-COT pattern) and (b-f) Contoured Frequency Optical Depth Diagram (CFODD) obtained from the simulated results with regeneration process at the center part of domain III

experimental setup between this study and Suzuki et al. (2010a). The main difference is number of clouds simulated in the calculation domain. This study simulates multiple clouds in the calculation domain, while Suzuki et al. (2010a) simulated an isolated cloud in the calculation domain.

To further investigate the effects of this difference of experimental set on the RE-COT patterns, additional analyses targeting on each cloud are required. It is, however, difficult to conduct the analysis of each cloud because there are too many clouds over the calculation domain to analyze one by one. To overcome this difficulty, we use the results of idealized simulation with a grid resolution of 500m, conducted in Chapter 4.

Figure 5.12a represents the trajectory of seven clouds on the RE-COT patterns, calculated from the results of idealized simulation. This figure indicates that RE and COT for each cloud moves along the anti-clockwise triangle (Fig. 5.12b), which is the schematic illustration of Suzuki et al. (2010)'s interpretation, even though the shape of the triangle is different from cloud by cloud.

To investigate vertical structures of each cloud, we generate temporal evolution of CFODD obtained from a cloud, whose trajectory is shown by the blue line in Fig. 5.12a.

It can be seen from Fig. 5.13 that a transition from a condensation pattern to a collision pattern on CFODD corresponds to that from a positive correlation pattern to a negative one on RE-COT.

From these figures, we can conclude that a correlation pattern obtained from satellite does not always represent the cloud growth stage, but shows mixtures of each growth stage of several clouds,

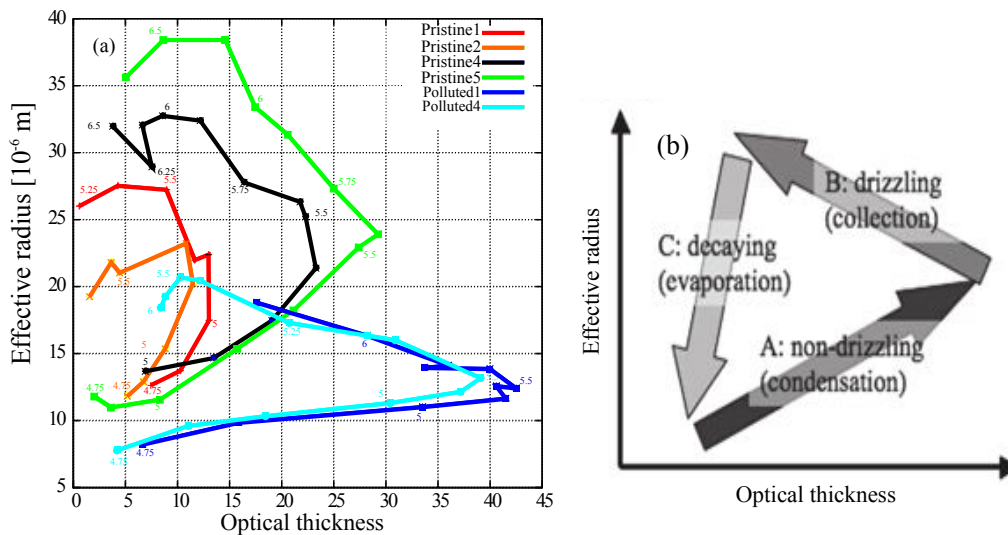


Figure 5.12 (a) Example of trajectories of clouds on the correlation patterns between cloud-droplet effective radius (r_{eff}) and cloud optical thickness (τ_c) (RE-COT patterns) obtained from idealized simulations. The numbers shown along each trajectory represent the time [hour] after starting calculation. (b) Schematic illustration to represent clouds growth stage on RE-COT pattern (Suzuki et al. 2010a).

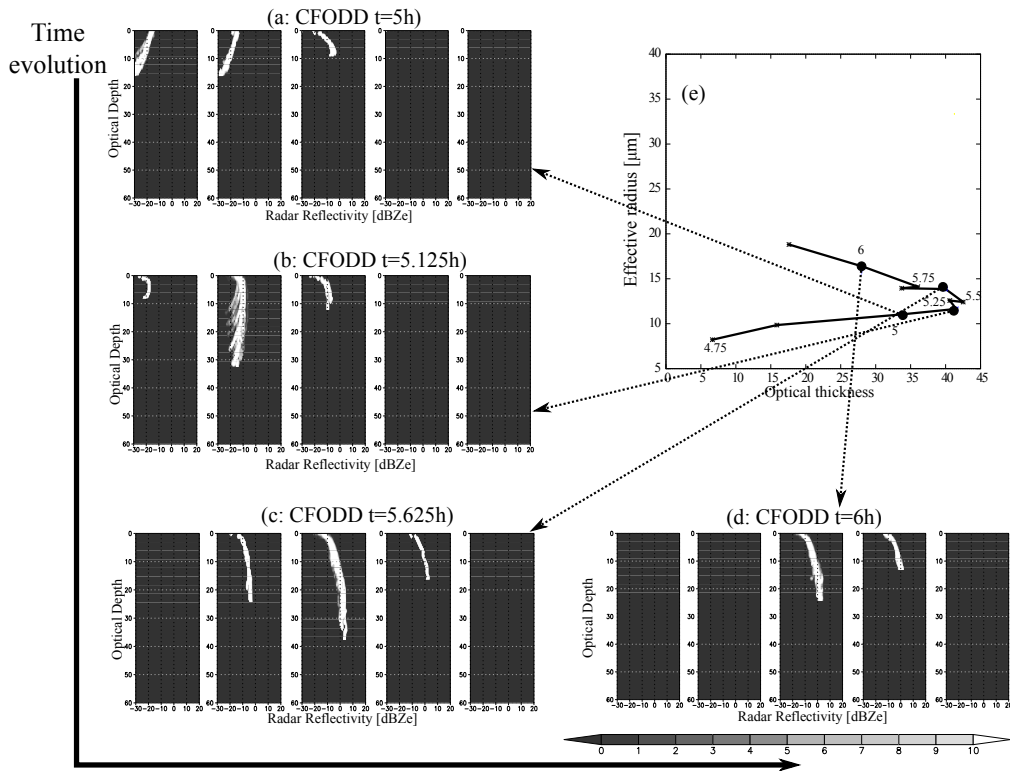


Figure 5.13 An examples of Contoured Frequency Optical Depth Diagram (CFODD) of an clouds, where its trajectory is the blue line of fig. 5.12a, obtained from the idealized model simulations at (a) $t=5$ h, (b) $t=5.125$ h, (c) $t=5.625$ h, and (d) $t=6$ h, and (e) the trajectory of the cloud shown by the blue line of fig. 5.12a.

which appears to be in contradiction to the previous study. However, each cloud moves along an anti-clockwise triangle on a RE-COT pattern during a life cycle of a cloud, which does not contradict to the interpretation by Suzuki et al. (2010a) and NN95.

5.5. Conclusions

In this chapter, downscale simulations of warm clouds in a real atmosphere off the west coast of California are conducted by the 3D spectral bin model. We have successfully reproduced warm clouds in the region, and RE-COT patterns and CFODDs. We have combined the RE-COT patterns and CFODDs to verify the interpretation about cloud growth stage on the RE-COT pattern and CFODD, which was suggested by the previous study (*e.g.* N10, S10, Nakajima and Nakajima 1995, Suzuki et al. 2010a).

Simulated results with the regeneration process of aerosol can reproduce the cloud microphysical properties of warm clouds obtained from the satellite observations. The characteristics of RE-COT pattern and CFODD are well reproduced by the model simulation with regeneration process. From

the combined analyses of a model derived RE-COT patterns and CFODD, and the results obtained from 0-th dimensional box model, it is demonstrated that the statistics of the RE-COT pattern obtained from satellite does not always represent the growth stage of clouds, but represent the mixture of the growth stages of several clouds. This result contradicts the interpretation about RE-COT pattern by the previous studies (NN95; Suzuki et al., 2010a).

The results from the model, however, indicate that RE-COT pattern created by each cloud represents cloud growth processes, which are expressed as an anti-clockwise triangle on RE-COT pattern in Fig. 5.12b. This indicates that the interpretation of the previous studies can be only applied to an isolated cloud, and the RE-COT patterns obtained from satellite represent complex characteristics of a mixture of several clouds.

Although these results shown above discuss the interpretation of NN95 and Suzuki et al. (2010a), these results do not discuss the basic characteristic of the RE-COT pattern *e.g.* key factors, which determine the characteristics of RE-COT patterns and CFODD. We will discuss it in the following chapter.

Chapter 6. Discussion

Results shown in the previous chapter confirm that the RE-COT patterns obtained from satellite data do not always represent the typical growth stages of a single cloud cell as simulated by Suzuki et al. (2010a), however, they represent various growth stages of multiple cloud cells. To find the controlling factors that determine the characteristics of the RE-COT pattern, *i.e.* shape and location of the geometrical center, the confirmation in the previous chapter is not sufficient.

In this section, the key factors are investigated by conducting sensitivity experiments. Suzuki et al. (2010a) and Sato et al. (2012a) investigated the effect of the aerosol amount and the atmospheric stability, which were found to be important factors in their single cell simulations.

Along with these two factors, several other factors are reported by many previous studies as controlling the microphysical properties of warm cloud: these include cloud top entrainment, turbulence of the sub-cloud layer, surface flux, large scale subsidence, longwave flux at cloud top (*e.g.* Bretherton et al., 2004), drizzle rate (*e.g.* van Zanten and Stevens, 2005), relative humidity above the cloud top (*e.g.* Ackermann et al., 2004), strength of shortwave irradiance (solar radiation), atmospheric stability, and so on.

Among these factors, surface flux, large-scale subsidence, turbulence, longwave radiative flux, and atmospheric stability closely relate to PBL height, *i.e.*, the balance of these factors determines PBL height. This indicates that the sensitivity of the RE-COT pattern to PBL height can offer some indication about the effects of other factors determining PBL height. In addition, the effects of each factor in the simulated clouds are considered minor in this study, because PBL height is mainly given by simulated results of domain II. Aerosol amount, on the other hand, does not directly relate to PBL height and atmospheric stability.

Considering this situation, it is very important to investigate the effects of PBL height and aerosol amount to investigate the general characteristics of the RE-COT pattern rather than other factors.

Keeping these factors in mind, sensitivity experiments changing aerosol amount and PBL height are conducted. The results of the sensitivity experiments are described in section 6.1. The factors to determine the shape and geometrical center position of RE-COT pattern are investigated in section 6.2. Some additional interesting characteristics in RE-COT patterns are discussed in section 6.3.

6.1. Sensitivity to aerosol and PBL height

Firstly, the sensitivity of the RE-COT pattern to aerosol amount is investigated. Figure 6.1 represents spatial distributions of the radiance at a wavelength of $0.62 \mu\text{m}$ (hereafter radiance) at 15

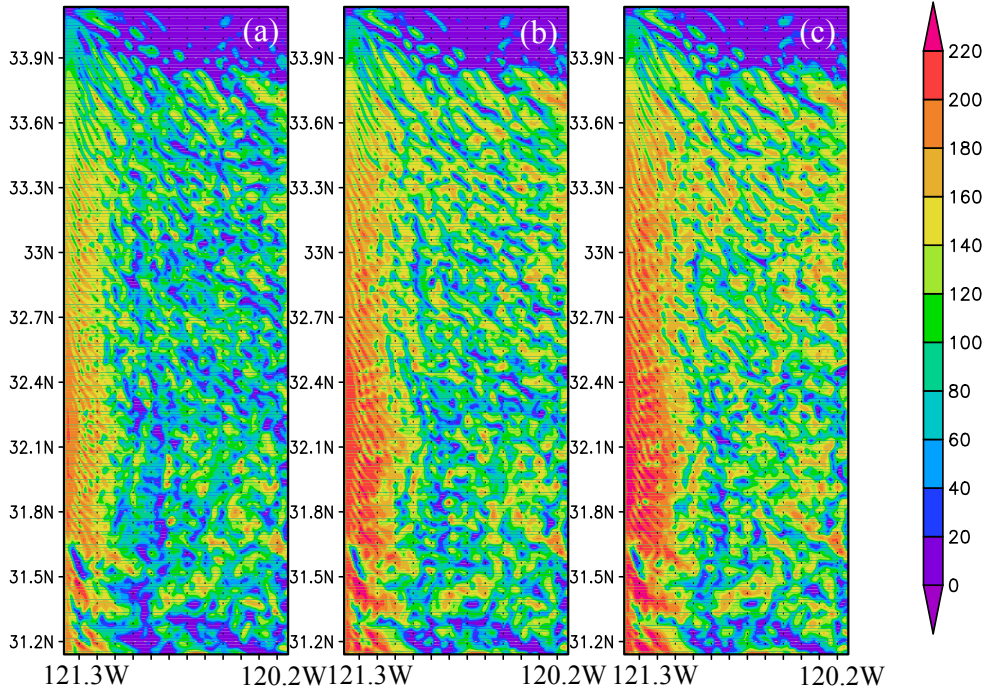


Figure 6.1 (a-c) Simulated radiance [$\text{Wm}^{-2}\text{Sr}^{-1}\text{m}^{-1}$] at $\lambda=0.62 \mu\text{m}$ and (d-f) net radiative flux at TOA calculated by the J-simulator with (a,d) Na1, (b,e) Na3, and (c,f) Na5 experiments, respectively, at 15 UTC on 10 of July 1987.

UTC on July 10, 1987, obtained from the sensitivity experiment by changing aerosol amount. It is found from the figure that the radiance increases monotonically with increasing aerosol amount.

Figure 6.2 shows RE-COT patterns obtained from the aerosol sensitivity experiment. Dashed and dotted lines represent isolines for cloud number concentration (N_c) and liquid water path (W) provided by the adiabatic condensation growth model (Brenquier et al., 2000). The COT derived from the model is given as

$$\tau_c = \begin{cases} \frac{8}{5} (\pi k_a)^2 \frac{\rho_w}{l_a} N_c^2 r_{eff}^5 (H) \dots (N_c = const.) \\ \frac{9}{5} \frac{1}{\rho_w} \frac{W}{r_{eff}} \dots \dots \dots (W = const.) \end{cases} \quad (6-1)$$

where H is the geometrical height from the cloud base and ρ_w is the density of water. The derivation of eq. (6-1) is described in Appendix A9. The parameters k_a and l_a denote is a coefficient relating the volume-mean radius and l_a is the adiabaticity factor. Values for k_a and l_a are set as $k_a^{-1/3}=1.1$ and $l_a=5.2 \times 10^{-3} \text{ g m}^{-4}$, respectively, following Suzuki et al. (2010b).

Although clouds do not always grow as the adiabatic growth model predicts, the model, when applied to the simulated SBM results, provides us with a useful theoretical framework to understand how each particle growth process links to the fundamental cloud properties such as W and N_c . (It is nevertheless worth noting that the adiabatic model still has a limitation, as will be discussed later.)

From Fig. 6.2, it is found that positive and negative correlation patterns, shown by black arrows, are also reproduced in all the experiments except for the Na1 experiment. In the Na1 experiment, optically thinner clouds with drizzle are generating (figure not shown), therefore contours of Figs. 6.2a, 6.2d, and 6.2g are concentrated in the left-upper area.

Comparisons of the outermost contour line, which show max value of W and N_c in each

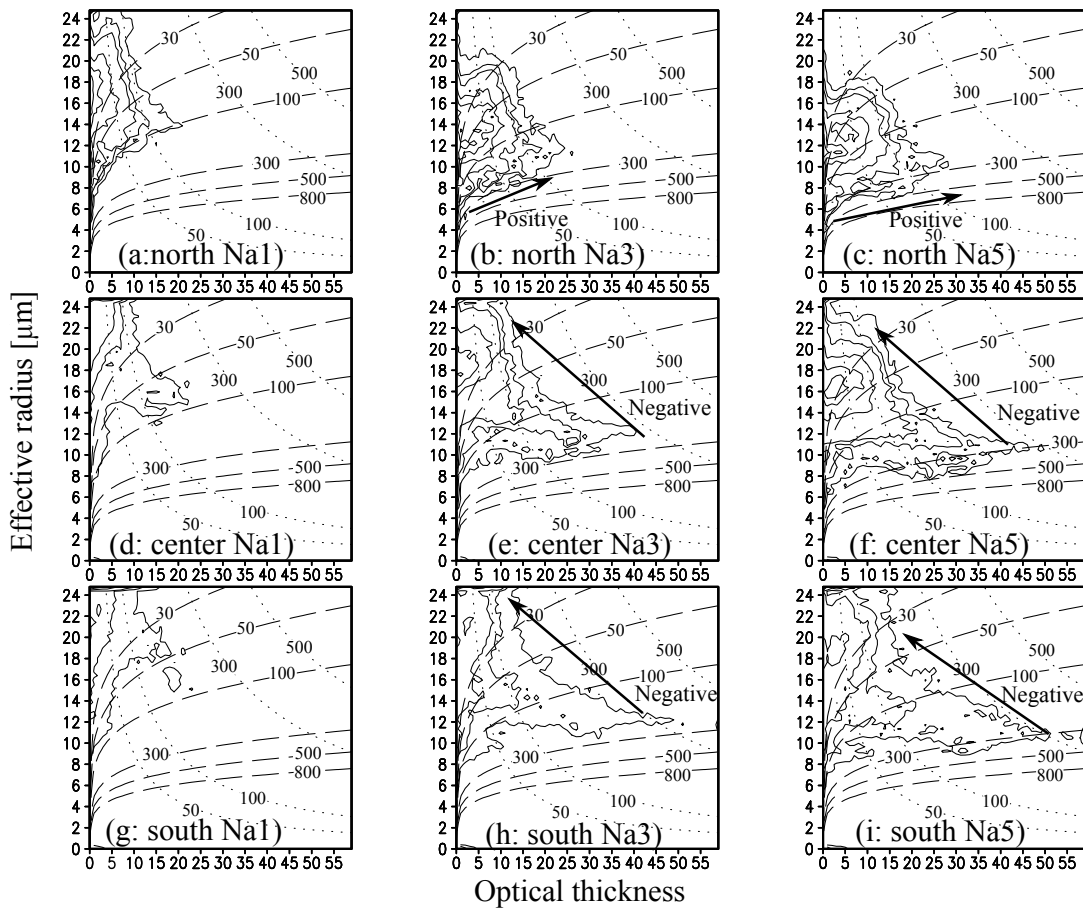


Figure 6.2. Same as Fig. 5.9, but obtained from the sensitivity experiment of aerosol amount. (a,d,g), (b,e,h), and (c,f,i) are obtained from the Na1, Na3, and Na5 experiments, respectively. (a-c), (d-f), and (g-i) show the northern, center, and southern parts of domain III, respectively. The contour values are for 0.01, 0.1, 0.3, 0.5, with setting the maximum value of frequency to 1. The dashed and dotted curves are isolines of cloud number concentration N_c and liquid water path W , respectively, based on an adiabatic-condensation growth model. The

isolines represent $N_c = 30, 50, 100, 300, 500, 800$, and $W = 50, 100, 300, 500 \text{ g m}^{-2}$

experiment, with the isolines for N_c and W given by the adiabatic condensation growth model indicate that the change in the aerosol amount is found to change N_c . The larger the aerosol amount is the higher the N_c becomes. Whereas, variation in W is small for the increase in aerosol amount.

The other contour lines move lower and more to the right area with increasing aerosol amount. This means that increases of aerosol amounts decrease cloud droplet size and suppress drizzle generation and precipitation, which decrease the reduction of W by precipitation.

These results show that increases of aerosol amounts lead to an increase in the *maximum value* of N_c in RE-COT patterns.

These trends are similar to those obtained by satellite remote sensing (Nakajima et al., 2001) and by models (Suzuki et al., 2004, 2010a).

Secondly, the sensitivity to PBL height is investigated. Spatial distribution of the cloud top height, corresponding to PBL height, at 15 UTC on July 10, 1987 is represented in Fig. 6.3. It is found that the PBL height monotonically increases with increasing SST.

Figure 6.4 represents spatial distributions of radiance at 15 UTC on July 10, 1987 obtained from the sensitivity experiment changing SST (*i.e.* PBL height) over domain I. The radiance decreases monotonically with increasing SST (*i.e.*, PBL height). Drizzle rate also increases with increasing

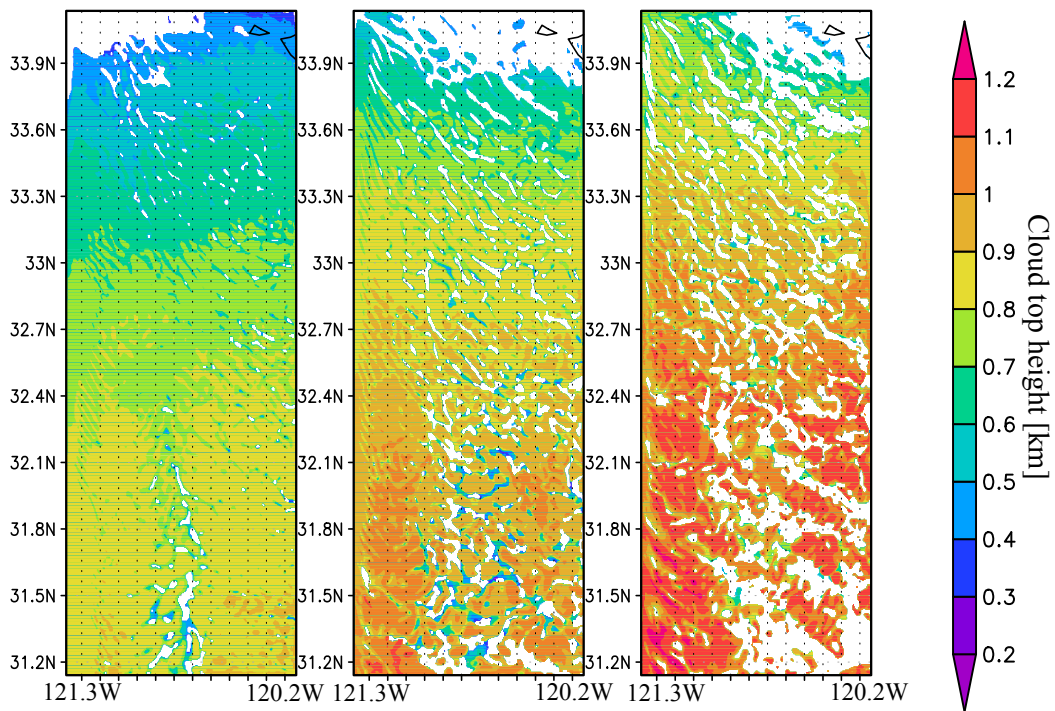


Figure 6.3. Spatial distribution of cloud-top height, which is corresponding to PBL height (km), of (a) sst-3, (b) CNTL, and (c) sst+3 experiments at 15 UTC on 10 of July 1987

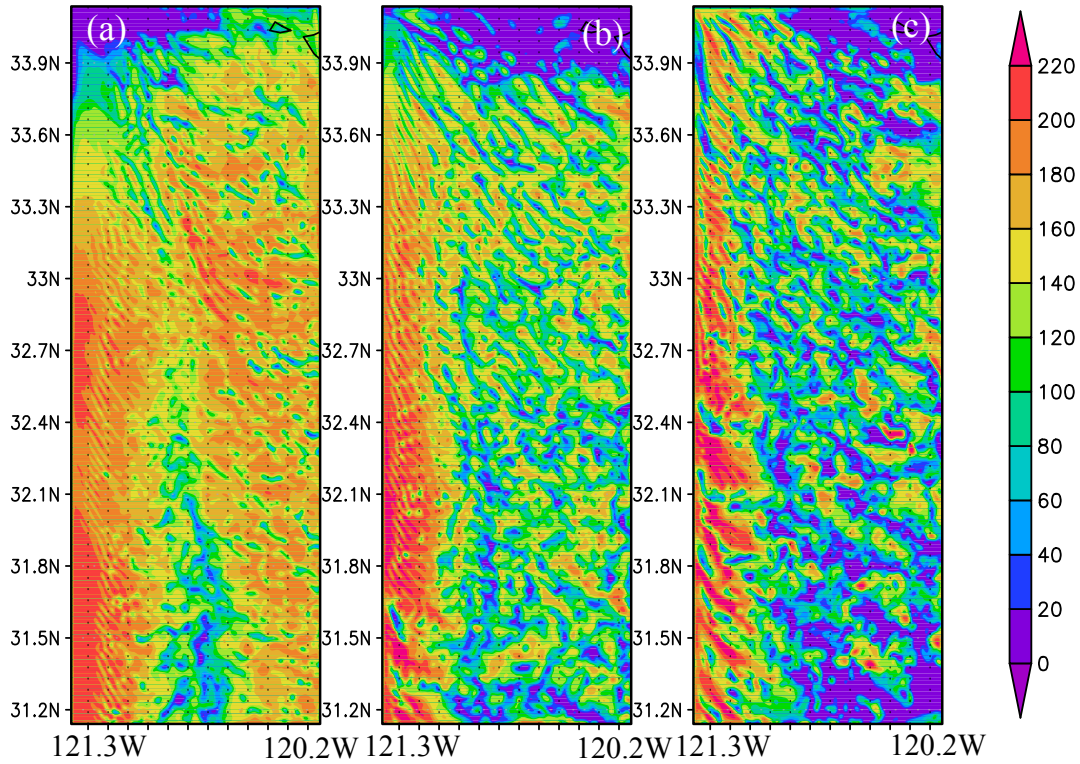


Figure 6.4. Same as Fig. 6.1 but obtained from (a,d) SST-3, (b,e) CNTL, and (c,f) SST-3 experiments, respectively, at 15 UTC on 10 of July 1987

SST (figure not shown). It is concluded from these results that atmosphere with high PBL height can easily produce drizzle, and decreases LWC by precipitation, which results in optically thin cloud corresponding to small radiance.

Figure 6.5 represents the RE-COT pattern obtained from the sensitivity experiment, and it demonstrated that positive and negative correlations are reproduced in the CNTL and SST+3 experiments.

The figures also indicate that a change in the PBL height affects the maximum value of W , which is drawn as outermost contour lines seen in the central part of domain III. Maximum value of W reaches about 320 g m^{-2} in SST+3 (Fig. 6.5f), 300 g m^{-2} in CNTL (Fig. 6.5e), and 180 g m^{-2} in SST-3 (Fig. 6.5d).

The other contours (*i.e.*, the contours except for the outermost contour) move upper and more to the left area with increasing PBL height. This means that increases of PBL height weaken atmospheric stability. This means that cloud droplets can easily grow to drizzle size in unstable conditions, which decreases mean value of W by precipitation.

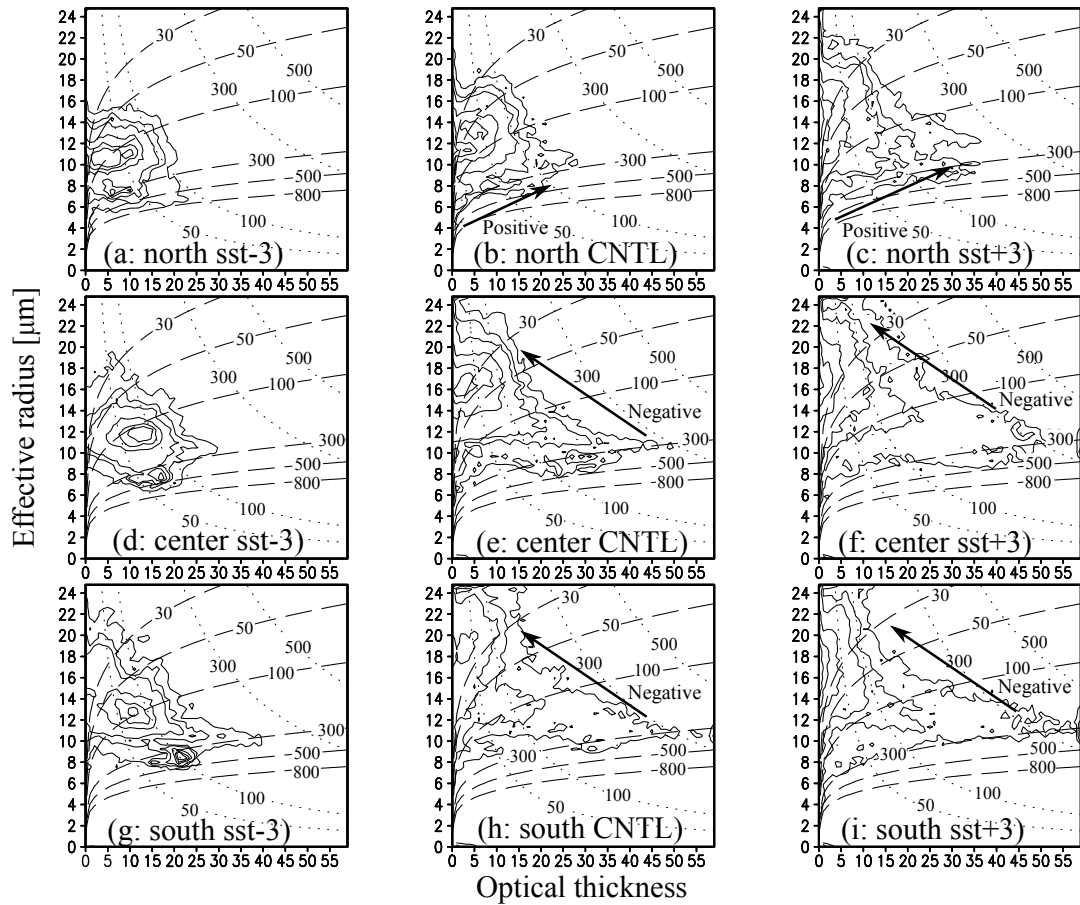


Figure 6.5. Same as Fig. 6.2, but obtained from the sensitivity experiment of aerosol amount. (a, d, g), (b, e, h), and (c, f, i) were obtained from the SST-3, CNTL, and SST+3 experiments, respectively. (a-c), (d-f), and (g-i) show the northern, center, and southern parts of domain III, respectively.

From these results it is found that that increases of PBL height lead to increases of *maximum value* of W in RE-COT patterns, even though the increase of PBL height reduces the mean value of W in RE-COT patterns.

This trend is also similar to those obtained by satellite remote sensing (Nakajima et al., 2001) and by models (Suzuki et al., 2004, 2010a).

6.2 Factors determining the characteristics of RE-COT pattern

The results in the previous section indicate the sensitivity of the RE-COT pattern to aerosol amount and PBL height. They give us some indications in finding the key factors determining the characteristics, *i.e.* shape and geometrical center position of patterns in the RE-COT diagram.

Figure 6.6 summarizes the tendency of the RE-COT pattern over the center part of domain III obtained from the sensitivity experiments. This figure shows the outermost contours and center of the RE-COT patterns simulated by the sensitivity experiments. The former is a good indicator of the uppermost values of LWP and N_c , whose values are obtained when the cloud grows adiabatically. The latter is a good indicator in showing where the main population is located on the RE-COT plane.

From this figure, it can be discussed how large the value of LWP and N_c can become in each aerosol and dynamical condition. Since we can roughly quantify the shape and position of the RE-COT patterns by the right edge, bottom edge, and geometrical center of the pattern, focuses of the following analysis are set upon these three elements.

It is seen from Fig. 6.6 that the right edges of the contour lines move along the isoline of W and across the N_c isolines as aerosol amount increases. This indicates that an increase in aerosol amount tends to increase N_c with small changes in W values. In contrast, when the PBL height is changed, the right edges of the contour line move across the W isolines, indicating that the higher the PBL height is, the larger W becomes. The bottom edge of contour lines is clearly affected by the aerosol amount and the effect of PBL height on the bottom edge is very small. Being affected by both stability and aerosol amount, the geometrical center moves across both isolines of W and N_c .

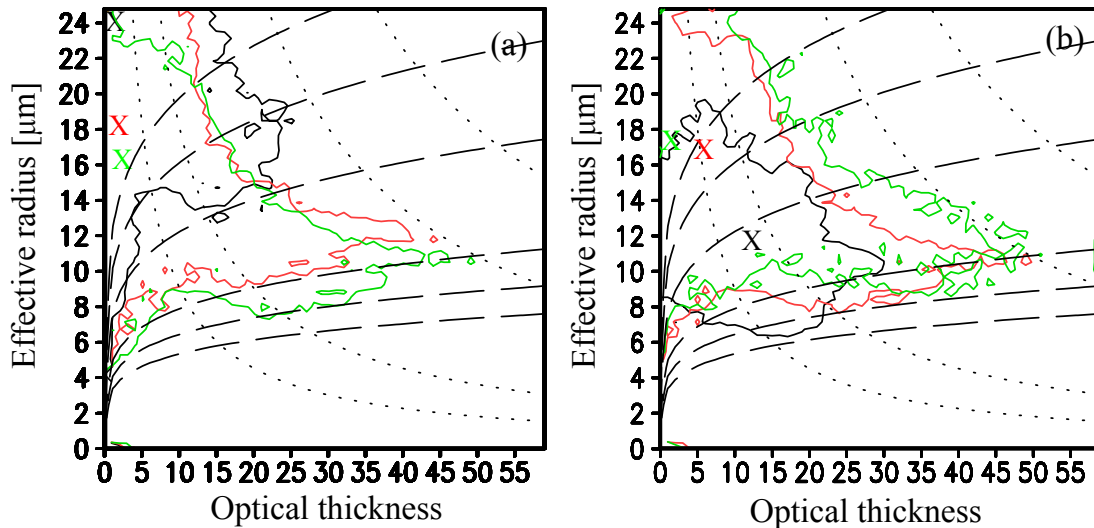


Figure 6.6. Summarized correlation patterns obtained from the center of domain III by (a) the changing aerosol amount sensitivity experiment and (b) the changing inversion height sensitivity experiment. The black, red, and green solid lines are the smoothed contours obtained from (a) Na1 (b)sst-3, (a) Na3 (b)CNTL, and (a) Na5 (b) sst+3, respectively. The contour value is same as that of the outermost contour of Figures 6.2d-f and Figure 6.5d-f, whose value is set to 0.01 (1 %) of the maximum value of frequency. “X” is center of each contour.

Several scatter plots were created to estimate the effects of PBL height and aerosol amount on the shape of the RE-COT pattern. To make these scatter plots, the model-derived PBL height, column accumulating CN number concentration and drizzle rate averaged over the three areas of south, center, and north part of domain III at 15UTC on July 10, 1987 are used.

Firstly, the bottom and right edge are discussed. To represent these edges, the maximum values of W and N_c (henceforth, referred to as W_{max} , $N_{c,max}$) in the RE-COT patterns are used. The large W_{max} ($N_{c,max}$) corresponds to a more right (lower) position of the right (bottom) edge.

It is found from Figs. 6.7a and 6.7c, that W_{max} clearly correlates well with PBL height rather than with column accumulating CN number concentration (*i.e.* correlation coefficients between PBL height, column accumulating CN amount and W_{max} are 0.7932 and 0.3013, respectively). This means that the right edge of the RE-COT pattern is more sensitive to the PBL height than the CN number concentration (*i.e.* aerosol amount).

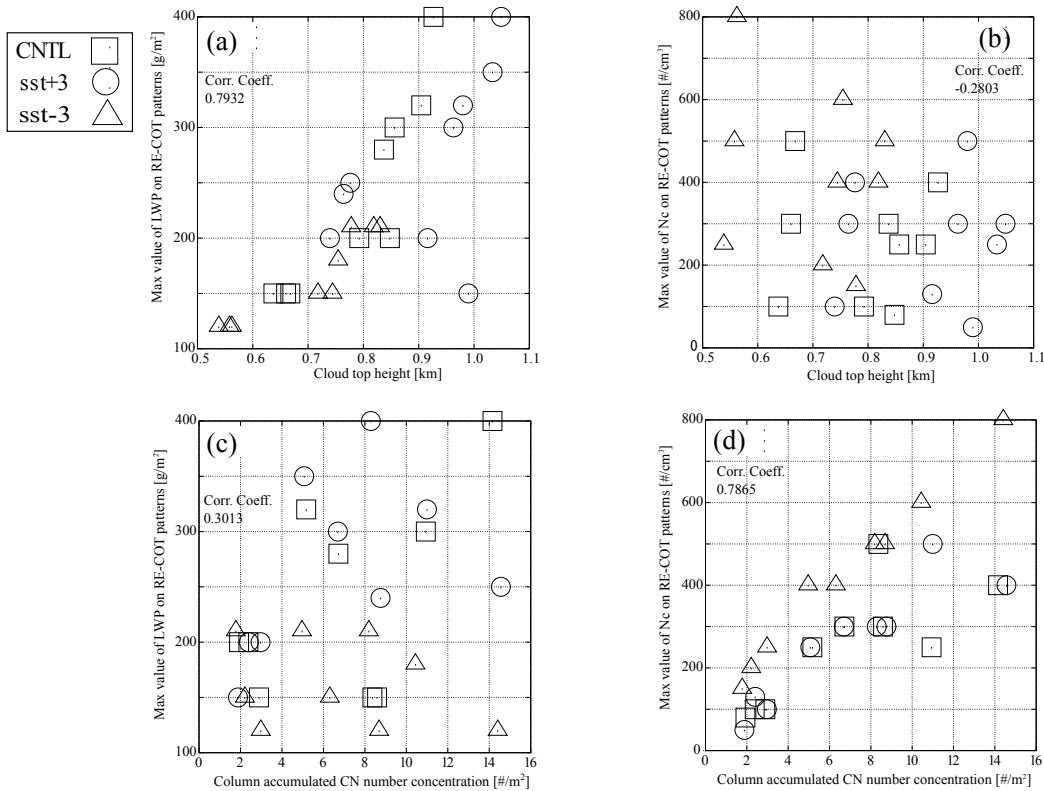


Figure 6.7 Scatter plots of (triangle) sst-3, (square) CNL, (circle) sst+3 experiments between (a) PBL height (corresponding to cloud top height) and maximum value of LWP on the correlation pattern between r_{eff} and τ (RE-COT pattern), (b) PBL height and maximum value of N_c on RE-COT pattern, (c) column accumulated CN number concentration and maximum value of LWP on RE-COT pattern, (d) column accumulated CN number concentration and maximum value of N_c on RE-COT pattern, respectively with their corresponding correlation

It is found from Figs. 6.7b and 6.7d, that the $N_{c,max}$, in contrast, clearly correlates with column accumulating CN number concentration but not with the PBL height (*i.e.* correlation coefficients between PBL height, CN amount and $N_{c,max}$ are -0.2803 and 0.7865, respectively). This means that the effect of aerosols on the bottom edge of the RE-COT pattern is larger than that of the PBL height.

Secondly, the geometrical center of the RE-COT pattern is discussed. In this case, W_{max} and $N_{c,max}$ are not used, but COT and RE averaged over each domain of each experiment. These are good indices of the position of the geometrical center (henceforth, referred to as center) of the RE-COT pattern. In addition, a drizzle rate is introduced, given as:

$$D_{drizzle} = \int_{r=2.1\mu m}^{r=3251\mu m} f(r)V(r)dr, \quad (6-2)$$

which is an index of the precipitation amount. Because the cloud does not always grow adiabatically, the index of precipitation, which is one of the diabatic processes, is introduced in this study. Figure

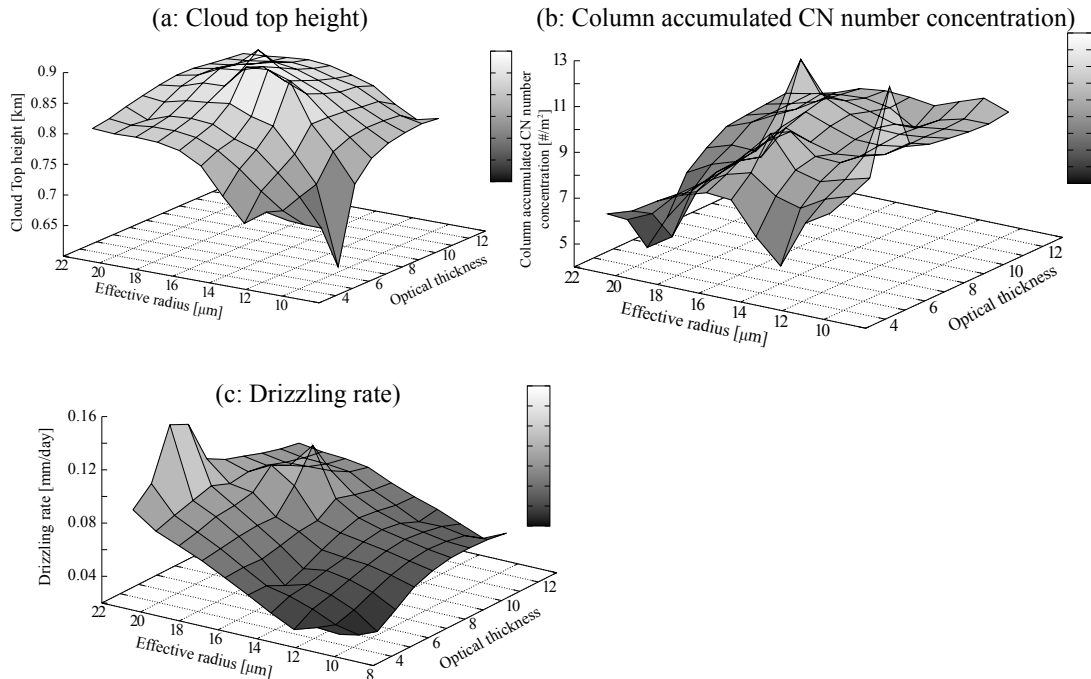


Figure 6.8. Statistical results between (a) PBL height, (b) column accumulated CN number concentration, and (c) drizzling rate and geometrical center of RE-COT plane, the shaded values shown are corresponding to the values of vertical axis

6.8 indicates relationships between the center of the RE-COT pattern and PBL height, column CN number concentration, and drizzle rate.

The x-y plane corresponds to the RE-COT plane, and it shows the positions of the averaged values of RE and COT of each experiment. The z-axis shows the value of each variable (*i.e.*, PBL height, CN number concentration, and drizzle rate). Thus, the 3D-plane shows the value of each variable at each position of the RE-COT plane. The shade shows the value of the z-axis variable (*i.e.*, PBL height, CN number concentration, and drizzle rate).

The center of the RE-COT pattern is located in a more left and upper area when the PBL height is higher, drizzle rate is larger, and column accumulated CN number concentration is smaller. These results indicate that the center position is determined by the PBL height, aerosol amount, and drizzle rate, although these factors are dependent upon each other.

The relationships between these factors and the center of the RE-COT pattern are represented in Fig. 6.9. It is found from the figure that 1) the higher PBL height is, the larger the drizzle rate is, 2) a smaller aerosol amount leads to a larger drizzle rate, and 3) the RE-COT pattern is located in a more left and upper area when the drizzle rate is larger.

These results indicate that the center of RE-COT patterns obtained from clouds with high drizzle rate (*i.e.*, clouds with large amounts of precipitation) is located in a more left and upper area, and PBL height and aerosol amount affect the position of RE-COT patterns by changing drizzle rate.

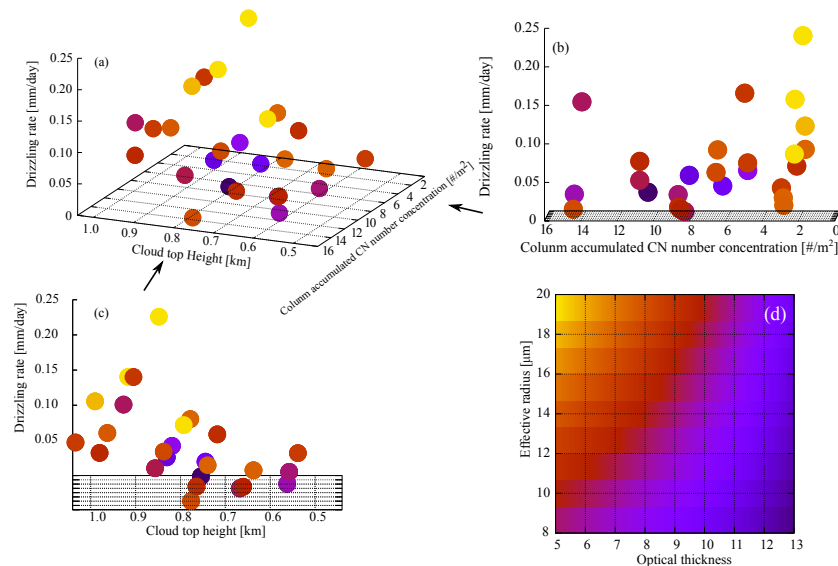


Figure 6.9. (a-c) 3-D scatter plots between (x-axis) column number concentration, (y-axis) PBL height, and (z-axis) drizzling rate. (b) and (c) are the same as (a) except for viewed by different angles. The colors of plots in (a-c) represent the position of each plot on RE-COT plane in (d).

From this result, it can be inferred that the other factors (*e.g.*, entrainment, large-scale divergence), whose sensitivity is not investigated in this study, can also change the position and shape of RE-COT patterns through changing drizzle rate.

From the results shown above, it can be concluded that factors that determine the characteristics of the RE-COT pattern *i.e.*, the right edge, bottom edge, and geophysical center, are mainly PBL height, aerosol amount, and drizzle rate, respectively.

The results show some of the possible factors determining the RE-COT pattern; however, other factors could also determine the characteristics of warm cloud. Thus, in future, the effects of other factors that can change the RE-COT pattern should be investigated.

6.3. Bi-modal distribution of RE-COT pattern

In the previous sections, several key factors that determine the characteristics of RE-COT patterns from the results of the sensitivity experiment are studied. In this section, an interesting issue among the results of the sensitivity experiment is discussed: the bi-modality in the RE-COT pattern as shown in Fig. 6.5h. One mode is located in the upper and left area, the other mode is located in the middle and right area with the border of isoline $N_c=75 \text{ cm}^{-3}$. This bi-modality indicates that the RE-COT patterns are composed of two groups divided by the isoline of $N_c=75 \text{ cm}^{-3}$.

This feature did not appear in the previous studies (Suzuki et al., 2010a, b), even though the cloud microphysical scheme used in the previous studies was essentially same as the one used here (*i.e.*, UT-ACBM). The major difference of this study from the previous study is the experimental setup, as described in chapter 5. Hence, the bi-modal feature must reflect two kinds of clouds with different microphysical properties co-existing in the calculation domain, *i.e.* those with droplet number concentrations greater than about 75 cm^{-3} , and those less than about 75 cm^{-3} .

Figure 6.10 presents separate spatial distributions of COT for these two groups of clouds separated by $N_c = 75 \text{ cm}^{-3}$ (henceforth, this threshold value of N_c is referred to as N_t). The figure indicates that except for the western boundary (upstream boundary), the clouds corresponding to a lower number concentration (*i.e.*, $N_c < N_t$) are located in the southern part of the computational domain with thinner optical thickness, whereas the clouds corresponding to a greater number concentration (*i.e.*, $N_c > N_t$) are located over the northern parts of the domain.

This spatial distribution of the different kinds of cloud is determined by the distribution of aerosol amount and the wind field at the initial time in domain III, as shown in Fig. 5.3. A high pressure system is located around (37°N, 140°W) that causes an anti-clockwise flow, which results in the

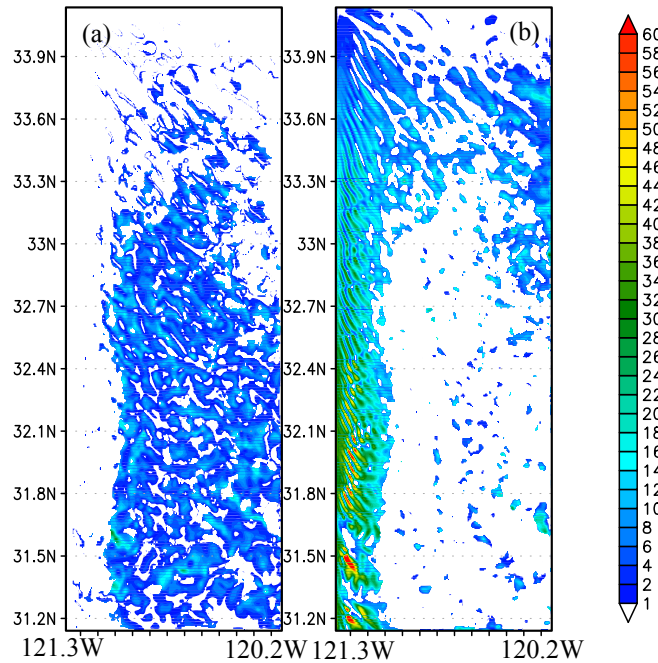


Figure 6.10. Optical thickness for the regions with number concentration (a) smaller than 75 cm^{-3} and (b) larger than 75 cm^{-3} at 15 UTC 10 July 1987, as calculated by the model in the CNTL simulation.

northwesterly wind and the aerosol transport from the northern and western boundary of the calculation domain III.

To some extent, this characteristic pattern is similar to the satellite-retrieved distributions of COT and RE as shown in NN95, which demonstrated a distinct difference in the COT and RE values between western and eastern regions of their observation separated by a longitude of 122°E (Fig. 5.1-right).

These results reveal that the bimodal characteristic of the RE-COT pattern is generated from multiple clouds with different microphysical characteristics caused by the inhomogeneity in the dynamical structure of the atmosphere and aerosol loading in domain III.

The results of the sensitivity experiments are summarized in Fig. 6.11. Figure 6.11a summarizes factors determining shape and location of RE-COT pattern. The figure demonstrates that the right and bottom edge, which correspond to the maximum values of W and N_c , are mainly determined by PBL height and aerosol amount, respectively, *i.e.*, the larger the $W(N_c)$ is, the more right (lower) the right (bottom) edge of the RE-COT pattern is. The figure also shows that the center of the RE-COT pattern is mainly determined by drizzle rate.

Figure 6.11b demonstrate that the signal of each cloud moves along the anticlockwise triangle form as shown in arrows. The figure implies that the RE-COT patterns are not an indicator of the growth process of each cloud.

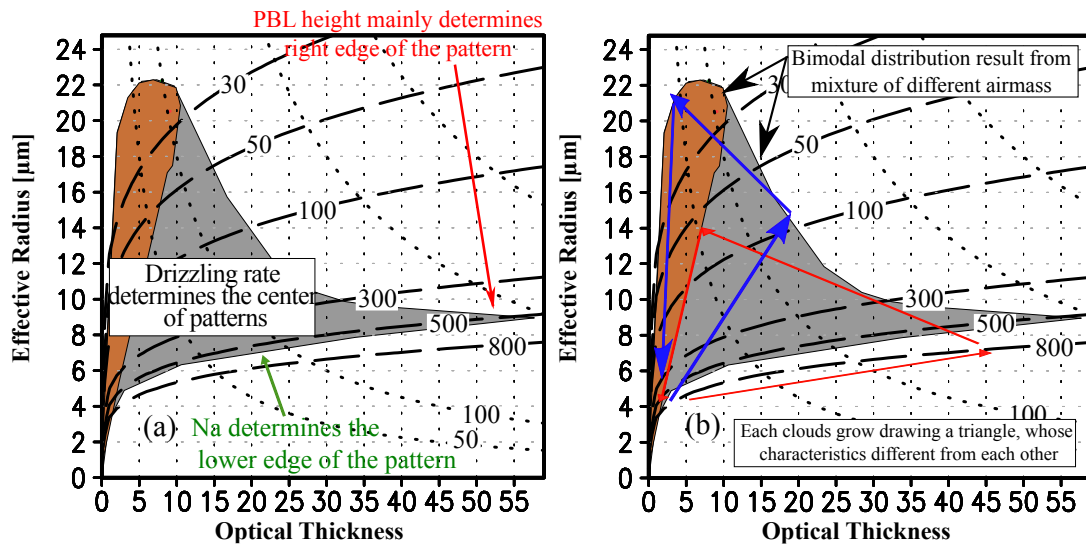


Figure 6.11. Summary of sensitivity experiment; Na and PBL height represent aerosol number concentration boundary layer height, respectively. Positions of the center, the bottom edge, right the edge of the correlation patterns are mainly determined by drizzling rate, Na, and PBL height, respectively (left), and each cloud draw a triangle on the RE-COT patterns during its growth stage (right). Mixture of brown and grey color shows mixture of the patterns.

Although the RE-COT patterns do not represent the growth process of each cloud, they represent the ensemble view of signals of each cloud accumulated over the whole observation domain. The characteristics of RE-COT patterns are determined by dynamical conditions, *e.g.*, PBL height, aerosol amount, and drizzle rate as shown in Fig. 6.11a.

The colors shown in both figures of Fig. 6.11 indicate that the RE-COT pattern can be multi-modal distribution if there are several air masses whose characteristics are different from each other. Grey and brown colors show a schematic RE-COT pattern by different types of clouds in different types of air masses.

Chapter 7. General Conclusion

This dissertation investigates the statistical features of the correlation between cloud-droplet effective radius (RE) and cloud optical thickness (COT) (RE-COT patterns) and Contoured Frequency Optical Depth Diagram (CFODD) through several numerical experiments using a three-dimensional regional Spectral Bin Model (SBM). The regeneration process of aerosols by complete evaporation of hydrometeors (Feingold et al., 1996) is implemented to the University of Tokyo Aerosol Cloud Spectral Bin Model (UT-ACBM) to simulate the microphysical characteristics of warm clouds interacting with aerosols. In order to reduce the computational cost of these detailed microphysical models, the UT-ACBM, a Monte Carlo-based integration scheme for the collision-coagulation equation of Sato et al. (2009), is introduced.

The CFODDs are reproduced, for the first time ever, from the data by numerical simulations using a 3D-SBM. Analyzing the numerical results of CFODDs derived from the idealized simulations with a fine grid resolution ($dx=dy=50\text{m}$, $dz=20\text{m}$) and from the zero-dimensional box model calculation, it is found that the CFODD patterns reflect the characteristic of cloud growth processes as suggested by Nakajima et al. (2010b) and Suzuki et al. (2010c), *i.e.* pattern (i), (ii), (iii), and (iv) of Fig. 3.1 represent particle uplift from cloud bottom to cloud top, condensation process, collision/coagulation, and evaporation at cloud top, respectively.

Idealized simulations using the dynamical condition of DYCOMS-II RF02, which is a campaign to observe warm clouds off the west coast of California, are conducted to investigate the effects of horizontal grid resolution on the characteristics of warm clouds. The results show that

- (1) cloud-top entrainment with a coarse grid resolution is weaker.
- (2) The wide updraft area simulated by coarse grid resolution can transfer more vapor from sub-cloud layer to cloud layer, which results in a large amount of LWC at coarse grid resolution.
- (3) Large cloud water content can generate strong radiative cooling by outgoing longwave radiation at the cloud top, which drives strong turbulence and strong entrainment at cloud top when drizzle generation is weak. This feature is seen in simulated results at intermediate grid resolution (*i.e.*, $dx=100\text{m}$ or 300m). When the large amount of drizzle is generated, evaporation of drizzle and evaporative cooling stabilize the atmosphere, as a result, entrainment is weak, which is seen in simulated results at coarse grid resolution (*i.e.*, $dx=500\text{m}$).
- (4) Strong entrainment simulated by the finest grid resolution (*i.e.*, $dx=50\text{m}$) promotes evaporation of cloud droplets at cloud top and reduces LWC .

This conclusion leads to a suggestion that both COT and RE simulated by the model can be affected by its grid resolution. In spite of such effects as grid resolution, responses of the RE-COT patterns to aerosol amounts and PBL height are similar. Therefore, the main characteristics of the RE-COT pattern can be discussed based on the simulation with the model at 500 m grid resolution. The simulated results also indicate that a model with several kilometer grid resolution (*i.e.*, courser grid resolution than that used in this study) tends to simulate optically thick clouds with large drizzle rate. This conclusion is important for the simulation of RE-COT patterns using models with coarse grid resolutions in future.

Based on the above-mentioned reasoning, simulations with the numerical model of 500 m grid resolution are conducted under a real atmospheric condition to simulate RE-COT pattern and CFODD. These results have been compared with satellite observations. By implementing the regeneration process of aerosols, it is confirmed that the model becomes able to reproduce satellite-retrieved characteristics found in the RE-COT pattern and CFODD of warm clouds.

Results of the simulations demonstrate several points about the RE-COT pattern as follows:

- (1) RE-COT patterns retrieved by satellite do not always represent the cloud growth process of each cloud cell, because it is composed from mixtures of several RE-COT patterns whose characteristics are from different processes.
- (2) Although these patterns do not represent cloud growth processes as suggested by Suzuki et al. (2010a), the suggestion of Suzuki et al. (2010a) can be applied for an isolated cloud.
- (3) The shape of the RE-COT pattern is determined by several key factors, *i.e.* drizzle rate, PBL height and aerosol amount. The bottom edge of the RE-COT pattern shifts downward with increasing aerosol amount, while the width of the pattern is mainly determined by the PBL height. The geometrical center of the RE-COT pattern is determined by drizzle rate, *i.e.* if the drizzle rate is large (small), the RE-COT pattern shifts to a left-top (right-bottom) position of the diagram.

These tendencies give us useful knowledge that can help interpretations of the cloud growth processes observed from next generation satellites (*e.g.* EarthCARE, Himawari-8, Himawari-9, and GOES-R), and the knowledge will contribute significantly to not only the science of satellite observation but also to that of cloud microphysics.